UNIVERSITÀ DEGLI STUDI DI PAVIA

DOTTORATO IN SCIENZE CHIMICHE E FARMACEUTICHE

XXX CICLO

Coordinatore: Chiar.mo Prof. Mauro Freccero

Human locomotion energy harvesting

Tutore

Chiar.mo Prof. Piercarlo Mustarelli

Tesi di Dottorato di

Fabio Invernizzi

a.a. 2016- 2017

Human locomotion energy harvesting

1. Introduction

The research project, described in this thesis, has the goal to design, develop, test and fabricate a passive energy harvester device able to recover the energy produced during human gait.

In the following sections, I will discuss, take into account and evaluate different aspects of energy harvesting from human motion. In particular (i) energy feasibility, to verify if enough energy is developed (thus can be harvested) during gait; (ii) gait physiology, to individuate the best position where to place a possible harvester and (iiI) physical phenomena to effectively harvest energy, were considered to draw the guidelines of the next experimental investigation.

To achieve the aim of this project, the research started from a screening of pre-existent literature in this field, to individuate the most suitable processes and physico-chemical phenomena to be exploited for harvesting purposes and the best body parts where to place the device. As second stage, the research involved understanding of physical and electrochemical aspect of selected harvesting phenomena. This was preparatory for the study and preparation of innovative materials able to harvest energy more efficiently. As the final step, once individuated a suitable material and energy harvesting system, design and development of a self-standing device able to harvest was carried out, to transform and store the energy developed by humans during walking.

From a preliminary evaluation on human gait, in this research project I decided to focus my efforts on harvesting the energy developed in the foot region. This decision comes from two principal considerations: 1. from different physiological studies emerged that feet are one of the most “powerful” sites of the body (due to pressure by body weight on the heel and metatarsal region); 2. harvesting energy from feet permit to exploit the shoe as housing where to place the energy harvester device (shoe sole can contain it, allowing to harvest energy without increase the user volume and/or affect the human gait). On the other hand, experimental research was focused on two different physical phenomena: reverse electrowetting on dielectric (REWOD) and electrostrictive polymer composites (EPCs). In particular with regard of REWOD, our intent was to reduce the fabrication steps by means of the only sputtering deposition technique, optimizing a processes that permits to obtain a REWOD device in a one-step fabrication; in view of a possible future industrial-scale application. Also, I focused my efforts on individuate and fabricate REWOD devices based on different dielectric oxides that can be more electrochemically efficient and cheaper than the anodized Ta_2O_5, actually employed.

For what concerning the electrostriction field, my research was directed to individuation of polymers functions and/or fillers that enhance the electrochemically efficiency (thus the generated energy) of the energy harvesting through electrostrictive polymer. This will pass obligatory through the study of the electrochemical processes that permit to obtain energy in this way and, since the relative new field of research, the design and development of a measuring instrument able to characterize the energy harvesting properties of these materials under the conditions of human gait.

2. State of the art

In the last century, we assisted to a rapid and constant increase of the world energy demand. This has been due to many reasons, including world population increase, development/industrialization of emerging countries, new and more demanding technologies. The world's energy demand is expected to reach 18 billion tons oil equivalent (t.o.e.) by 2035 under current policies[1]. The percentage of electrical energy consumption passed from 9% in 1973 to 18% in 2012; in contrast, the need for other energy sources, e.g. oil, coal or natural gases, remained the same or even decreased in the same time span. This means that in the future, electrical energy will presumably be the most consumed form of energy, and its production shall be as efficient as possible to satisfy the increasing demand.

In recent years, the electrical energy demand has also due to the rapid development of technologies that have become of daily use in our life, both in the workplace as in the free time, like computers, displays, conditioners, industrial robots and so on. At these relatively new technologies, has to be added the more recent portable technologies (such as smartphones, tablets, smartwatches, etc.) that need a portable electrical energy source to work, actually Li-ion batteries. In order to satisfy the increasing electrical energy demand, many efforts were made to produce electrical energy from renewable sources, instead from fossil fuels combustion.

In this frame, was born the concept of *Energy Harvesting* (EH). It consists in the recovery of the energy from different environmental sources (e.g. sunlight, heat gradient, wind, etc.), to produce electrical energy to be stored or used *in-situ*. The devices that perform this energy transformation are commonly called *energy harvesters*. To date, there exist different examples of energy harvesting devices that are commonly used to produce energy: geothermal plants, exploiting the internal heat of the Earth; photovoltaic plants, that harvests sunlight; fuel cells, reacting hydrogen and oxygen to generate electrical energy and water, and many others. Recently, a "new" renewable, sustainable, green, portable and potentially large-scale energy source has been coming under study: kinetic energy from human body movements[2, 3]. Human body offers a large number of movements that can be potentially exploited to generate energy, for example: bending of legs[4], oscillation of the arms[5], breathing, finger motion, etc. In energy harvesting field, energy harvesters for human body motion are divided in two principal classes: i) *active* harvesters, where the user

is required to perform some voluntary action in the process of generating electricity (e.g., pressing springs); ii) *passive* harvesters*,* where the harvesting is performed from users passive motion, without that he notice to do it (e.g., harvesting during breathing, walking or doing sports).

As can be deduced, the main drawbacks of the transposition of energy harvesting concept to human motion is related to the device itself: it must be wearable, passive, safe and non-invasive. To do this, materials and architectures able to harvest the kinetic energy of human motion, must be designed also considering the transition from the laboratory to the industrial scale[6].

2.1 Gait analysis

One of the first points to be considered when designing an energy harvester generator, is if there is enough available energy to be harvested. In the case of EH from human motion, a careful study on human kinetic physiology is mandatory.

T. Starner, in his work, calculated that a maximum theoretical value of about 67 W is generated when a 68 kg human heel falls to the ground [7]. He also calculates energies from some common actions, for example: breathing (0.8 W when chest expands and relaxes); upper limb lift (60 W); finger tapping on a keyboard (6.9 mW). However, this power values comes from calculation that do not take into account factors that can alterate the effectively available energy, like the damping of the shoe sole when the foot approach to the ground or the frequency of the action under investigation.

In another work, Niu *et al.* measured the energy developed by different body parts, taking into accounts such mechanisms that could affect the effective available energy, and using three different devices based on piezoelectricity, electrostriction and electromagnetic induction, respectively[8]. As conclusion, they found that the available energy at the heel oscillates from 2 to 20 W for each step (1-5 J/step); while from the comparison of different harvesters they concludes that electromagnetic induction and electrostrictive systems were the most promising approaches for this purposes. The first because of the high currents (thus high energy) that can be produced by moving a magnet inside a coil, while the second because it involve polymeric materials that are low-cost, flexible, stretchable and compliant with good harvesting properties.

More recently, M. Gorlatova *et al.*[9] using MEMS accelerometers placed on different parts of the body, were able to measure the energy produced by various human movements. The trial was performed over 40 participants. They correlated the generated energy (for 20 s of activation) with different parameters: 7 types of human movements (relaxing, walking, fast walking, running, cycling, going upstairs and downstairs), corresponding to different activation frequencies, bio-mechanic movement and location of the accelerometer. As expected, by increasing the activation frequency there was an increase of the available power. For instance, when passing from walk to run, the mean power generated for each step increases from 202 µW to 612 µW. They also obtained significant results by correlating human physiology to energy production, with taller people generating 20% more power than shorter ones. In addition, the kind of the action can affect the energy generation: e.g. go downstairs generate more power with respect to go upstairs. Finally, they evaluated the energy production over a working-day human activity for 5 different participants, during a period of 25 days (Fig. 2.1). As expected, energy generation during a working-day is alternated by regions of zero generation (depending on the job), when the body is stationary. This suggests, in a perspective of a final device, that the energy harvester should be able to store exceeding energy to cover that time intervals of zero generation, to ensure the feed power to electronics over the whole duration of no movement.

Finally, it should be also pointed out that these experimental measurements of body energies, take into account only the energy generated by body acceleration and deceleration, neglecting the energy component due to pressure/impact on the ground. The importance of pressure forces

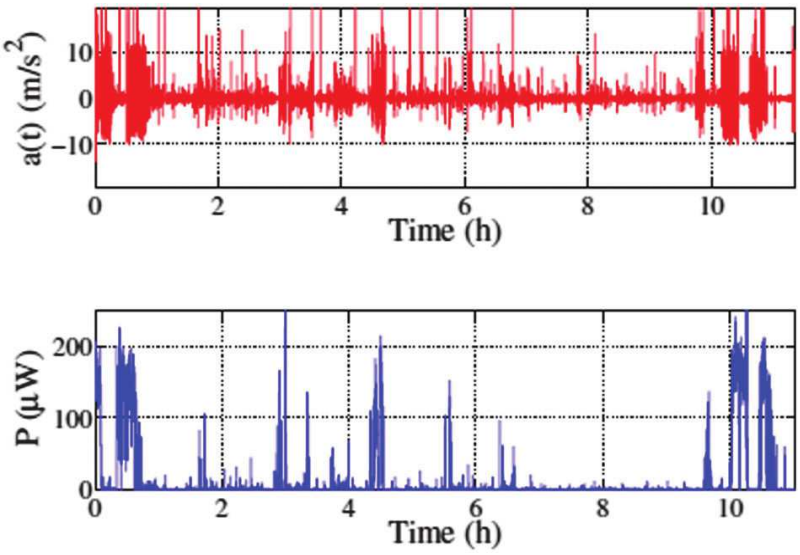

Fig. 2.1 *Acceleration (up) and developed power (down) graphs recorded over a working-day, for one person. Reprinted with permission from ref. 9.*

becomes evident when analyzing the human gait biomechanics. Human gait can be easily analyzed considering the gait cycle, focusing on one limb. As depicted in Fig. 2.2, the gait cycle (also called *stride*) is divided into two phases called *stance* and *swing*. Stance phase starts when the heel of the limb touch the ground: in this moment both the limbs supports the body weight. Subsequently, the gait continue with the detachment of the toe of the opposite limb, while the other foot approach, gradually, with all its area to the ground. At the end of this, the limb is parallel with the body and supports all the weight, while the other limb is moving through the air above the ground. Then, the supporting limb pass behind the bust, the heel detach from the ground, while the heel of the opposite foot start to touch to the ground: at this point the body weight is double supported. Finally, the stance phase end when the toe completely detach from the ground, letting all the body support to the other limb. Here, once toe-off happen, starts the swing phase: the limb move through the air from behind to ahead the bust, until the heel touch the ground again, thus closing the stride. In conclusion, a complete walking gait cycle is composed of an alternation of double and single support, in which each foot perform a stance phase (ground touching: from heel touch to toe-off) and a swing phase (ground detaching: from toe-off to heel touch).

However, this is true only when considering the common action of walking. In fact, increasing speed of motion our body is no longer able to continue to walk and is constrained to switch to run. From the point of view of gait mechanism there is no much difference between walk and run, while the main differences consists in body support. In fact, while walking is characterized by single/double support alternation, running is composed by stance phases, of right and left feet

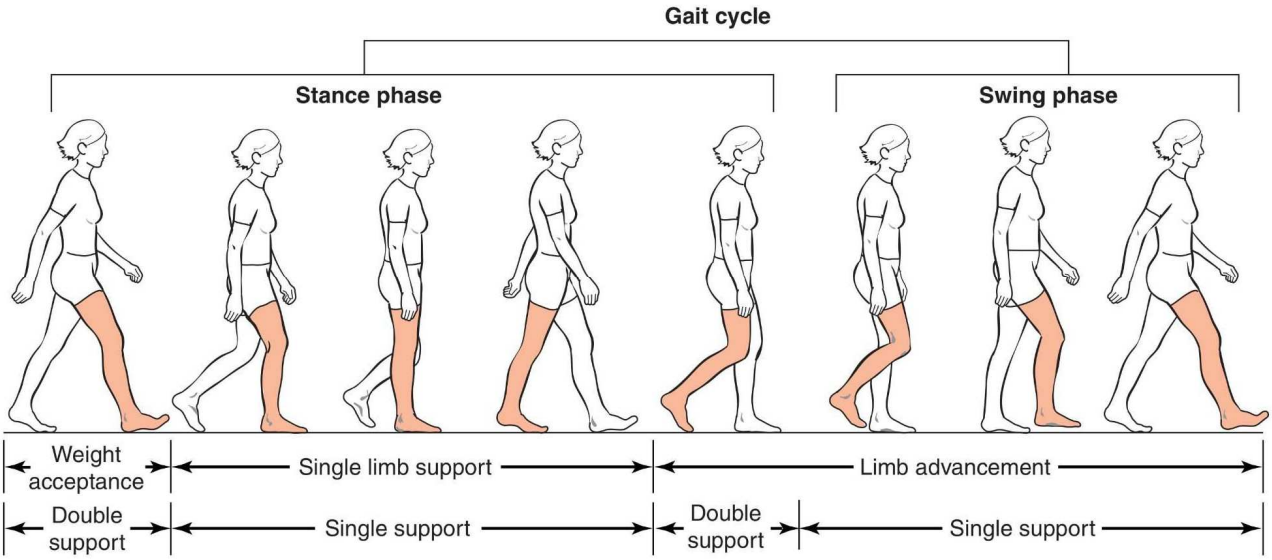

Fig. 2.2 *Gait phases during walking. Phases are referred to the movement of the colored limb.*

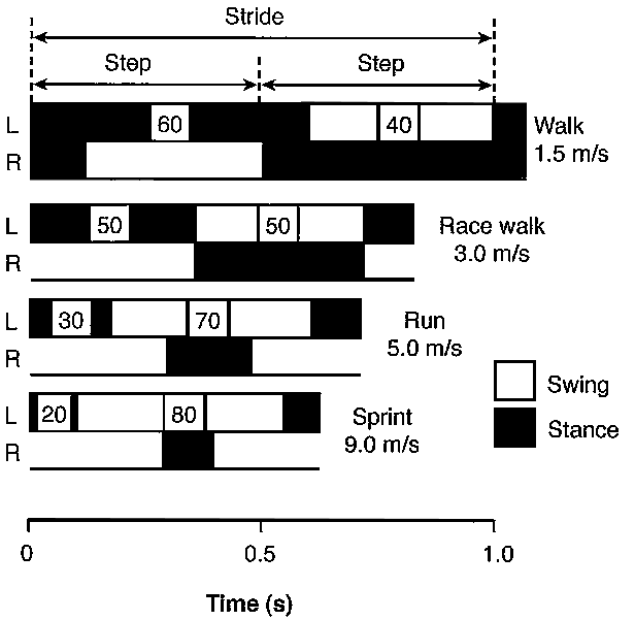

Fig. 2.3 *Events and phases characterizing walking and running gaits (R=right, L=left). The numbers in rectangles indicate the relative duration (% stride) of stance and swing phase.*

(single support) interrupted by a time interval where both feet are detached from the ground (no support), as showed in Fig. 2.3. From previous considerations on human gait, is evident that the foot involved in the stance phase is submitted to the body weight at different regions and that the energies developed on the foot area are affected by the frequency (walk or run), physiological parameters and by the type of action that is going on. In a very interesting work, E.M. Hennig and T.L. Milani were able to measure pressures exerted by the body on different regions of the foot directly during walk[10]. They built up an insole with 8 pressure sensors (2 heel; 2 midfoot; 3 forefoot; 1 toe) and represented the obtained values in 10 moments, redrawn in Fig. 2.4 (9 moments for better clarity). First available measure diagram correspond to 10 ms, when heel starts to touch the ground. Then, from 20 to 50 ms, the heel gradually support the body weight and the pressure on it raise up to 1MPa at 30 ms. After 50 ms, the body weight start to be supported by the whole area of the foot and at 90 ms the foot is completely leaning on the ground dividing equally the pressure over all the sole area. Starting from 130 ms, the heel gradually detach from the ground, body weight shift to the metatarsal region of the foot (at this moment pressure reaches values comparable with those obtained at the heel) and then decrease until 250 ms, after which toe-off occur.

Even if the developed pressures can change as function of personal gait and foot conformation, is possible to individuate the most powerful regions of the foot. In particular, the most powerful regions that emerges from data treatment resulted to be the heel, when it accepts the body weight

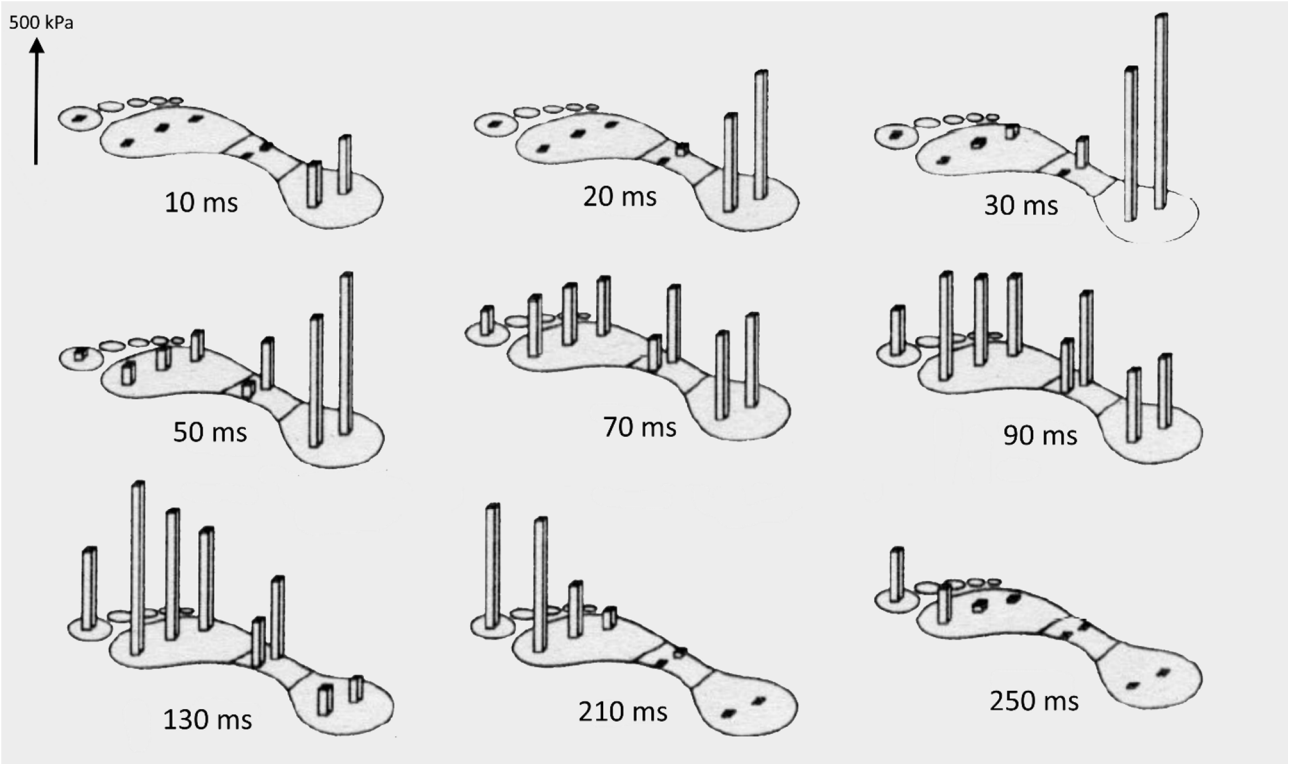

Fig. 2.4 *Pressure distribution at eight locations under the foot, during the stance phase for a subject running at 3,3m/s. Reprinted with permission from ref. 10.*

at the start of a new step, and metatarsal, when the foot pushes the body forward. From the energetic point of view, this parts seems to be the most promising to harvest energy from human gait. However, when designing an EH device many factors must be taken into account, in particular where EH regards human body. In fact, the placement of the device is important because it should be chosen as of no impediment to the normal body movement activity.

During discussion of body motion developed energy, we focused the attention on the energy developed by limbs and feet. This because of higher energies developed in such regions and also because of more sites where to place an EH devices. In fact, available volume in the shoe sole seems to be enough to host a little energy harvester without cause body movement impediment or sole deformation/enlargement, which could lead to walking disorders. In particular, for our purposes, the heel seems to be the most suitable site where to place an energy harvesting device.

To conclude, heel represents the most promising candidate for energy harvesting purposes in the lower part of the body. It satisfies both the energetic (most intense pressure produced on it, due to body impact on the ground) and volumetric requirements (in daily-use shoe soles the heel part result higher and offer more volume respect to the metatarsal part), thus our research project will be focused on development of a new energy harvesting device embeddable into a shoe sole.

2.2 Energy harvesting from human motion: state of the art

Despite one could image, the concept of energy harvesting is far from recent. One of the most famous and older examples of its energy harvester devices are self-winding watches. This mechanism exploit the movement of the wrist/arm (kinetic energy) to wind the mainspring that will supply the clock mechanisms (potential energy).

To date energy harvesting is intended as the conversion of a wasted environmental energy into electrical energy (more consumed) to power common electronic devices, by means of an energy harvesting device. About this, many different devices, harvesting different types of energy, have been developed during years. However, kinetic energy from human motion still remain one of the more difficult form of energy to be harvested, mainly because of the requirements of very small volume, wearability and efficiency, needed at same time. In spite of the obstacles related to the device itself, some vibration energy harvesters (VEHs) were developed to exploit energy from human motion, based on different physical phenomena, that divide them into three categories: 1. Electromagnetic; 2. Piezoelectric[11]; 3. Electrostatic[12] systems.

2.2.1 Electromagnetic systems

Electromagnetic systems were among the first classes of energy harvesters to be investigated, because of the simplicity of the mechanism and good output power, that easily permit to supply electronic devices. These systems are based on the well know current (I) induction into a conductive coil immerged in a magnetic field (B), by the variation of a magnetic flux (Φ_B), in any way, with time. At the same time, in the opposite direction of the induced current is developed an *electromotive force* (f_{em}), proportional to the magnetic flux (Φ_B) variation, described by the following equation:

$$f_{em} = -\frac{d\Phi_B}{dt} \qquad \text{(Eq. 2.1)}$$

According to the energy conservation principle, the physical work done against this force corresponds to the electrical energy produced by the system.

Let us consider an electromagnetic generator (a coil) constituted by N turns oscillating with an angular frequency ω in the x direction through a constant magnetic field B. The voltage produced across the circuit is a function of the coil turns N, magnetic flux gradient $\left(\frac{d\phi_B}{dx}\right)$, and velocity $v = dx/dt$:

$$V = -N\frac{d\emptyset_B}{dx}\frac{dx}{dt} \quad \text{(Eq. 2.2)}$$

The same result is obtained by moving a permanent magnet in a fixed coil. To contrast F_{em}, an amount of instantaneous power P_e should be developed, which is given by:

$$P_e = F_m(t)v(t) = F_m(t)\frac{dx(t)}{dt} \quad \text{(Eq. 2. 3)}$$

This power is dissipated in the coil and load electrical impedances. At the low frequencies (typically $\omega < 10$ rad s^{-1}) encountered in human motion, the coil inductance L_C has a reactance $\omega L_C << R_C$, so that the coil impedance reduces to R_C. By equating the power P_e to the electrical power dissipated in the circuit, P, and by using Eq. 2.2, we obtain:

$$P = F_m v = F_m\frac{dx}{dt} = \frac{V^2}{(R_C + R_L)} = N^2\left(\frac{d\emptyset_B}{dt}\right)^2\frac{\left(\frac{dx}{dt}\right)^2}{(R_C + R_L)} \quad \text{(Eq. 2. 4)}$$

It follows that in order to maximize the output power, one should obtain the best compromise among flux linkage gradient, coil turns, and coil resistance[13].

When design an electromagnetic VEH, the components to be optimized are permanent magnets and coils[14]. Permanent magnets are a class of materials that naturally produce a magnetic field. The property characterizing the strength of a magnet is the magnetization, M (magnetic dipole moment per unit volume), that is proportional to the magnetic field strength H: $M = \chi_m \cdot H$, where χ_m is the magnetic susceptibility. Relying on their magnetic properties, materials can be classified into four classes: diamagnetic, paramagnetic, ferromagnetic and ferromagnetic. However, only ferromagnetic and ferrimagnetic are of interest for EH purposes, because they are able generate a permanent magnetic field due to the alignment of the electron spin moments of the component atoms/molecules; while dia- and paramagnetic materials only respond (repulsion and attraction, respectively) when an external magnetic field is applied to them. Unfortunately, the pass from macro- to microscopic is not trivial for magnetic materials. As a matter of fact, hard magnets undergo a decrement of their properties (energy product, coercive force, etc.) with miniaturization. Common magnetic materials like Co–Ni–X (X = non-magnetic element), Fe–Pt, Co–Pt $L1_0$ ($L1_0$ refers

to the tetragonal distortion of a face-centred cubic structure) and rare earth magnets can be prepared by pulsed laser deposition (PLD), sputtering and electrodeposition. Among all of them, electrodeposited Co–Pt magnets are most suitable for micro-applications, due to their good magnetic properties and because they can be prepared at room temperature. Magnetic powders were also taken into account for micro-applications. This approach has the advantage of addressing the problem of the optimal preparation of the material, leaving only the powder implementation burden to the device fabrication, but they suffer from bad magnetic properties.

For what concerns the final VEH, also coils has to be miniaturized to minimize the device volume and make it wearable. To achieve this goal, two main approaches can be followed: micro wire-wounded coils or micro-fabricated coils. Concerning micro-wounded coils, the decreasing of wire diameter increase rapidly the electrical resistance per unit length, thus reducing the efficiency of the generator, while micro-fabricated coils attracted attention due to their relatively simple fabrication in very small sizes and complex geometries. Micro-coils have been fabricated by different techniques: LIGA process (Lithography, Electroplating, and Molding)[15], electroplating on micro-templates; LCVD (laser-assisted chemical vapor deposition) and by automatic wire bonders[16].

Considering all the previous factors that could affect the efficiency of an electromagnetic VEH for human motion, Williams and co-workers were among the first to fabricate such kind of device [17]. As schematically shown in Fig. 2.5, it is composed of a case in which a seismic mass (*m*), i.e. the magnet, linked to a spring (*k*), of known spring constant, and a damper (*d*), that converts the vibration into electrical energy, are placed. In practice, the damper *d* is represented by the coil attached at the device bottom. This type of micro-generators are also called *inertial*.

They used a samarium–cobalt magnet (0.9 T) as the inertial mass, attached at the center of a polyimide membrane that acts as the spring. The electromagnetic damper consist of a planar gold

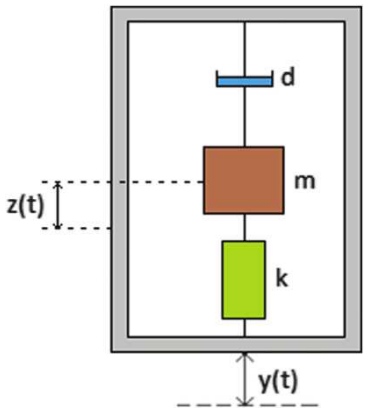

Fig. 2.5 *Schematic electromagnetic micro-generator fabricated by C. B. Williams et al. Redrawn with permission from ref. 17, copyright IEEE Xplore, 2008.*

coil, placed under the magnet on a silicon wafer that represent the housing of the device. With this arrangement, they obtained 0.3 µW at 4 kHz, instead of 1 µW at 70 Hz as predicted. The authors hypothesized two causes as responsible of this discrepancy: (i) at high frequencies the polyimide membrane give a nonlinear response; (ii) working in air atmosphere, a strong mechanical damping is present, which decreases the efficiency of the device. Based on the same inertial model, Beeby *et al.*[18] fabricated a device of 0.15 cm^3 volume, by using two pairs of NdFeB magnets, bonded at the end of a cantilever beam (two face up and two face down) that sandwiched a copper coil with their protruding part (Fig. 2.6). With this arrangement, the authors were able to reach power generations up to 428 mV and 46 µW (rms) at 53.2 Hz on an optimized load of 4kΩ, using a shaker actuator that apply an acceleration of 60m*g* and a 2300 turns coil.

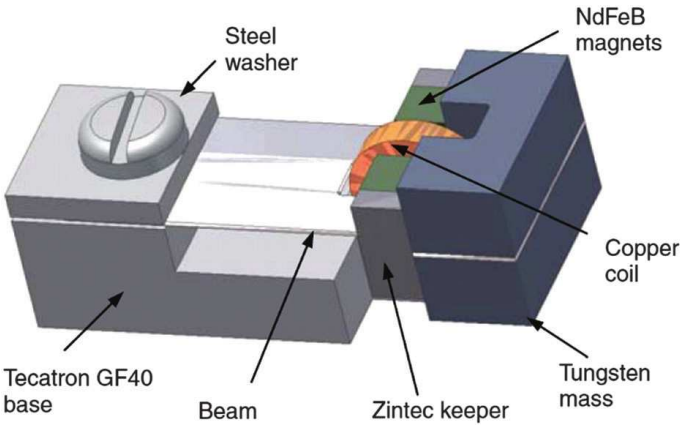

Fig. 2.6 *Micro cantilever generator proposed by Beeby et al. Reprinted with permission from ref. 18, Copyright Elsevier, 1996.*

2.2.2 Piezoelectric systems

The second class of VEH developed for human motion are that based on *piezoelectricity*. Certain inorganic crystals (e.g., some ceramics), polymers, as well as biological matter (such as bone, DNA and various proteins) become electrically polarized when mechanically stressed. The same crystal also exhibits the reverse effect, consisting of a mechanical strain or distortion when it is subjected to an electric field. Polarization charges appear on the pairs of opposite surfaces of the crystal, thus leading to a voltage difference between the same surfaces. Thus, piezoelectric crystals are essentially electromechanical transducers because they convert an electrical signal (electric field) into a mechanical signal (strain), and *vice versa*. Of the 32 crystal classes, 21 have no inversion center of symmetry, and 20 of these exhibit piezoelectricity. Let us consider, for example, a simple planar hexagonal cell (Fig. 2.7a), that has no center of symmetry: if we draw a vector from point O to any charge and then reverse the vector, we will find an opposite charge[19]. If the positive and negative ions have the same absolute charge, the total dipole moment is given by

$$p = \sum_i q_i \, r_i \qquad \text{(Eq. 2. 5)}$$

(with q_i the ion charge and r_i its position) and therefore the polarization

$$P = \frac{p}{V_m} \qquad \text{(Eq. 2. 6)}$$

(overall dipole moment per unit cell volume, V_m) is zero, *i.e.* the center of mass of the negative charges coincides with that of the positive charges. Under an applied force, that stresses the cell in the *y* direction (Fig. 2.7b), the center of mass for positive and negative ions is shifted, which results in a polarization $P_y \neq 0$. If the crystal is cut with two opposite faces perpendicular to *P*, polarization charges with opposite sign and surface density $\sigma = P$ appear on the faces, resulting in a voltage difference between them. When the stress is along the *x* direction (Fig. 2.7c), there is no net polarization along *x*, but there is along *y*.

There are two common modes utilized for piezoelectric energy harvesting: in the 33-mode the direction of applied stress and generated voltage is the same, whereas in the 31-mode the stress is applied in axial direction but the voltage is obtained from the perpendicular direction.

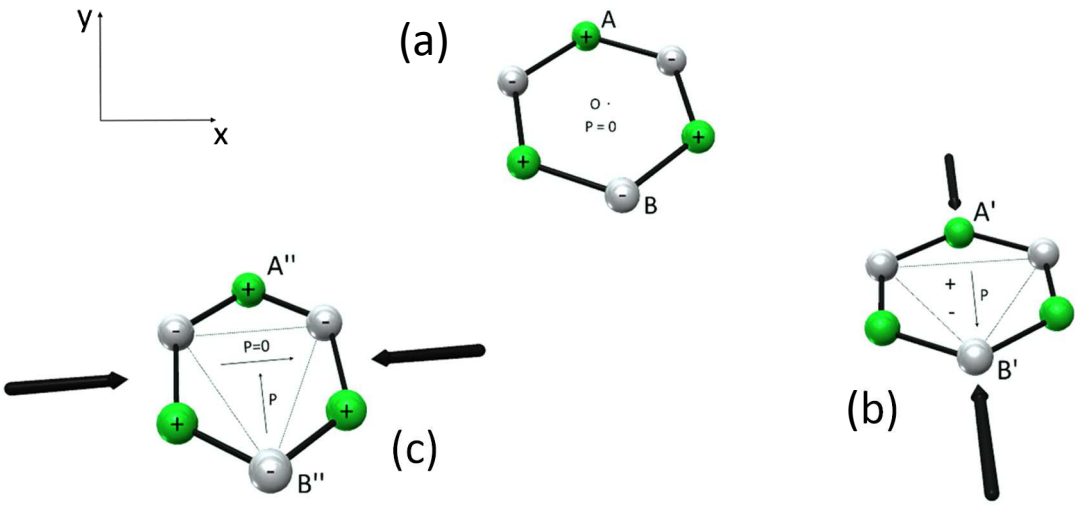

Fig. 2.7 *Induced polarization P in a hexagonal unit cell that has no center of symmetry: (a) in the absence of an applied force P = 0; (b) an applied force along y produces a net polarization P along y; (c) when the force is along x, there is no resulting net dipole moment along x but there may be a net P along y. Redrawn with permission from ref. 19. Copyright McGraw-Hill, 2006.*

Let us consider a piezoelectric sample with area *A*, thickness *t*, and piezoelectric constant $d \equiv d_{33}$ along *t*. If $T = F/A$ is the applied stress in the direction of *t*, the induced polarization is $P = dT$, that leads to a surface polarization charge

$$Q = \sigma A = PA = dTA = dF \qquad \text{(Eq. 2.7)}$$

The capacitance of the sample is $C = \varepsilon_0 \varepsilon_r A/t$, thus the induced voltage is

$$V = \frac{Q}{C} = \frac{dFt}{\varepsilon_0 \varepsilon_r A} = \frac{gFt}{A} \qquad \text{(Eq. 2.8)}$$

where ε_0 and ε_r are the permittivity of vacuum and material, respectively. The constant *d* and the rate $g = d/\varepsilon_0 \varepsilon_r$, called the piezoelectric voltage coefficient, are fixed by the material. Therefore, the electrostatic energy is:

$$W = \frac{1}{2} CV^2 = \frac{1}{2} \frac{dgF^2 t}{A} \qquad \text{(Eq. 2.9)}$$

In a typical experiment, having chosen the material and the applied force *F*, one should maximize *t* and minimize *A* in order to get the highest *V* and *W* values. However, *t* is limited by the compliance and, *e.g.* by the characteristics of the entity that stress the piezoelectric cell. The minimum value of *A* is limited by the breakdown voltage *V* max and by the maximum stress $T = F/A$ supported by the

dielectric. Then *A* should be chosen to meet these constraints [20]. The piezoelectric materials used in devices can be in the form of polycrystalline ceramics, textured ceramics, thin films or polymers, depending on the desired frequency and vibration amplitude. Materials commonly employed for applications are: $Pb(Zr,Ti)O_3$ (PZT), ZnO, SiO_2 (quartz), AlN, $BaTiO_3$ (BT), and poly(vinylidene fluoride) (PVdF). In Table 2.1 the figures of merit of some of them are reported[21]. The most important materials for energy harvesting from human motion, due to their optimal piezoelectric performances, are PVdF and PZT. However, because the synthesis of both single crystal materials and polymers in large volume is challenging and expensive, polycrystalline or film samples are used. PZT polycrystalline ceramics are solid solutions with composition $PbTi_{1-x}Zr_xO_3$, where $0 < x < 1$ but typically $x = 0.5$. PZT components can be manufactured by standard sintering procedures, in which the powders are placed in a mold, compressed and treated at high temperatures, or by wet chemistry (*e.g.* sol-gel method). PZT is rigid, brittle, and heavy, so bringing limitations in wearable applications where flexibility and high strain tolerance are necessary. On the other hand, PVdF is a semi-crystalline high-molecular weight polymer with the repeat unit $(CH_2–CF_2)_n$. It has the advantage to be mechanically strong, resistant to a wide variety of chemicals, including acids, flexible and easy to handle and shape. Taking into account the human motion characteristics, PVdF is indeed more appropriate for wearable applications than PZT. The first energy-harvesting piezoelectric devices based on human walking were fabricated by Kymissis *et al.*[22]. They developed two types of insoles: one was made of eight-layer stacks of 28 mm PVdF sheets around a central 2 mm flexible plastic substrate; the other was a strip of spring steel bonded to a patch of PZT thick 250 mm. The PVdF stave produced ≈ 1 mW of average power, while PZT ≈ 2 mW, corresponding to net energy transfers of ≈ 1 mJ per step and ≈ 2 mJ per step, respectively. Afterwards, some other PVdF wearable energy harvesters implemented in shoes, bags and clothing were reported[20, 23, 24].

Table 2.1 *Electric properties comparison between commonly used piezoelectric materials.*

Material	Dielectric constant	Piezoelectric constant d_{33} [pC N^{-1}]	Piezoelectric voltage g_{33} [10^{-3} V m N^{-1}]
$BaTiO_3$	1700	191	12,6
Quartz	4,5	2,3 (d_{11})	50 (g_{31})
PVdF	13	-33	-339
PZT-4	1300	289	25,1

2.2.3 Electrostatic systems

The last energy harvesting category considered is that of electrostatic-based devices. This category is in turn divided into different classes based on the principle of charge separation and motion to produce energy: triboelectrification, reverse electrowetting on dielectric (REWOD) and electrostrictive polymer composites (EPCs)

2.2.3.1 Triboelectric effect

Triboelectricity is an electrostatic phenomenon well known since antiquity. It involves a physical contact between two materials with different electrostatic properties: when contact occurs, a charge separation takes place, leading to a positively charged material and a negatively charged one. If the materials are subsequently separated, a net potential difference occurs between them. Despite the mechanism of charge exchange between materials is not yet well understood, the triboelectric effect is involved in many technological products/processes, as well as in unwanted phenomena such as: xerography, self-cleaning wrapping materials, adhesion of powders on semiconductors, which necessitated the use of clean rooms, and many others. It is well known that not all the materials may be equally charged, in fact, some of them can bear a greater amount of

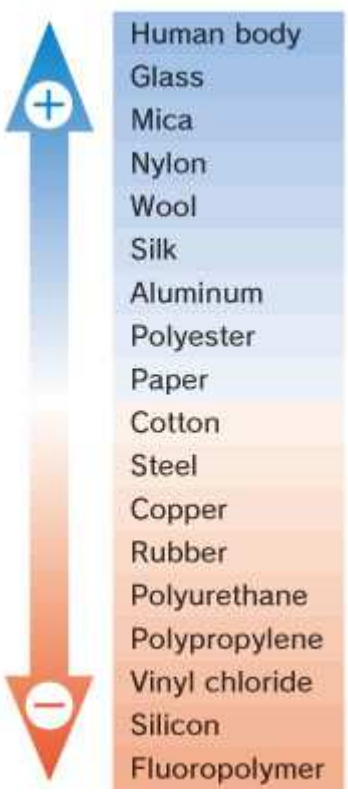

Fig. 2.8 *Triboelectric series, which lists common materials according to their charging affinity and intensity*

charge with respect to others. Furthermore, charge sign can be positive or negative depending on the nature of the involved materials, and their tendency to accept or give charges. A ‘‘triboelectric series’’ has been empirically defined (Fig. 2.8): it lists materials from those tending to be positively charged, to those tending to be negatively charged. The triboelectric series is a useful tool that permits to predict the sign and, roughly, also the extent of the charge separation, because materials that are close in the series will exchange a lower amount of charges with respect to those that are far from each other[25]. For example, rubbing a piece of Teflon™, that is the negative extreme of the series, with a piece of poly(vinyl chloride), we will obtain a charge separation (Teflon™-/PVC+) that is less than that available using Nylon® instead of PVC. As stated, triboelectric charges can generate a potential drop when two surfaces are separated by a mechanical force, which can drive electrons to flow between electrodes built on the surfaces of the two materials. This is particularly interesting when nanostructures are considered, which can give origin to significant power densities. Z.L. Wang reported the first harvesting device based on this phenomenon in 2012 and called it *triboelectric nanogenerator* (TENG)[26, 27]. Following the analysis reported by Wang and his group, there are four fundamental modes of TENG operation: (a) the vertical contact-separation mode; (b) the lateral sliding mode; (c) the single-electrode mode and (d) the free-standing mode (Fig. 2.9). In the vertical contact separation mode (Fig. 2.9a) a contact between the two dielectric films with distinct electron affinity creates oppositely charged surfaces. Once the two surfaces are separated by a gap, a potential difference is created between the electrodes deposited on the two dielectric films, and a current can be obtained across an appropriate load[26]

Periodic contact and separation between the two layers drive the induced electrons to flow between the two electrodes, resulting in an AC output in the external circuit. In the lateral sliding mode (Fig. 2.9b), when a displacement is produced by a force applied in the direction parallel to the interface of two materials with opposite triboelectric polarities, triboelectric charges are not fully compensated at the displaced/mismatched areas. This results in the creation of an effective dipole polarization parallel to the direction of the displacement, which in turn gives origin to a potential difference across the two electrodes. A sliding back and forth motion will then result in AC voltage (current). This mode can be practically obtained both with dielectric/dielectric and dielectric/metal interfaces. Fig. 2.9c illustrates the metal-to-dielectric contact case. A dielectric layer and a metal electrode are stacked to form a triboelectric pair, with the same length *l* and width *w*. A gap, *g*, is

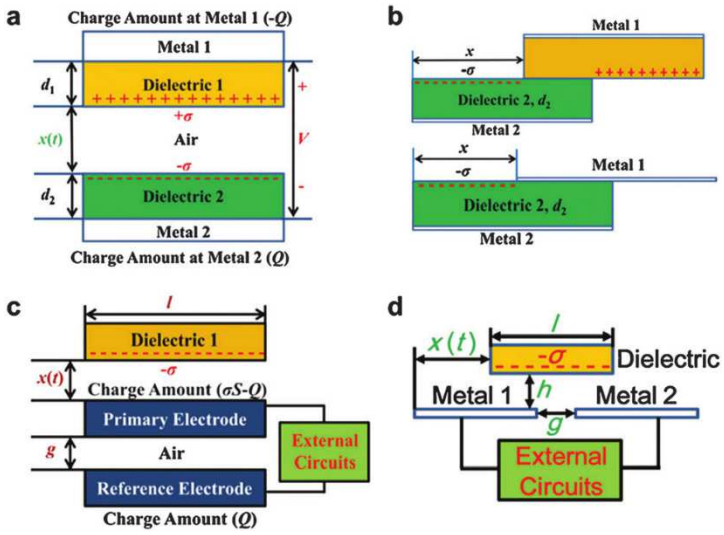

Fig. 2.9 *Modes of TENG operation. Reprinted with permission from ref. 27.*

made between the primary electrode and a reference electrode. The two electrodes are fixed, and the dielectric layer can move under the external mechanical excitation. In principle, the performances of the single electrode mode TENGs are limited by the electrostatic shielding effect of the electrodes. In the single electrode mode, one of the triboelectric layers can move freely without any restriction. This makes the configuration very versatile, and many applications have been tested to date. Finally, Fig. 2.9d reports a scheme of the free-standing mode. Here, a couple of symmetric electrodes are placed below a dielectric layer. The dielectric motion approaching and departing from the electrodes will induce an asymmetric charge distribution, provided it was preliminary charged by a triboelectric process. The oscillation of the electrons between the paired electrodes, in response to the back and forth motion of the object, produces an AC current output. Compared to the single-electrode mode, there is no screening effect here, and the electrostatically-induced electron transfer can reach the same amount of the triboelectric charges on the free-standing layer.

On the basis of the configurations possible to exploit this phenomenon, many devices has been developed to harvest different types of energies into electricity, and among these, also kinetic energy from human motion has been considered. Among the first to exploit triboelectrification for EH, L. Beccai and co-workers developed an interesting device based on the single electrode mode[27a]. They, using a porous sugar template made by an appropriate mold, were able to prepare a sponge PDMS matrix that, under the action of a compressive force, come into contact with the primary electrode generating an AC voltage (Fig. 2.10a). The final generator had a 3 cm^3 volume, that become 4 cm^3 considering the encapsulation of the sponge matrix. They also evaluated the

trend of the generated power as function of different variables and found that it increase with increasing frequency, amplitude of compression and sugar particle size (porosity of the final matrix). With this device, they obtained 1.22 µW of generated power applied 45% strain (compressive) at 9.5 Hz.

While the work of Beccai *et al.* still represent a proof of concept that will be improved and implemented, Z. L. Wang *et al.* developed a TENG device and tested it directly on a person during walking (Fig. 2.11a)[28]. In this work, they fabricated a tubular TENG, with inner electrode wrapped in a helical fashion, that can produce energy under different kind of deformations such as bending,

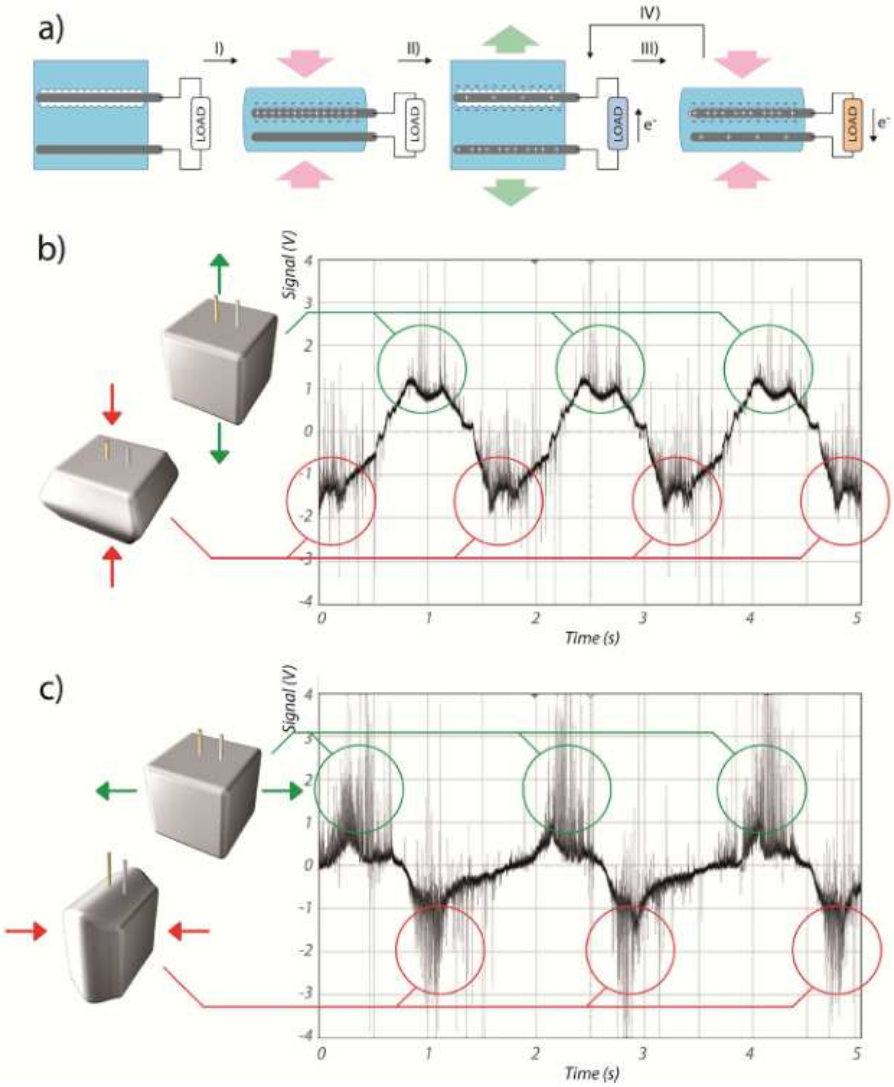

Fig. 2.10 *a) Mechanism of current generation; b,c) The open-circuit output voltage signal when the composite is compressed along two different perpendicular directions. The highlighted negative and positive peaks are shown to correlate with the compress. Reprinted with permission from ref. 27a.*

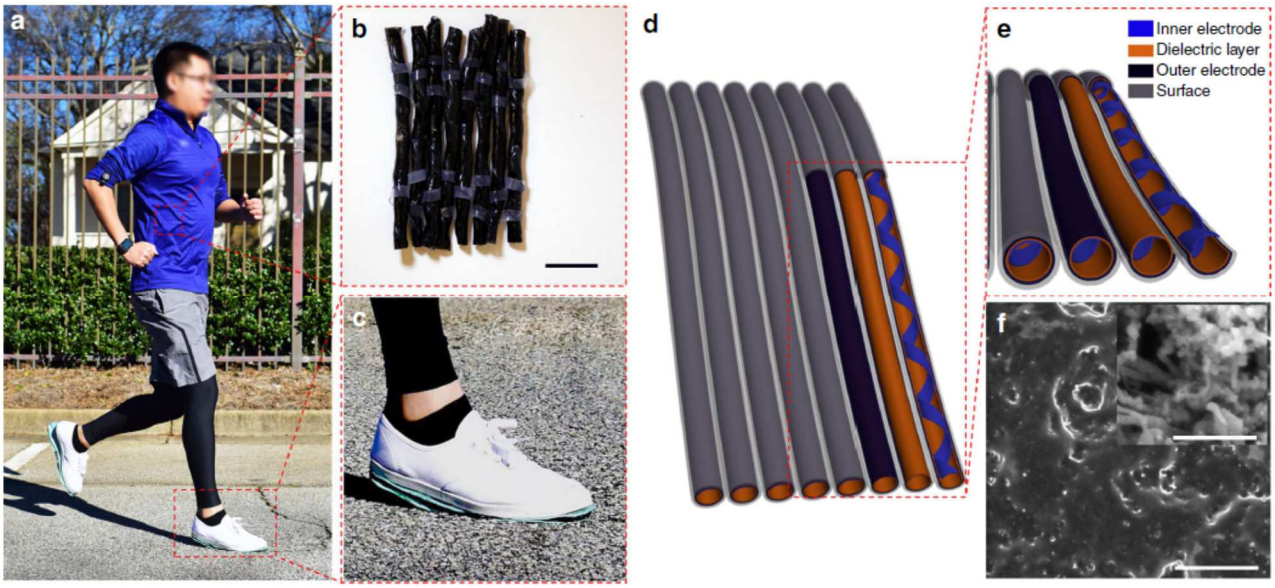

Fig. 2.11 *a) TENG assembled under a shoe sole and tested under real conditions, b) photo showing the textile-TENG tubes, c) zoom of the working TENG tubes under the shoe, d) Structure sketch of the TENG tubes; e) Enlarged view of the TENG structure; f) SEM image of the triboelectric electrode surface. The inset shows the SEM image of the carbon black/CNTs mixture, which is the conductive ingredient of the inner and outer electrodes. Reprinted with permission from ref. 28*

twisting and stretching. Inner and outer electrodes are composed by silicon rubber (Ecoflex 00-30) filled with both carbon black and carbon nanotubes (CNTs) in a 2:1 weight ratio (providing a nanostructured surface that improve charge separation), while the dielectric layer is composed by the silicon rubber itself. The device charge separation occur as depicted in Fig. 2.12a: (i) when the

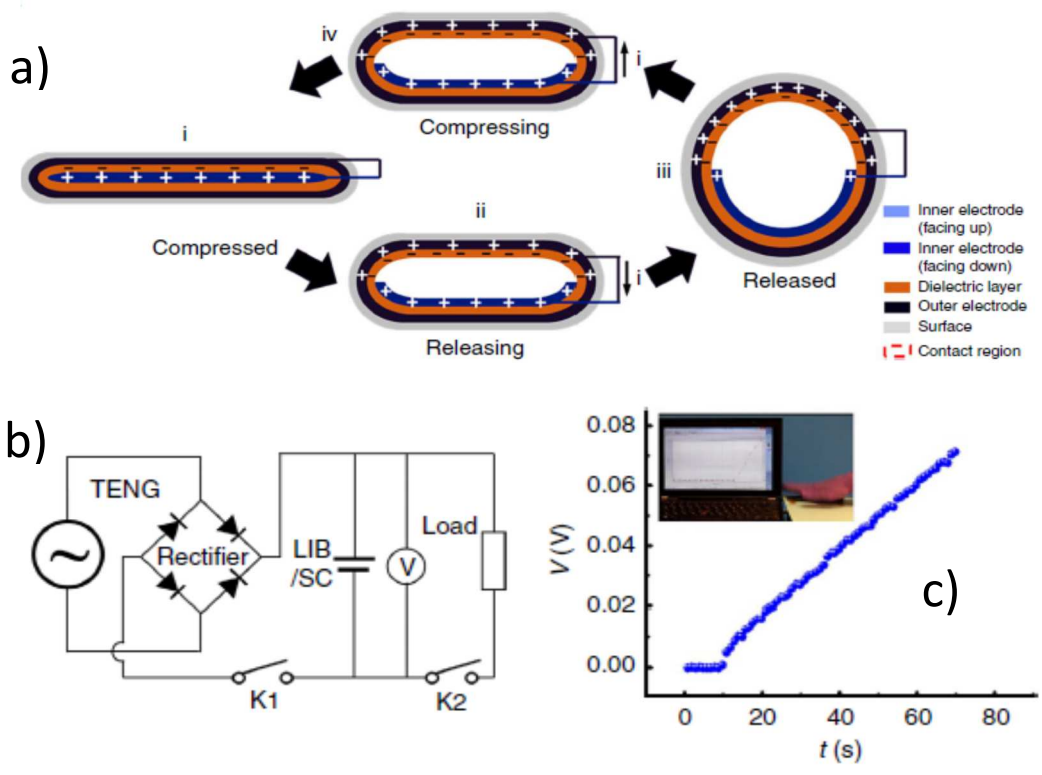

Fig. 2.12 *a) Steps of charge separation and AC current generation, b) power management circuit with LIB/SC supercapacitor store unit, c) voltage drop raising across the supercapacitor with TENG operation. Reprinted with permission from ref. 28.*

tube is compressed the dielectric layer (able to retain electrons) comes into contact with the inner electrode and charge separation take place; (ii) the tube release and positive charges are induced into the outer electrode, thus causing electrons movement from outer to inner electrode across the load until the charges are in equilibrium at stage (iii). Subsequently, a new step is starting and the charges in the outer electrode migrate again to the inner electrode (iv). In the same work, the researchers also tested a power management circuit that rectify the AC current and store it into a supercapacitor (Fig. 2.12b). As showed in Fig. 2.12c, the voltage drop across the supercapacitor raise with tapping on the TENG with a hand.

In another work, Z. L. Wang developed also a hybrid device the match the triboelectric and the piezo energy generation in a single unit[29]. This device is composed by a bridge-like PVdF film coated with gold electrodes and with the upper face protected by a polyimide (PI) film. The bottom side of the piezo unit face to the TENG unit that is composed of a PTFE film in contact with an aluminum electrode on its bottom side (Fig. 2.13a). This configuration permit to match the peak of energy generation of both the piezo and TENG units. During their work, they perform different tests and characterizations of the hybrid generator, by compressing the device with hand tapping (that correspond to about 0,2N force) they were able to charge, with the help of a power management circuit similar to that showed in Fig. 2.12b, capacitors of different sizes: 1µF, 10µF and 47µF were charged in 2,5, 25 and 47 seconds at 10V under a 5Hz excitation frequency. They perform also some practical experiments, again by hand tapping on the device (0,2 N, 5Hz) was possible to them to light up 550 LEDs connected in series and 600 LEDs connected in parallel. In conclusion, this hybrid device has a power density of about 4,44 mW cm^{-2}, a current generation density of 12 µA cm^{-2} and is able to produce a voltage output up to 370V when compressed with a force of 0,2 N.

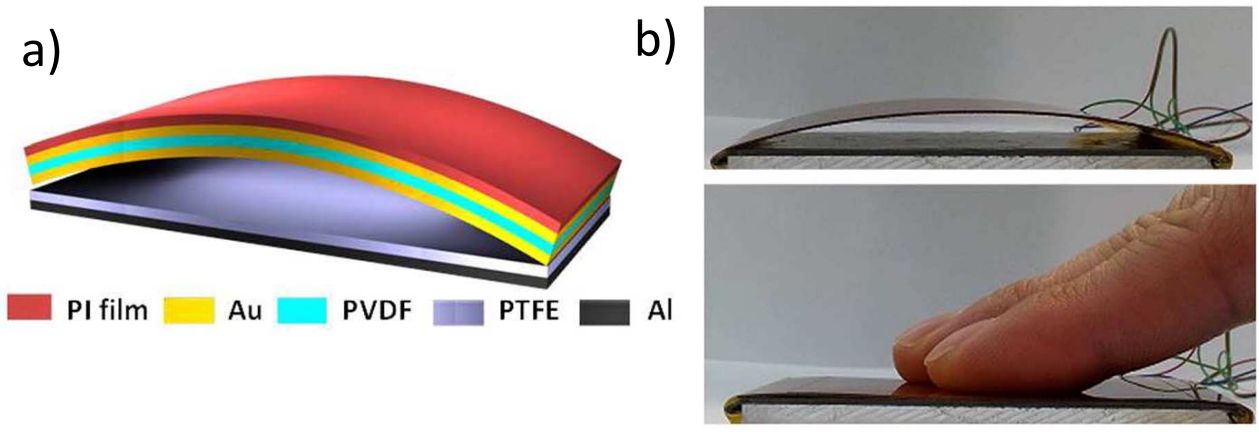

Fig. 2.13 *a) piezo-TENG Hybrid structure scheme, b) working mechanism of the hybrid generator. Up: relaxing state, bottom: compressed state. Reprinted with permission from ref. 29.*

2.2.3.2 Reverse electrowetting on dielectric (REWOD)

Another class of electrostatic energy harvester are that based on the inversion of the electrowetting phenomenon, called by its discoverers *Reverse ElectroWetting On Dielectric* (REWOD). The common electrowetting phenomenon consist in the change of the contact angle between a drop, of a partially wetting conductive liquid and a dielectric film (with thickness *d*) grown on a metal electrode, due to an applied potential difference *V* between the liquid and the electrode (Fig. 2.14 a-b). In 2011, T. Krupenkin and J. A. Taylor discovered that if the drop/dielectric contact area is mechanically modified when a potential difference is applied, this lead to an AC current generation due to charges movement[30]. As shown in Fig. 2.14c and d, an external mechanical force is used to periodically deform the droplet, thus inducing a periodic change in the contact area *A* between the droplet and the dielectric-coated electrode, which are connected to a bias voltage *V*. This periodic change in the contact area induces a change in the electric capacitance *C* and forces electrical current to flow back and forth across the load resistor, thus converting mechanical work into electrical energy. The electrostatic energy accumulated by the capacitor is $U_1 = C_M V^2/2$, where C_M is the maximum capacitance and is defined as $C_M = \varepsilon_0 \varepsilon_r A_M/d$ (with A_M=maximum contact area). When the external force stops working, the droplet relaxes, and *C* decreases. The initial charge Q_M is forced back across the load resistor, causing a current *I* with the opposite direction due to the discharge of the capacitor and producing the energy $U_2 = Q_M V = C_M V^2$

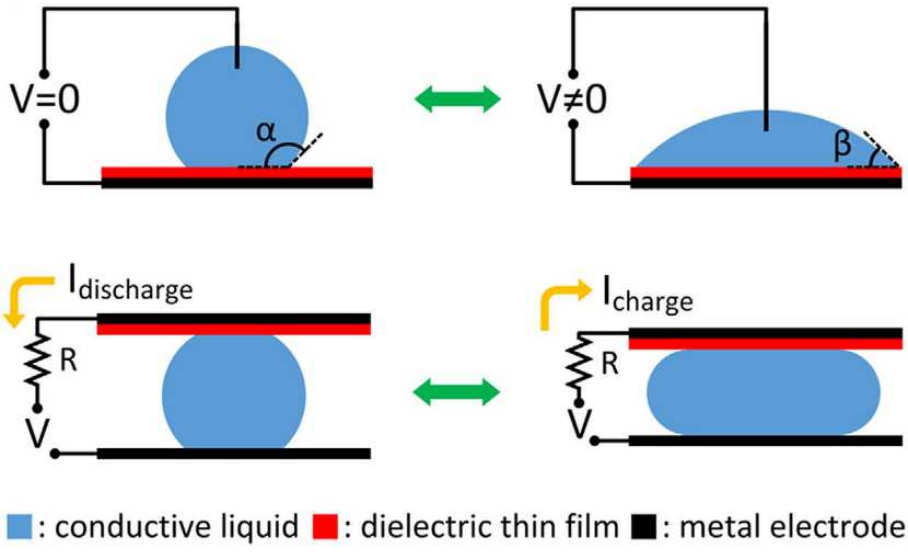

Fig. 2. 14 *Schematic of the electrowetting (a and b) and reverse electrowetting (c and d) processes. Reprinted with permission from ref. 30.*

(Q_M=$C_M V$, maximum charge on the capacitor). Thus, the net energy recovered during one cycle, which is due to the work done by the external force during the compression phase, is given by:

$$U = U_2 - U_1 = \frac{c_M V}{2} \quad \text{(Eq. 2. 10)}$$

The power output of the REWOD chip can be obtained by analyzing the electrical circuit shown in Fig. 2.15b, which his described, during the relaxation process, by the following equation:

$$V_C - V = IR \quad \text{(Eq. 2. 11)}$$

where $V_C = Q/C > V$ is the transient voltage on the capacitor, *C* is the time-dependent capacitance, and $I = -dQ/dt$ is the discharge current. It follows that:

$$\frac{dQ}{dt} + \frac{Q}{RC} - \frac{V}{R} = 0 \quad \text{(Eq. 2. 12)}$$

If the dependence of *C* vs. *t* is known, the differential equation in *Q(t)* can be numerically solved, and the energy *U* generated during one oscillation period, *T*, is given by

$$U = \int_T \left(\frac{dQ}{dt}\right)^2 R dt \quad \text{(Eq. 2. 13)}$$

from which the average generated power $\langle P \rangle = U/T$ can be obtained. The electric power can be increased by increasing *V* or *C*. Krupenkin and Taylor reported three major designs exploiting vibration, shear and pressure (Fig. 2.15a), which may be represented by the equivalent electric circuit of (Fig. 2.15b). More recently, Krupenkin *et al.* presented a new REWOD method, called *Bubbler*, showed in Fig. 2.15c-d. A pressurized dielectric fluid (air) is supplied through the holes in the REWOD chip causing dielectric bubbles to grow and displace the conductive liquid. This reduces the area of overlap between the conductive liquid and the thin-film dielectric-coated electrode: as in the previous methods, the *C* value of the capacitor decreases and the equivalent electrical circuit is the same as in Fig. 2.15b.

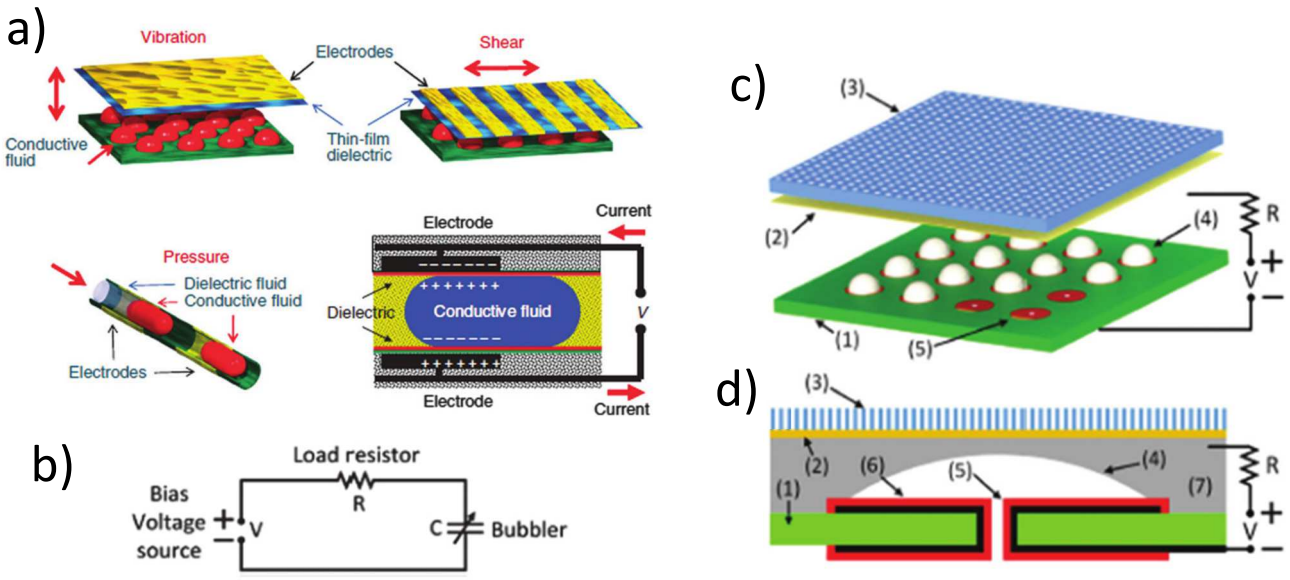

Fig. 2.15 *Schematics of three major droplet actuation mechanisms: include a) droplets between oscillating plates, droplets between sliding plates and droplets in a microchannel. b) Equivalent electrical circuit of the REWOD chip. c) Bubbler conceptual design: (1) indicates a REWOD chip, (2) membrane, (3) top plate, (4) an array of bubbles, and (5) an array of electrodes. (d) Schematics of a simplified single-electrode device used in the experiment: (1) represents the REWOD chip, (2) membrane, (3) top plate, (4) bubble, (5) metal electrode, (6) dielectric coating, and (7) conductive liquid. Reprinted with permission from ref. 31.*

In order to increase the power produced in a REWOD process, the applied bias voltage V and the capacitance C between the droplet and the dielectric-coated electrode should be increased. Higher C values require thinner dielectric films with high permittivity; however the d value is limited by the maximum electric field that can be applied to the dielectric material without exceeding the breakdown voltage V_{max}. In the first device developed by Krupenkin, the back electrode is a 1 µm thick Ta layer sputter-deposited on a quartz substrate. Then Ta was anodized to obtain a 200 nm thick tantalum pentoxide (Ta_2O_5) dielectric film. The Ta_2O_5 was chosen due to its relatively high permittivity ($\varepsilon_r \approx 25$) and the high DBS, allowing a bias voltage $V \leq 100$ V. C values up to 10^2 nF cm^{-2} were obtained.

In order to reduce contact line hysteresis and surface charge trapping occurring at the droplet–dielectric film interface during dewetting stage, which reduces energy production, the Ta_2O_5 film was spin-coated with a thin dielectric film of a fluoropolymer (Cytop^{TM}). A number of conducting liquids such as aqueous salt solutions, molten ionic salts, and liquid metals showed the REWOD effect. However, liquid metals proved to be the best, due to high electrical conductivity, low vapor pressure and higher surface tension, which increases the surface energy density. Most common metals remaining liquid at room temperature are Hg, Ga and Ga/In/Sn alloy (Galinstan^{TM}). Droplets of Hg and Galinstan^{TM} show similar good performances in the REWOD methods: Hg is highly toxic, whereas Galinstan^{TM} is less toxic and widely used in commercial products; however, it oxidizes

almost instantaneously when exposed to air, and thus it should be used in sealed systems. An array of 1000 Hg or Galinstan™ droplets, between oscillating plates (Fig. 2.15a), each droplet with the maximum overlap area A_M=1 mm^2 and C=16 nF cm^{-2} generated an average power per foot between 2 W and 10 W, using bias voltages between 35 V and 75 V, respectively. In the *Bubbler* method (Fig. 2.15c-d) the compressed air supplied through the inlet (diameter between 140 and 200 µm) grows the bubble until its surface touches the membrane, breaking the Hg film (thick 100–130 µm). At this point the bubble starts collapsing toward the center of the electrode, thus inducing volume self-oscillations with a period of 0.5–1.5 ms, depending on Hg thickness, inlet diameter, mercury and air pressures. The results relative to a footwear-embedded harvester device with 800 electrodes, each with a 1 mm^2 diameter, and a total area of 628 mm^2 are reported. The device operates a 30 V bias voltage and a self-oscillation frequency of 2 kHz. The average power output, at one step per second walking cadence, is ≈1 W[31].

2.2.3.3 Electrostriction

A further class of energy harvesters for human gait are that based on electrostriction phenomenon. Electrostrictive polymers (EPs) belong to the larger family of electroactive polymers (EAPs) that includes all the polymeric materials that give any kind of response because of an electric stimuli. Based on the phenomenon that causes the response, EAPs are divided into *Ionic EAPs*

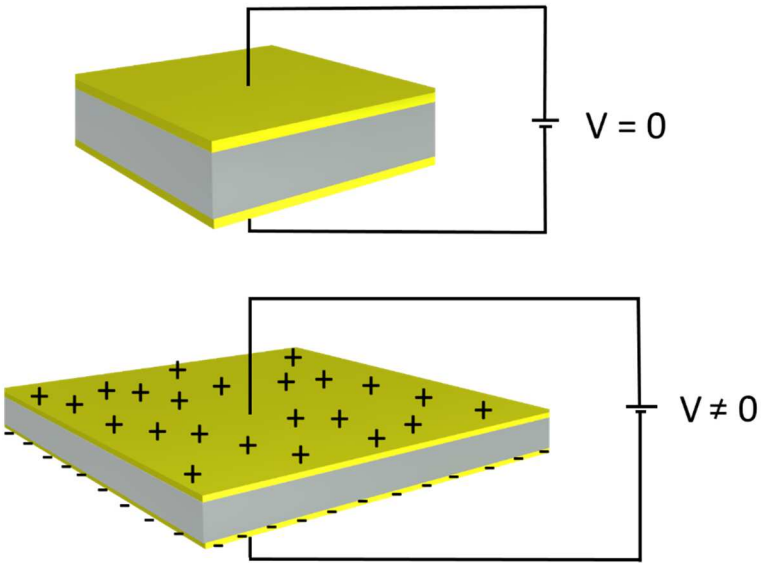

Fig. 2.16 *Electrostrictive response of an electrostrictive polymer under applied voltage.*

(displacement of ions through the matrix) and *Electronic EAPs* (drived by electric field or coulombic forces). Depending on EAP class, the type of response obtained when electrically stimulated change: for example, Ionic polymer metal composites (IPMCs), a type of ionic EAPs, bend when subjected to an electric field through thickness. On the other side, electrostrictive polymers, that are electronic EAPs, are able to decrease their thickness and increase their area as response of the applied electric field. This is due to *Maxwell stress* exerted by the opposite electrodes of the EPC: positive and negative charges attract each other causing a decrease in thickness in the film, while the repulsion of charges with the same sign, accumulated on one electrode, causes a uniform strain in the film that in turn increase its area. However, has been found that Maxwell stress account for only 15% of the total strain experienced by a stimulated film[32]. *Intrinsic electrostriction,* due to microscopic effects, shows to be responsible of 85% of the response in EPs. In fact, measured strains on phase-separated (PS-PU) and phase-mixed (PM-PU) polyurethane elastomers shows that PM-PU possess higher electrostrictive coefficients: this is due to the larger quantity of hard/soft segments interfaces, that works as space-charge trapping sites causing a non-uniform distribution of the electric field in the film, that in turn enhance the electrostrictive response[33]. Electrostriction occur in all dielectric materials subjected to an electric field. In the same way work dielectric elastomers actuators (DEAs) and generators (DEGs), but with substantial difference in respect to EPs. DEAs and DEGs (commonly silicones or acrylates) needs very high electric field intensity in order to perform a significant response or energy generation (40-120 MV/m)[34], while EPs needs lower electric field (10-40MV/m) to achieve the same, or even better, performances[35].

Electrostriction is commonly defined as the quadratic coupling between the strain and the applied electric field. From the Devonshire formalism of the thermodynamic phenomenology, electrostriction is a fourth rank tensor property relating the mechanical strain *S* to an applied electric field *E*, or to the polarization *P*, expressed by the following relationships:

$$S_{ij} = s^{E}{}_{ijkl} T_{kl} + M_{mnij} E_m E_n \qquad \text{(Eq. 2.14)}$$

$$S_{ij} = s^{P}{}_{ijkl} T_{kl} + Q_{mnij} P_m P_n \qquad \text{(Eq. 2.15)}$$

where s_{ijkl} is the elastic compliance tensor under appropriate boundary conditions, T_{kl} is the elastic stress component, and M_{mnij} and Q_{mnij} are the electrostriction coefficients[36].

Since their discovery, electrostrictive polymers were employed as actuators due to their capacity to generate a displacement under electrical stimuli. More recently, this class of materials were also employed as generators[37], particularly suitable for high-strain low-frequency activations, where piezoceramics, piezoelectric polymers (PVDF) and inductive systems are less efficient due to stiffness, energy generation and frequency of activation, respectively. Y. Liu *et al.* were among the first the explore this kind of employment of electrostrictive polymers[38]. They evaluated the energy generation densities of polyurethane and a PVDF-based terpolymers, under different electrical boundary conditions: constant field, open circuit, constant field-open circuit and passive diode. They found that electrostrictive polymers are significantly more efficient at harvesting energy in small devices with low frequency of excitation, compared with piezoelectric and inductive systems. However, the performing of such boundary conditions results quite tricky to be transposed to a practical device.

More recently, D. Guyomar *et al.* developed a new energy harvesting mode called *pseudo-piezoelectric* [36]. This mode concern the application of a polarizing DC-bias electric field to the film, that upon excitation (stress/relax cycles) is able to produce an alternated current. This mode produces less energy if compared with electrical cycles performed by Y Liu *et al.*[38], but can be easily applied into realistic conditions, without complications in the electronic management. In the same work, they also defined the affecting variabilities that permit to maximize the energy generation. They observed that maximization of bias electric field, frequency, strain and derivative of strain permit to enhance the harvested current in this arrangement. In a related work, they discover that, apart from experimental conditions, the relative dielectric permittivity (ε_r) of the EP is a key property in energy generation maximization[39]. To achieve higher ε_r there are different ways: i) synthesis of new high-k elastomeric polymers, ii) polymer blend and iii) polymer composites. Among different manners to increase ε_r, the incorporation of high-k filler into a polymeric matrix represents an immediate and simple way, and also permit versatility due to potentially endless combinations of polymer matrices (commercial or synthesized) and fillers. Electrostrictive polymer composites (EPCs) can be fabricated by incorporation of conductive or insulating fillers. The first type permit to increase ε_r at low %loadings, maintaining almost unchanged the mechanical properties of the polymer, but percolation threshold and increase of conductivity of the resulting EPC limit the percentage of filler that can be incorporated. On the other hand, high-k dielectric fillers permit to enhance the ε_r without increase in conductivity, but needs higher loadings (up to 50%wt) to be effective, leading in some cases in Young's modulus *Y* and stiffness increase in the final EPC. Despite

the disadvantages related to the different kind of filler employed, P.-J. Cottinet *et al.* reported a significant increase in the harvested power when, both conductive or insulating, fillers are incorporated into the polymeric matrix, as depicted in Fig. 2.17.

In this optic, recently J.-F. Capsal and co-workers obtained energy densities up to 4.14mW/cm^3 per cycle, using the high-k relaxor ferroelectric terpolymer p(VDF-TrFE-CTFE) blended with 2.5%wt of a DEHP plasticizer, which constitutes the best energy generation result in this field.

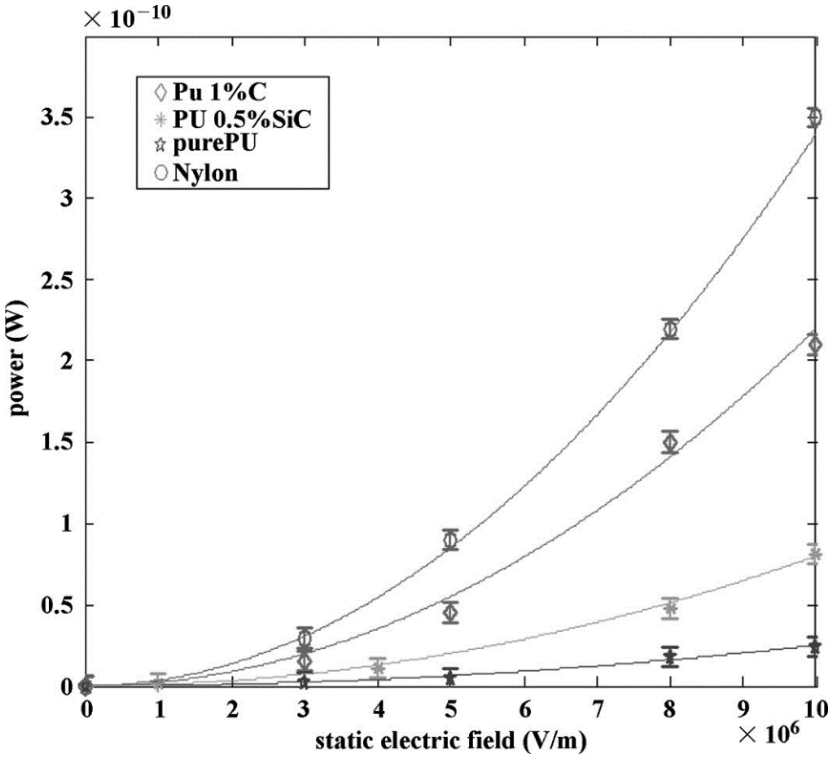

$$\varepsilon_{r\,Nylon} = 12$$

$$\varepsilon_{r\,purePU} = 4.8$$

$$\varepsilon_{r\,PU\,1\%C} = 8.3$$

$$\varepsilon_{r\,0.5\%SiC} = 5.1$$

Fig. 2.17 *Harvested power as function of the applied electric field for different polymers and EPCs. Reprinted with permission from ref. 39.*

3. Materials and methods

When investigating new materials and/or devices, different instruments and processes are needed to achieve the goal. In particular, instrumentation can be divided into that useful from preparation of samples, *e.g.* deposition techniques, and that used to characterize their properties or composition. In this chapter, I will face with the technical aspects of this research project, meaning the synthesis and/or preparation of the materials involved in the energy conversion systems, the techniques used to process them to be tested in the energy harvesting configuration and all the instrumentation used to characterize their chemical and physical properties. Moreover, in this section, I will treat also the design and optimization of a homemade measuring system, developed to characterize the energy harvesting properties of the materials and systems investigated.

Since the mechanisms to perform mechanical-to-electrical conversion are different for each physical phenomena (REWOD or electrostrictive polymers), and because energy harvesting is still a niche field of research, no industrial and validated measuring instruments are available on the market to characterize the harvesting properties of the materials involved in energy conversion. Due to this lack, a significant part of this research project was focused on the design, development and optimization of a measuring system able to perform mechanical-to-electrical energy conversion of different energy harvesting devices, simulating the human walk/run conditions. In particular, the measuring instrument had to be able to apply compression and/or tension forces to the analyzed sample, at different frequencies (to simulate walk or run), and at different applied electric fields and, at the same time, to measure the energy generation.

3.1 REWOD materials fabrication

The reverse electrowetting on dielectric (REWOD) is an electrostatic phenomenon, that produces energy as a consequence of a capacitance change in a parallel plate variable capacitor, where one of the two plates can be mechanically modified. Among the different variables affecting the process, the *dielectric layer* is one of the most important. During this research project, we focused on the investigation of new materials to be employed as dielectric layers for REWOD energy harvesting systems, and on different fabrication processes, with respect to the literature.

In this project, we employed the *cathodic magnetron sputtering* process to deposit the dielectric films. This technique allows depositing from nano- to micro-metric films of many materials, including insulating ones, with the help of an ablating ionized gas. In a chamber under vacuum an Argon (Ar) flux (or a mixture of it with other sputtering gasses like oxygen) is injected, which is ionized (Ar^+ plasma) by an appropriate electric field. The Ar^+ ions accelerate towards the cathode, where the material to be deposited (called *target*) is placed, so extracting single atoms, or atom clusters, from the target. Then, the ablated atom travels through the chamber for a distance, called *mean free path*, which can be calculated by the following equation:

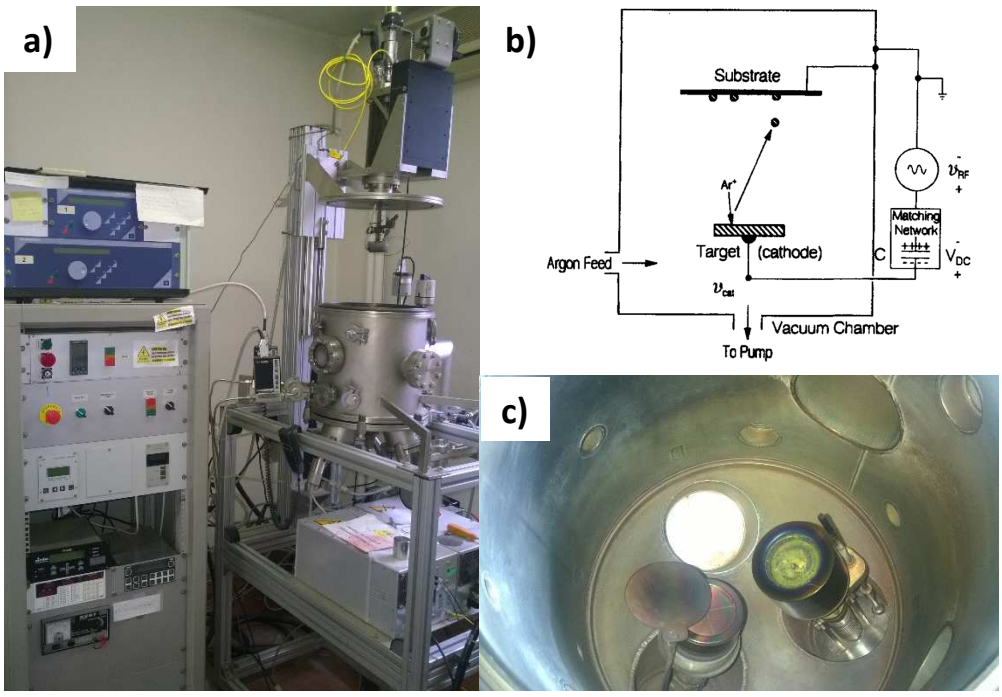

Fig. 3.1 *a) Sputtering system used to deposit thin dielectric films. Left: electronic console; right: vacuum chamber and matching boxes; b) scheme of an RF-sputter system; c) oblique cathodes inside the vacuum chamber.*

$$\lambda\,[cm] = \frac{5 \cdot 10^{-3}}{P\,[Torr]} \qquad \text{(Eq. 3.1)}$$

Inside this distance range the substrate to be coated is placed. There exist different types of sputtering systems, during this work I used a radiofrequency (RF) sputtering system, showed in Fig. 3.1a. This technique allows depositing also dielectric materials, thanks to a high-voltage power supply working at 13.56 MHz. In particular, our RF-sputtering instrument has a confocal configuration with three cathodes, which allows depositing up to three different materials consecutively (layer-by-layer deposition) or simultaneously (co-deposition).

Before to perform the dielectric layer deposition, the substrate must be previously cleaned. The substrate used in this project is oriented silicon (100), obtained from cutting of the native wafer (MEMC Electronic Materials, CZ P-doped (B), 16-24 Ω cm^{-1}, thickness 600-650 µm, orientation: 100). A common cleaning process, described in detail in Table 3.1, was carried out before to use silicon substrates, to eliminate all the impurities, organic and inorganic, as well as the native oxide from the surface. Cleaning process is composed of three consecutive steps to afford a complete cleaning of the Si wafer. Briefly, step one affords a first and mild clean from organic impurities present on the substrate; since acetone can bring impurities itself, if not highly pure, subsequent methanol washing guarantee a complete clean from organic impurities. The second step involves surface oxidation, by NH_4OH/H_2O_2 solution bath, which decomposes all the obstinate impurities on the substrate. With this step, a SiO_2 layer, more or less thick depending on the time duration of this treatment, is formed, changing the surface of the substrate. Thus, third step is needed to remove

Table 3.1 *Cleaning process for Si wafer before sputtering deposition.*

Solvent cleaning (1° step)	RCA clean (2° step)	HF dip (3° step)
Soaking in acetone (10 min)	Prepare the RCA bath[a]	Prepare 2% HF solution[C]
Soaking in MeOH (5 min)	Wait for RCA bath activation[b]	Soak Si in HF sol. (2 min)
Wash with DI water	Soak Si in RCA bath (15 min)	Wash with flowing DI water
N_2 blow dry	Wash with DI water	Hydrophobicity test[d]

a) 5 parts of water; 1 part of NH4OH (27%); 1 part of H2O2 (30%); b) when, after 2 minutes, the solution starts to bubble the RCA bath is ready; c) 48ml of water + 2ml of HF (49%); d) Pour a little DI water drop on the Si surface, if the water beads up and roll off the test is positive, otherwise repeat the HF cleaning.

this unwanted layer and restore Si atoms on the surface. This step involves the soaking of the Si wafer into a diluted HF solution bath. As well known, HF dissolves SiO_2 leaving only Si atoms on the surface, which in turn are themselves subjected to dissolution when exposed to F^- ions. Therefore it is important to restrict the soak duration of HF bath in order to eliminate only the unwanted SiO_2 present on the surface. To do this, Si wafer have been immersed in an HF bath and at 2 minutes intervals of HF exposition, the substrates were extracted, washed and subjected to a hydrophobicity test (see Table 3.1 caption), to check for the complete dissolution of the SiO_2 layer.

Once the substrate has been cleaned, the deposition step can be started. In a typical deposition process, the substrate to be coated is placed on an appropriate support (with shape and dimensions that changes depending on the substrate), that is fixed, facing down, to the substrate holder by several screws. The support maintains the substrate face down, preventing its falling, and acts as mask for the deposition of the active material. The deposition target is placed on the cathode. Depending on the target form, bulk or powder, it can be directly placed on the cathode or gently pressed in an appropriate container, respectively. Following these preparing step, the vacuum chamber is closed and evacuated with the help of a turbo-mechanical pump to obtain a pressure of about 10^{-3}-10^{-4} mbar. When vacuum becomes stable, Ar gas (or a Ar/O_2 mixture) can be injected, and the chamber pressure is adjusted to the desired value by controlling the opening of the turbo pump electro-valve. The temperature of deposition can be controlled by means of a heating element placed near the substrate holder. When both chamber pressure and temperature are stable, the deposition is started by turning on the Ar^+ plasma. Then, the RF power is raised until the desired value, and the target material is let to deposit for a time chosen by the operator. To stop the deposition experiment, the power supply, the turbo pump and the mechanical pump are turned off sequentially, and finally the atmospheric pressure is restored by opening the manual valve on the chamber.

Table 3.2 *Sputtering deposition conditions for REWOD materials.*

Target material	Temperature [°C]	Dep. Pressure [mbar]	Power [W/cm^2]	Ar flux [sccm]	O_2 flux [sccm]
Ta	600	$1{,}4 \cdot 10^{-2}$	5,5	20	3,5
ZrO_2	rt	$9 \cdot 10^{-3}$	2,5	10	1,5
PTFE	rt	$5 \cdot 10^{-2}$	2,5	20	-

Table 3.2 briefly summarizes the deposition conditions used during this research project to deposit the dielectric layers for REWOD systems. In the case of Ta_2O_5 deposition, an Ar/O_2 mixture was used to perform a reactive sputtering deposition, in order to obtain the oxide starting from the Ta metallic target, while for ZrO_2 deposition, oxygen was inject anyway to avoid oxygen under-stoichiometry, which is a typical problem of RF sputtering depositions due to low impinging coefficient of oxygen atoms. For PTFE deposition, a disc of Teflon™ was obtained from a cylinder by lathing, cleaned and placed on the cathode.

3.2 Electrostrictive polymer composites (EPCs)

Each material when placed between two electrodes that apply a potential difference become polarized. The polarization consists in the alignment of dipoles with the electric field and in a slight displacement of the ions in the crystal lattice. This alignment/displacement causes a reduction in thickness and an increase in area, depending on the stiffness of the material polarized. This phenomenon is commonly called *electrostriction*, which is generally defined as a quadratic coupling between strain and applied electric field. Recently, several research groups around the world observed that subjecting an electrostrictive material to an electric field and stress/relax cycles at the same time, lead to AC current generation. Since the dielectric permittivity (ε_r) was found as a key material parameter to improve the energy generation[40], during this research project we focused on its improvement by incorporation of an high-k dielectric ceramic material.

The composite we investigated was made by a polyurethane matrix (Estane 58887 – Lubrizol Corp.), in which we incorporated Calcium Copper Titanate ($CaCu_3Ti_4O_{12}$, CCTO) nanopowder at different volume ratios; abbreviated as "*TPU-CCTO x vol%"*, where *x* identifies the percentage number of CCTO volume incorporated. A typical fabrication process starts with the synthesis of the $CaCu_3Ti_4O_{12}$. The filler was obtained by a sol-gel synthesis according to the literature[41]. Appropriate amounts of $Ca(NO_3)_2{\cdot}4H_2O$ (1 equivalent) and $Cu(NO_3)_2{\cdot}2.5H_2O$ (3 eq.) were dissolved in 50ml of distilled water. In a separate beaker $Ti(iPrO)_4$ (4 eq.) was mixed with acetylacetone (acac, 4 eq.) and stirred together for 10 minutes. After this, an aqueous solution of citric acid (4 eq, 0.6M) was poured into the $Ti(iPrO)_4$/acac mixture and stirred for 30 minutes. Subsequently, the water solution, containing Ca and Cu cations, was dropped into the mixture over 10 minutes. The final solution was heated until complete evaporation of the solvent and burning of the blue gel, obtaining a dark brown-black powder that is treated at 300°C for 3h, then grounded and calcined at 800°C for 30 minutes. Finally, the brown powder obtained was ball-milled with some drops of ethanol for 4h at 200rpm, to afford the final nanopowder.

TPU-CCTO composites were obtained by solvent casting method. In a typical lab-scale preparation procedure, 1.5g of TPU granules (Estane 58887, pellets) were dissolved into 15ml of dimethylacetamide (DMAc, 99%) under stirring at 50°C. After the dissolution was complete, CCTO nanopowder was added and sonicated for 3h, in order to break the aggregates and disperse homogeneously the filler into the TPU solution. After the sonication step, the suspension was poured onto a glass sheet and heated at 80°C in an oven, to evaporate the solvent. Finally, the

resulting film was peeled off from the glass sheet, and heated again at 80°C under vacuum to completely dry it from solvent traces. The final film thickness ranges between 30 and 100 µm, depending on how much the TPU solution concentration and how it has been spread on the glass sheet. Once obtained the film, it was possible to proceed to the preparation of the energy harvesting test sample. The film was cut into strips of 2x5cm, placed on a microscope glass and masked with scotch tape to let exposed a 1.5x4.5cm rectangular surface. Subsequently, the masked film was placed into a sputter chamber and coated with a thin film of gold, to obtain a stretchable electrode. The same process is repeated for the opposite face of the film strip. The two gold electrodes were obtained in a non-symmetrical fashion, as depicted in Fig. 3.2, to allow contacting and layers sandwiching.

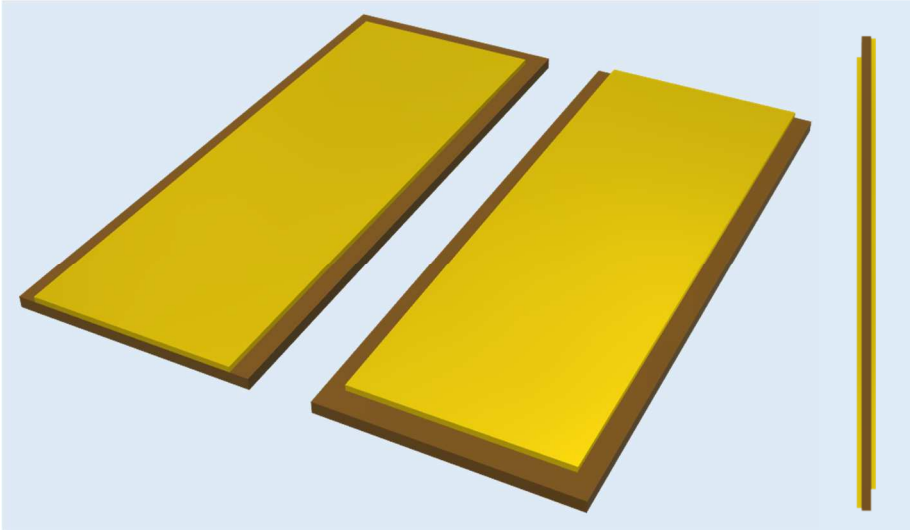

Fig. 3.2 *Prospective and frontal vision of asymmetric sputtered gold electrodes on TPU-CCTO film strips.*

3.3 Energy harvesting measuring instrument: design and development of the prototype

As said before, a suitable measuring instrument should be able to perform, simultaneously, different tasks in order to carry out the characterization of the energy harvesting capabilities of a system. At the same time, the instrument should simulate the behavior of a foot during human gait. In this frame, during the design of the instrument, we chose to develop a vertical system able to simulate both the impact of the heel to the ground, and the tension developed at the metatarsal of a foot. The first one, since the heel is a preferential zone in terms of available mechanical energy and space to place a possible device[10]; while the metatarsal region develops the tension needed to stretch the electrostrictive films. As showed in the Fig. 3.3, the prototype system consists of a vertical arrangement of a pneumatic piston fixed to an appropriate metallic structure. This piston provides the up-down controlled movement useful to simulate both the heel pressure on the ground and the metatarsal tension. The mechanical drive is actuated by compressed air. Therefore, by acting on the pressure value, the velocity of the piston movement can be controlled, and the same holds for the mobile part of the test cells, described in detail later. This is possible thanks to a pressure gauge (Fig. 3.3, right), placed between the compressor and the piston, that permits to measure and control the pressure value provided to the piston, usually set at 2 bar, in order to

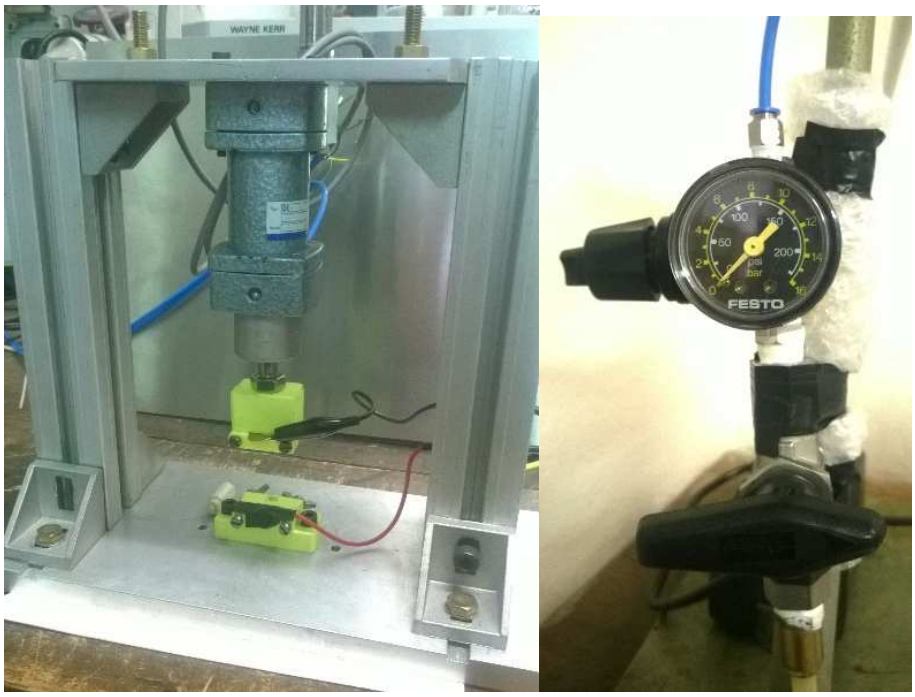

Fig. 3.3 *Left: measuring instrument structure (with EAP test cell mounted on); Right: pressure reducer between compressor and piston.*

Fig. 3.4 *Arduino program used to control piston movement, cycles and frequency.*

obtain a realistic walk simulation. Once the pressure value was set, the compressed air must be directed into the piston to move it up and down. This is possible by controlling four electrovalves directing the air that comes from the pressure gauge. In turn, the electrovalves are controlled by the microcontroller board Arduino Uno™, that is able to activate them alternatively to perform up/down cycles. In Fig. 3.4 the program used for control the electrovalves is showed. By changing the time values of up and down steps (called *ts* and *td* [ms]) and the *N* value, it is possible to control the frequency and the number of cycles of the simulated walk.

In order to selectively perform pressure or tension measurement, different test cells were designed and fabricated. In Fig. 3.3 we showed the test cell for electrostrictive films characterization, mounted on the instrument. In particular, it is composed of two specular jaws, one of them fixed to the basement of the structure, and the other one free to move with the piston rod. Each jaw contains an electrical contact (a metallic sheet) connected to the stretchable electrode of the filmstrip, in order to build a stretchable capacitor system. Thanks to these jaws, the film can be clamped at its ends and stretched at given amplitude, frequency and velocity, depending on the program preset (Fig. 3.4). In Fig. 3.5a a detailed photo of the mobile jaw is reported, where: i) the

inner electrical contact (thin brass plate), and ii) the screws used to maintain clamped the film also under mechanical strain are evident. Each jaw was provided by opportune threaded holes for fixing to the basement and to the piston shaft.

For REWOD measurements, another test cell was used, showed in Fig. 3.5b-c. This test cell is composed of three parts: 1. bottom electrode contact, fixed to the basement, providing electrical contact with the lower part of the capacitor and serving as housing for the second part, that can be blocked by the four screws on the sidewalls; 2. A liquid electrode container, constituting the central part of the test cell, which guarantees the confinement of the liquid electrode (mercury, Hg); this part houses the bottom electrode and provides a guide for the piston movement and 3. mobile upper electrode, which provides the second electrical contact and transmits the mechanical energy to the device. Due to their complex shape, first and second parts were 3D-printed (STRATASYS, Object30 Pro) in order to obtain a good matching between them, while the *mobile upper electrode* part was obtained by lathing a cylinder piece of Teflon^{TM}. The electrical contacts were made with stainless steel. Fig. 3.5c shows the assembled cell, with the electrical contacts that come from the respective electrodes.

Until now, we described the mechanical aspects of the instrument, focusing on how the mechanical energy (simulated human walk/run) is transferred from the machinery to the energy harvesting system. The other main aspect of the instrument is concerned with the measuring

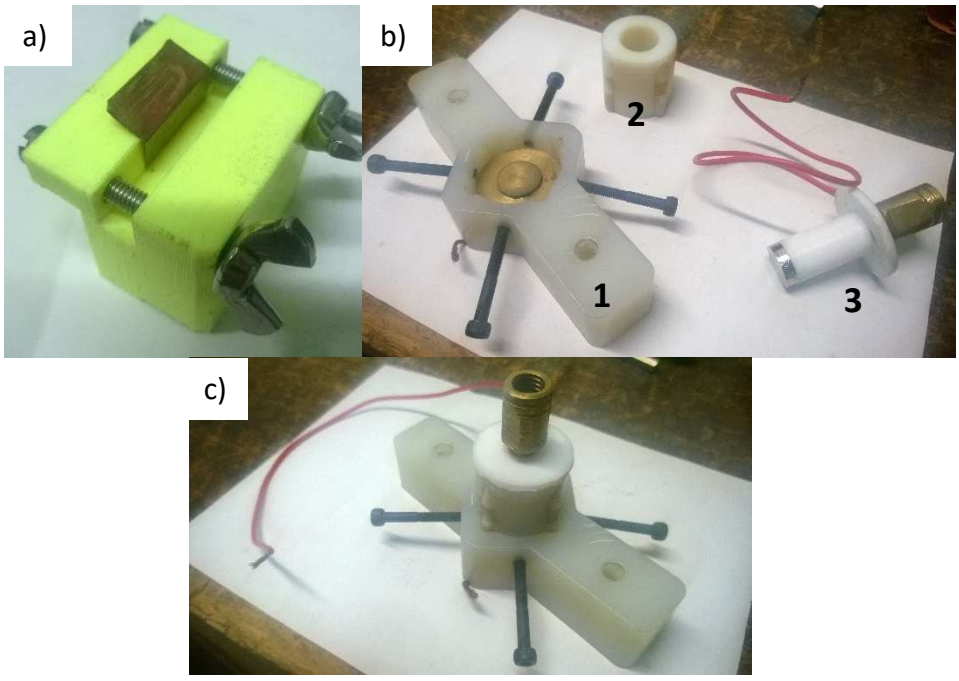

Fig. 3.5 *a) Zoom on a jaw for tension measurements; b) three parts REWOD test cell, disassembled; c) REWOD test cell, assembled.*

electric circuit that allows measuring the energy produced during cycles, for both EAPs and REWOD devices.

In Fig. 3.6b the equivalent electrical circuit of the instrument is shown. Since both REWOD and EAP energy harvesting systems are based on electrostatic phenomena, they need an external polarization source to convert mechanical energy into electrical one. In order to apply a suitable electric field, the measuring instrument was provided with a power supply able to give up to 600V output (BK precision). This is important in particular for EAP systems, that need higher bias voltages (with respect to REWOD) to reach suitable electric fields. In order to measure the energy produced by the system under investigation, the voltage drop across a known resistor (called experimental resistor, R_e) was recorded with the help of a digital oscilloscope (Picoscope 3000 series), connected in parallel to the load. This unity sends the recorded voltage vs. time data to a PC interface (Fig. 3.6c), from which are extracted and mathematically treated to obtain power and energy of the harvesting cycle. Since a leakage current I_L pass through the capacito, represented by the resistor R_L, the measures were taken in AC current regime. I_L was taken into account by measuring it in direct current mode of the oscilloscope, when no mechanical excitation is applied to the electrostatic systems.

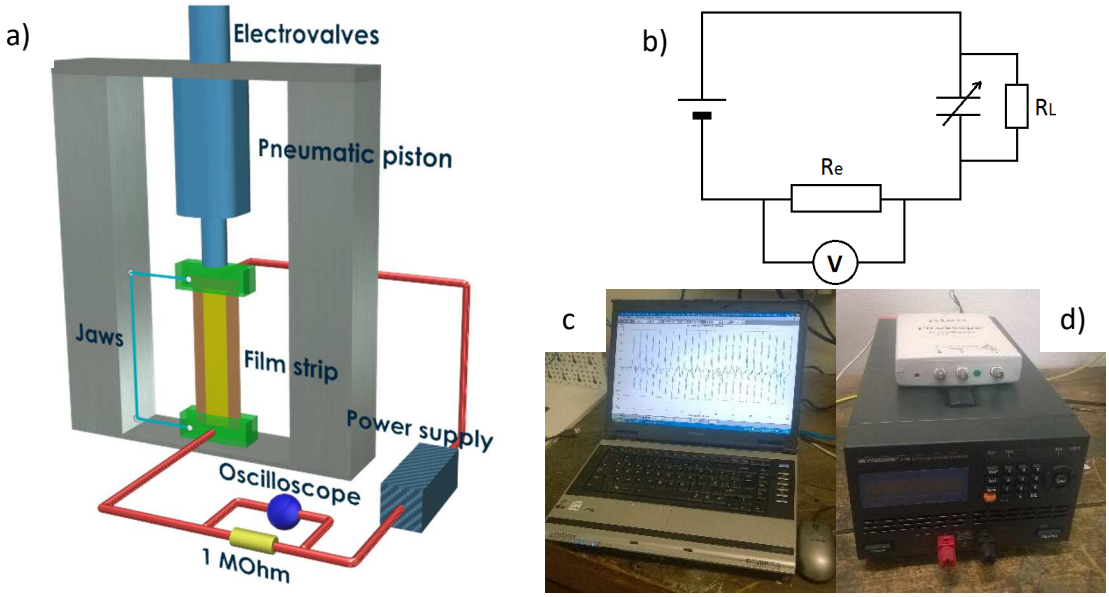

Fig. 3.6 *a) 3D model of the measuring instrument prototype; b) equivalent electric circuit of the measuring instrument. (RL: capacitor resistor; Re: experimental resistor (1MΩ); V: digital oscilloscope); c) PC-oscilloscope interface; d) digital oscilloscope and high-voltage power supply.*

3.4 Energy harvesting measuring instrument: implementation and optimization

During the last part of the project, I focused our efforts on the optimization of the measuring instrument described in subchapter 3.3. In particular, the aspects of safety, precision and accuracy of the test were carefully considered to obtain a reliable instrument that could permit to perform complex electromechanical measurements. Moreover, some implementation have been made to the prototype instrument in order to perform reliable measurements and, on the same test cell, to characterize all the mechanical and electrical properties of the sample under investigation. The first modification of the prototype instrument concerned with the separation of the electrical, pneumatic and measuring units, (*e.g.* pressure, bias voltage, stretching amplitude, etc.) for each sample. In our optimized instrument, we decided to reduce dramatically the hindrance of the

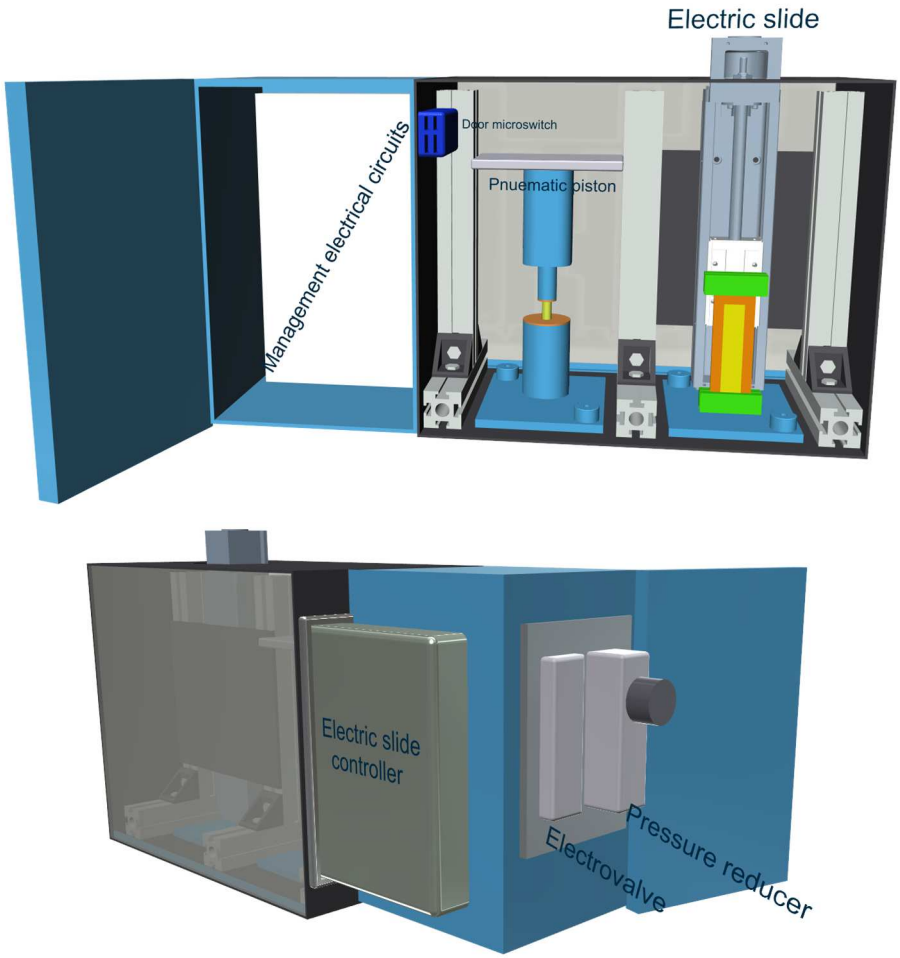

Fig. 3.7 *Front and back visual of 3D-project for the new measuring instrument*

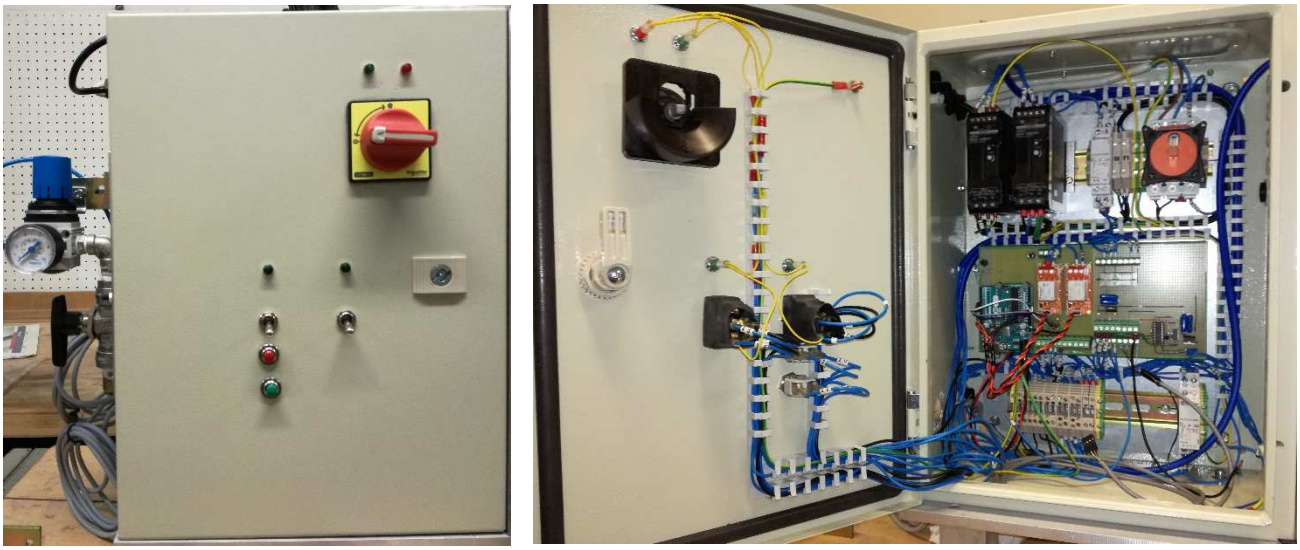

Fig. 3.8 *Open and close visuals of management electric circuit board.*

instrument by integrating all the units of the prototype in a unique compact fashion that occupy only about 0.5m^2 of area, with respect to an entire working table occupied by the prototype (Fig. 3.7). This space reduction was possible by mounting all the units (structure, measuring circuit, piston, etc.) on an aluminum slab (1x0.5m) equipped with anti-vibration supports. All the electrical parts regarding the voltage supply management and safety solutions were confined into an appropriate closed electric board provided with a lock and a general electric switch, that permits to activate and control the instrument actions without the possibility to access directly to the operating electric parts (Fig. 3.8). In particular, on the upper side of the electrical board were placed the power supply for the management electric circuits; in the middle part the Arduino™ board and related circuits that control the pneumatic electrovalve; at the bottom the digital oscilloscope (Picoscope 2000 series), which records force and electric output of the test cells.

Besides modifications directed on reducing the overall sizes of the instrument, also functional modifications have been made. The first we discuss is related to the pneumatic system. First of all, electrovalve and pressure reducer were placed on the side of the electrical board, in order to reduce the instrument hindrance. Moreover, while in the prototype instrument the piston movement was controlled by four electrovalves (2 normally open and 2 normally closed), in the optimized

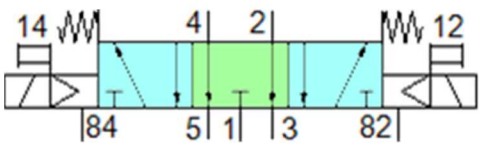

Fig. 3.9 *FESTO electrovalve scheme*

instrument only one electrovalve (FESTO, VUVS-L20-P53E-MD-G18-F7) controlled by the Arduino™ board was employed. In Fig. 3.9 the scheme of the electrovalve employed in the new testing instrument is reported. As can be seen, the electrovalve consists of 3 chambers, with only one working at time. The external chambers (light blue) can be electrically activated, while the central one (green) works in the absence of electrical input. In this way, the piston can be fed in both directions, to perform stress/relax cycles or any other type of action, and when the measure ends, the piston rod can be moved by hand e.g. to replace the specimen.

One of the most important modifications made to the prototype instrument is concerned with the electromechanical excitation part. It regards test cells and actuators that apply electric and mechanical stimuli to the sample under investigation. In fact, in the optimized instrument, an electric actuator (FESTO, egsk) was added to the electromechanical part. Thus, with this addition, this part results as composed of two chambers, one for the pneumatic piston and another for the electric slide (Fig. 3.7). The electric slide was added to the electromechanical part for two main reasons: i) electric actuators can perform actuation profiles different from simple square or sine waves (e.g. simulate the asymmetric walk profile); ii) it is possible to perform two activations at the same time, permitting to explore the coupling between piezoelectric elements (as bias voltage suppliers) and electrostrictive energy generation. As can be seen from the model showed in Fig. 3.7, the electric slide is fixed to an aluminum slab on its backside that, in turn, is fixed to the instrument structure. The slide consists of a mobile element mounted on a leadscrew that is activated by a brushless motor. The mobile element is provided of threaded holes on which an aluminum support is mounted, which houses the test cell.

Another important addition with respect to the first prototype of the instrument consists in the load cell placed under the test cells (Fig. 3.11). As can be seen, the load cell was placed between the lower (fixed) part of the test cell and the basement, in order to record the force transmitted to the sample during testing. The fixing of the test cell was made by a screw, and by a groove on the bottom side of the test cell, that allows it to get stuck with the load cell to avoid the rotation on the fixing screw axis.

In addition, the entire electromechanical part of the optimized instrument was completely closed, by aluminum and PMMA sheets, and provided with a door in its front side. The door, that permits the access of the user to test cells and actuators, is provided with a general electric switch that stops both high-voltage supply to the sample and actuators motion when the user is operating inside the electromechanical chamber (Fig. 3.10).

Fig. 3.10 *Left: door microswitch mounted on the instrument structure; right: door key approaching to the structure microswitch.*

Modifications to the measuring circuit were also carried out passing from the prototype to the final instrument. The nature of the measurement was maintained: the energy generation is measured as a voltage drop on a known resistor by the digital oscilloscope. Since in the prototype instrument safety solutions for electronics against tension peaks were not present, in the final version we decided to protect measuring electronics from tension peaks that could occur (e.g. dielectric breakdown). To do this, an insulating amplifier was added between the film and the oscilloscope (Analog Devices, AD202KN). This additional electronic circuit should guarantee electrical insulation between the connected parts, thus, in our case, protecting the oscilloscope (and electronics connected to it) from tension peaks.

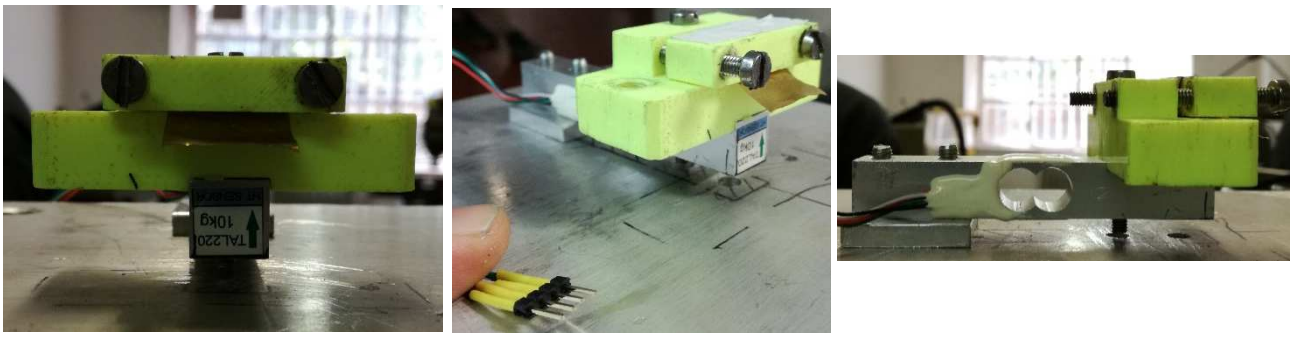

Fig. 3.11 *From left to right: frontal, perspective and lateral visuals of load and test cells mounting on the measuring plate.*

3.5 Chemical and physico-chemical characterization techniques

3.5.1 Scanning Electron Microscopy (SEM)

Scanning electron microscope (SEM) is a type of electron microscope that produces images of a sample by scanning the surface with a focused beam of electrons. This technique is used to analyze small samples, with very high resolution at the same time, where optical microscopy cannot be useful due to diffraction limit (see 3.5.7 section for details).

Depending on the interaction between the impacting electron beam with the sample, different information on sample morphology and composition can be extracted. The possible interactions are: 1. secondary electron emission, the most used emission detected to make SEM photographs; 2. Back scattered electrons, deriving from elastic scattering of beam electrons; 3. X-ray emission, due to ablation of core electrons by the beam; 4. absorbed current and 5. transmitted electrons. Even if all the beam interactions give important information on materials properties, generally 1, 2 and 3 interactions are the most interesting in common SEM analysis. The secondary electron emission permits to obtain topographic information of the surface of the sample, as shown in Fig. 4.19 and 4.20 of section 4.2.1. In secondary electron imaging, the secondary electrons are emitted nearly from the specimen surface. Consequently, SEM can produce high-resolution images of a sample surface, revealing details less than 1 nm in size. Back scattered electrons, or BSE, emerge from deeper locations within the specimen, and consequently the resolution of BSE images is less than SE images. However, since BSE are very sensitive to the atomic number of irradiated atoms, they are often used to analyze the distribution of different elements in a matrix, also deeper in the

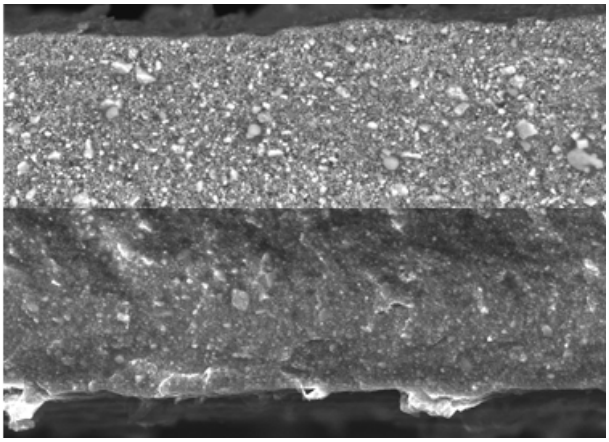

Fig. 3.12 *SEM imaging of a TPU-CCTO sample prepared in our laboratory. Up-side is obtained from BSE, while bottom-side in made from secondary electrons, for the same sample.*

sample with respect to secondary electron emission. This type of emission is particularly useful when analyzing composite materials, like in our case, evidencing the filler included in a matrix (TPU in our case), as showed in Fig. 3.12.

3.5.2 Broadoband Electric Spectroscopy (BES)

Broadband Electric Spectroscopy (BES) measures the dielectric properties of a medium as a function of frequency. This analytical technique is based on the interaction of an external electric field, applied to the specimen by electrodes, with the electric dipole moment of the sample, often expressed by permittivity or conductivity. BES working frequencies varies from 10^{-6} to 10^{12} Hz. In this frequency range many electrochemical properties of the system under study can be obtained. Moreover, depending on the frequency of the response, different relaxation mechanisms can be individuated: *electronic polarization*, due to perturbation of the electronic cloud that surround atoms; *atomic polarization*, due to reorientation of nuclei under the filed; *dipole relaxation*, permanent and induced dipoles oscillates with the field; *ionic relaxation*, comprises ionic conductivity and interfacial space charge relaxation, and *dielectric relaxation*; here listed from high to low frequency of the applied electric field.

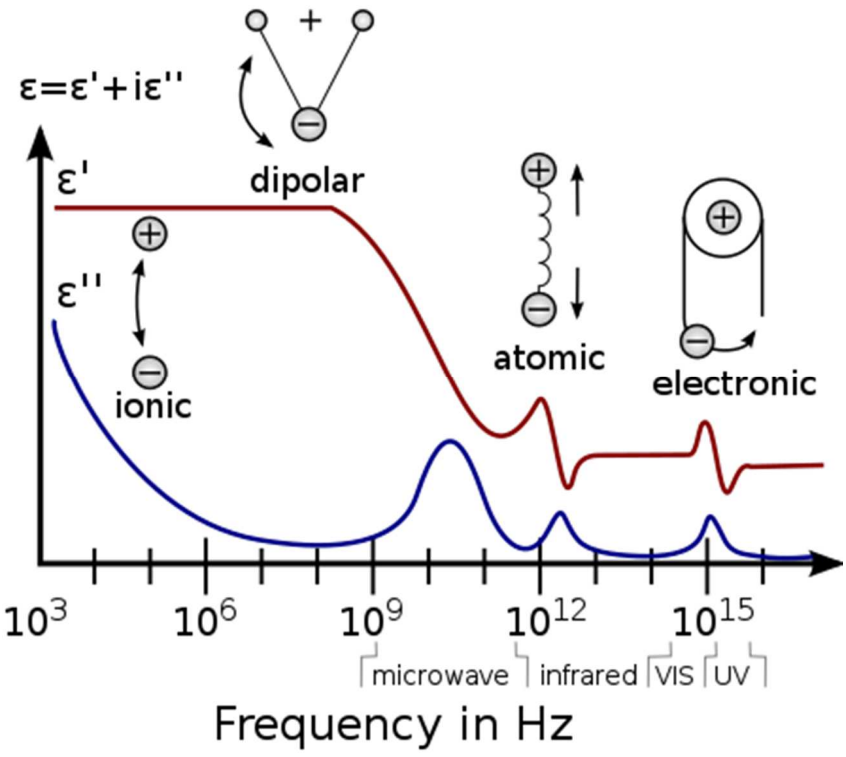

Fig. 3.13 *A dielectric permittivity spectrum over a wide range of frequencies. From the Dielectric spectroscopy page of the research group of Dr. Kenneth A. Mauritz.*

3.5.3 Differential scanning calorimetry (DSC)

Differential scanning calorimetry, abbreviated as DSC, is an analytical technique in which the difference in the amount of heat required to increase the temperature of a sample with respect to a reference is measured as a function of temperature. In a typical DSC experiment the sample and the reference are placed into appropriate holders and placed onto two different heating elements, which supply heat to them, in order to maintain the same temperature during heating/cooling cycles. Once a temperature ramp is set, the heating elements start to heat both reference and sample, but, while the reference material is perfectly stable over all the temperature range, the sample can run in thermal induced processes that lead to absorption or emission of heat. Thermal events try to change the temperature of the sample respect to that of the reference, thus the heating element gives more or less heat to the sample in order to keep the sample/reference temperature equal. The heat flow variation due to thermally-induced processes, is recorded and the final scan is plotted as function of temperature (Fig. 3.14).

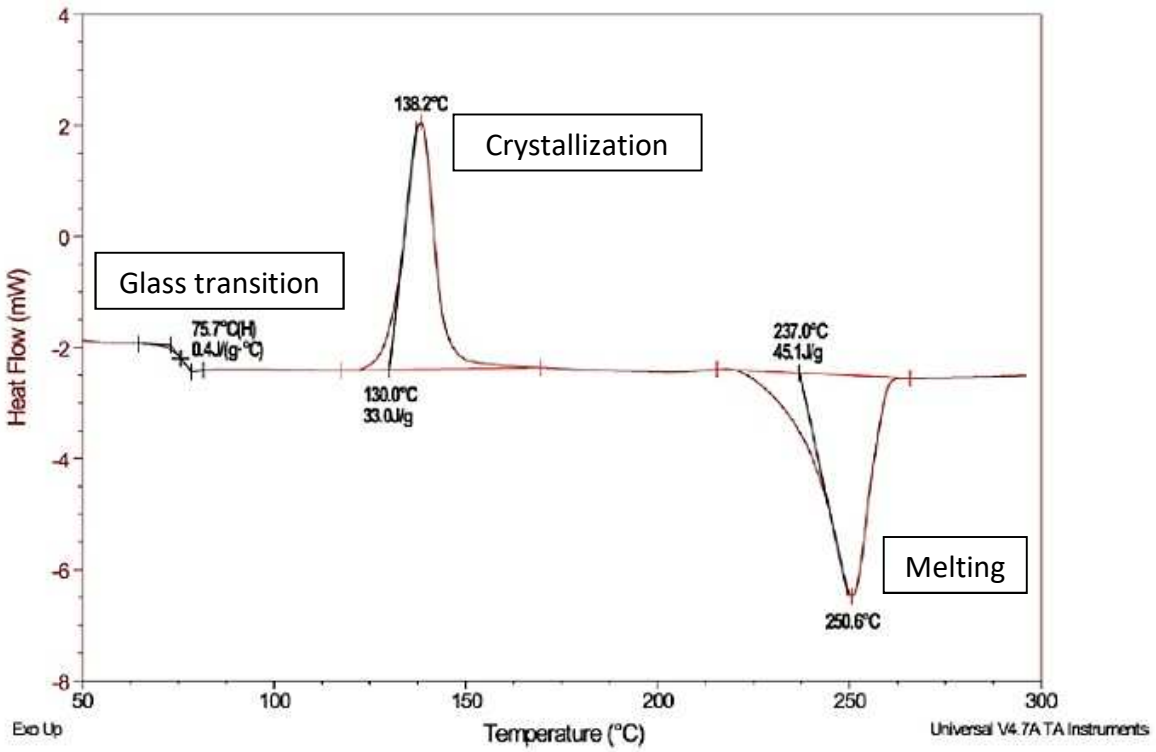

Fig. 3.14 *Explanatory DSC scan of a sample from 50 to 300°C. In the graph are clearly seeable the glass transition (change in heat capacity of the system), crystallization and melting of the sample.*

3.5.4 Ellipsometry

Ellipsometry is an optical technique that measures the change of polarization upon reflection or transmission of light with the sample, and can obtain dielectric/microstructural information of thin films. In particular, ellipsometry is able to obtain accurate information about composition, roughness, thickness (depth), crystalline nature, doping concentration and electrical conductivity of the sample under investigation. The measured signal is the change in polarization as the incident radiation (in a known state) interacts with the material structure of interest (reflected, absorbed, scattered, or transmitted). The polarization change is quantified by the amplitude ratio Ψ and the phase difference Δ. These two parameters are related to the Fresnel reflection coefficients (r_p and r_s) for the sample, according to $\rho = \frac{r_p}{r_s} tan\psi^{i\Delta}$, where r_p and r_s provide information about the optical constants of the sample. Upon the analysis of the change of polarization of light, ellipsometry can yield information about layers that are thinner than the wavelength of the probing light itself, even down to a single atomic layer.

Spectroscopic ellipsometry (SE) measurements were performed with a variable angle spectroscopic ellipsometer (VASE®) from J. A. Woollam Co., Inc. in the 0.3 – 2.5 µm wavelength range with a 10 nm-step and angles of incidence from 60° to 75°. SE data were analyzed using WVASE32® dedicated software which adopts a multilayer model for the samples: this includes the silicon substrate dielectric functions (as derived on a Si reference sample) and the Ta_2O_5 or ZrO_2 film, whose

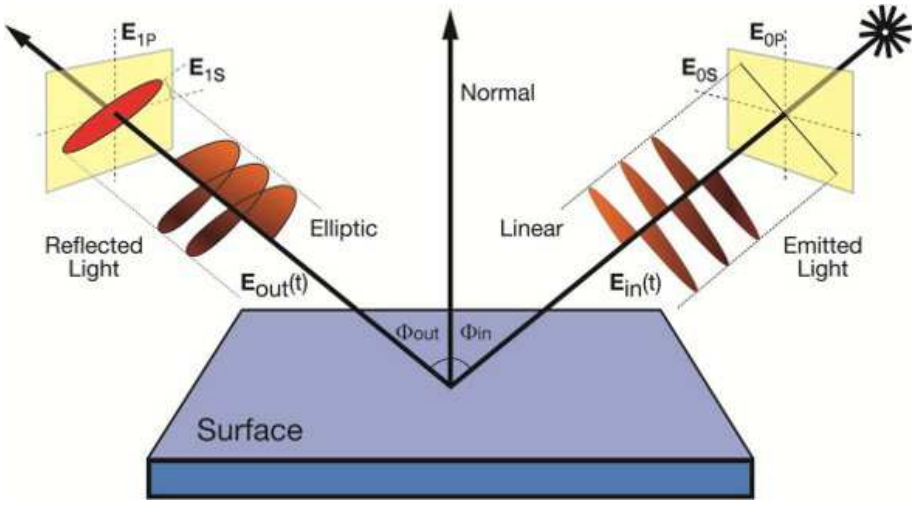

Fig. 3.15 *Schematic of a spectroscopic ellipsometry measurement in which linearly polarized incident light (right) changes to elliptically polarized light (left) after oblique reflection off of the sample.*

dielectric function and thickness were free-parameters of the best-fit procedure. The Teflon overlayer thin film is added on top, with dielectric function and thickness free parameters as well. In particular, the film dielectric functions have been modelled with Tauc-Lorentz oscillators, where the imaginary part at the absorption edge has the typical form for amorphous semiconductors and UV absorbing materials.

3.5.5 Atomic Force Microscopy (AFM)

Atomic force microscopy (AFM), or scanning force microscopy, is a type of scanning probe microscopy. In fact, this technique involves the scanning of a micrometric tip onto the sample in order to obtain an image of its surface. As shown in Fig. 3.16c, the displacement of the tip is controlled by the change in reflection of the laser beam detected by the photodiode.

AFM can also work in three different ways: 1. force measurement, the tip records the force needed to separate itself from the sample surface, performing *force spectroscopy*; 2. Imaging, the displacement of the tip following the surface morphology is used to create an image of the sample and 3. Manipulation, where the tip is used to modify, physically or chemically, the nature of the sample. In order to investigate the morphology of the sample surface, imaging setup is needed. The tip is dragged onto the surface in a x-y grid giving a final 3D image of the surface (Fig. 3.16).

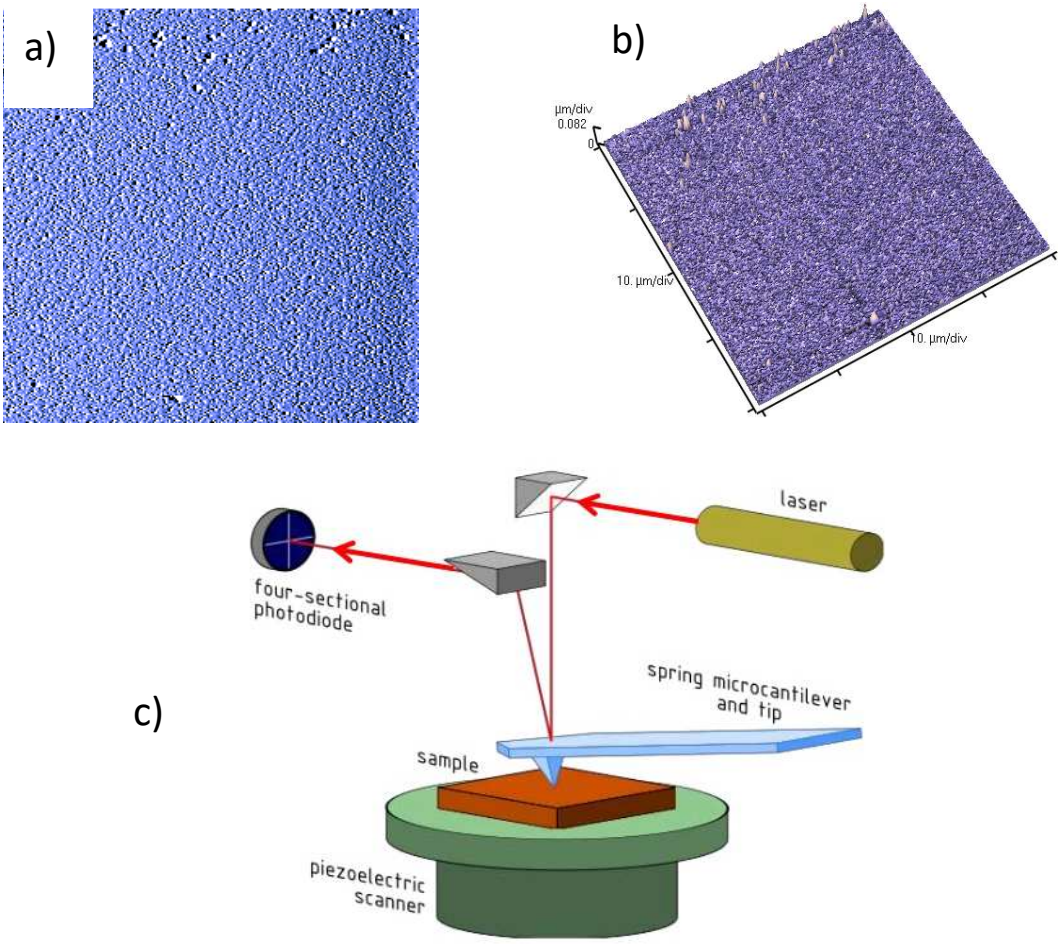

Fig. 3.16 *a) 2D-AFM scan of a PTFE sputtered film; b) 3D view of the sample analyzed in a); c) scheme of the AFM experimental setup: vertical movement of the tip change the angle of reflection.*

3.5.6 X-rays diffraction

X-rays diffraction is an analytical technique used to determine atomic and molecular structure of crystalline materials. This technique is based on the diffraction of X-rays, due to elastic scattering, by the sample. Crystals are regular arrays of atoms, and X-rays can be considered waves of electromagnetic radiation. X-rays can interact with not only the surface atoms, but also with atoms under it. When different X-rays are diffracted at different depths from the sample, they can cancel each other by destructive interaction, or add constructively. The positive interaction between diffracted rays occur only at specific angles of incidence, described by the Bragg's Law:

$$2d \cdot sin\theta = n\lambda \qquad \text{(Eq. 3.2)}$$

where *d* is the interplane distance, θ is the Bragg angle and λ is the X-ray wavelength.

Thus, only at particular Bragg angles diffracted X-rays sum each other, giving a signal that can be detected. What the X-ray diffractometer does is to irradiate the sample with X-rays over a wide range of angles, permitting to individuate all of them where beam diffraction is constructive. Once do this a typical diffraction pattern is obtained, as showed in Fig. 3.18.

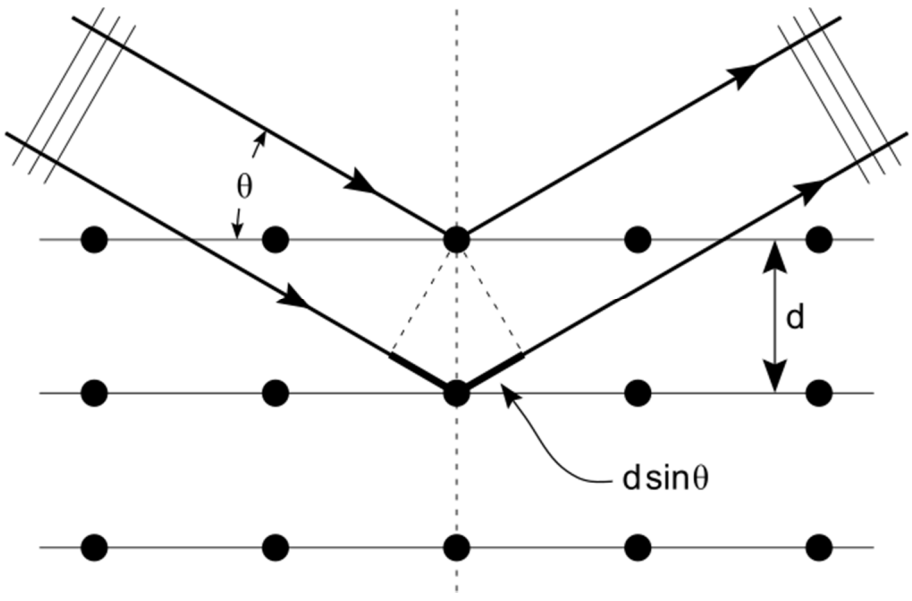

Fig. 3.17 *Graphical display of the Bragg's Law.*

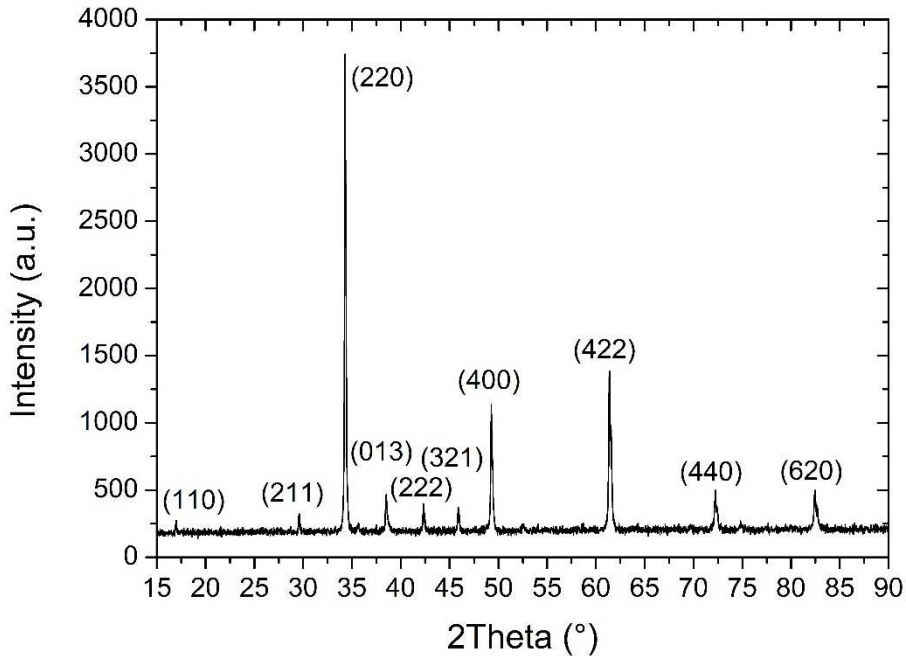

Fig. 3.18 *$CaCu_3Ti_4O_{12}$ diffraction pattern obtained with X-ray diffraction technique. Number between parenthesis indicates the hkl Miller indexes of Bravais lattices.*

3.5.7 Optical microscope

The optical microscope is a type of microscope that uses visible light and a system of lenses to magnify images of small samples. In a sense, what can be obtained from this technique is similar to that obtainable from SEM analysis, but here light is directly used to obtain the sample image. This has the advantage to be quicker than SEM and the sample has not to be electrically conductive, but it reach lower magnification levels due to the diffraction limit:

$$d = \frac{\lambda}{2NA} \qquad \text{(Eq. 3.3)}$$

where d is the resolution, λ is the wavelength of the and NA is the numerical aperture of the objective lens. Considering 550nm as λ, corresponding to green light, and a NA of 1.5 (with oil as medium) the maximum resolution that can be reached is 200nm.

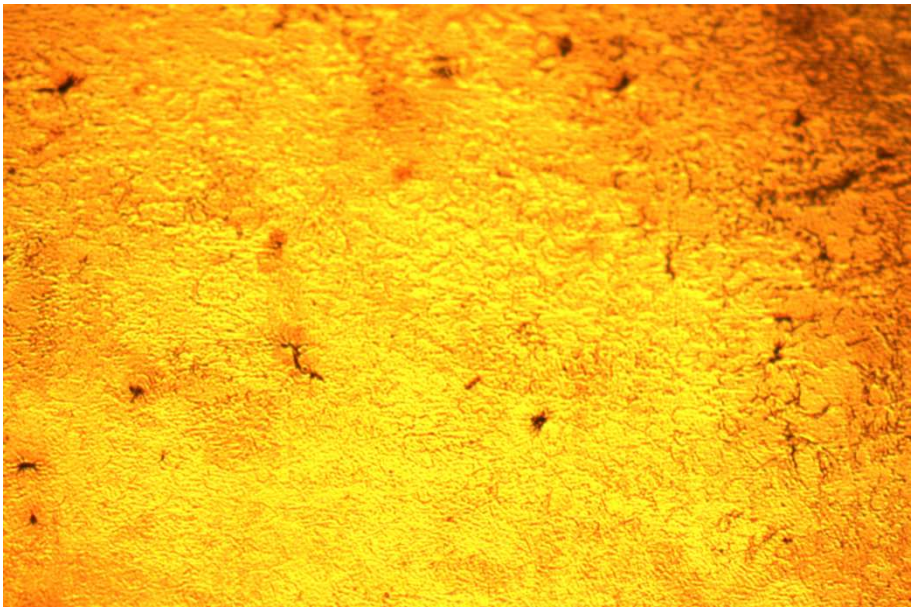

Fig. 3.19 *Gold electrodes imaging we obtained using optical microscope imaging*

3.5.8 Profilometry

Like in the case of AFM, profilometry is a technique used to investigate the surface roughness and morphology by scanning of a micro- or nanometric tip on the sample. The principal differences between profilometry and AFM are the sampling area and the surface data generation. In fact, profilometry can sample and analyze area up to 5µm x 5µm with a vertical resolution similar to that of AFM. Moreover, profilometers do not obtain surface data from optical instrumentation, but they used a very sensitive capacitance method: the end of the tip is directly connected to a plate of a parallel capacitor; its vertical moving changes the distance between the two plates, changing also the capacitance of the capacitor that is converted into height of the sample surface profile.

3.5.9 Tensile testing

Tensile testing, also known as tension testing, is a fundamental materials science test in which a sample is subjected to a controlled tension, for a given displacement or until its failure, and the force exerted by the instrument is recorded. This technique is useful to predict the behavior of materials under dynamic conditions. Once the measurement has been done, strain ($\gamma=\Delta L/L_0$) and stress ($\sigma=F/A$, where A is the section area) can be calculated and used to obtain stress-strain curves (Fig. 3.20). From this useful graphs, much information about materials properties can obtained: Young' modulus, yield strength, maximum elongation, ultimate tensile strength and many others.

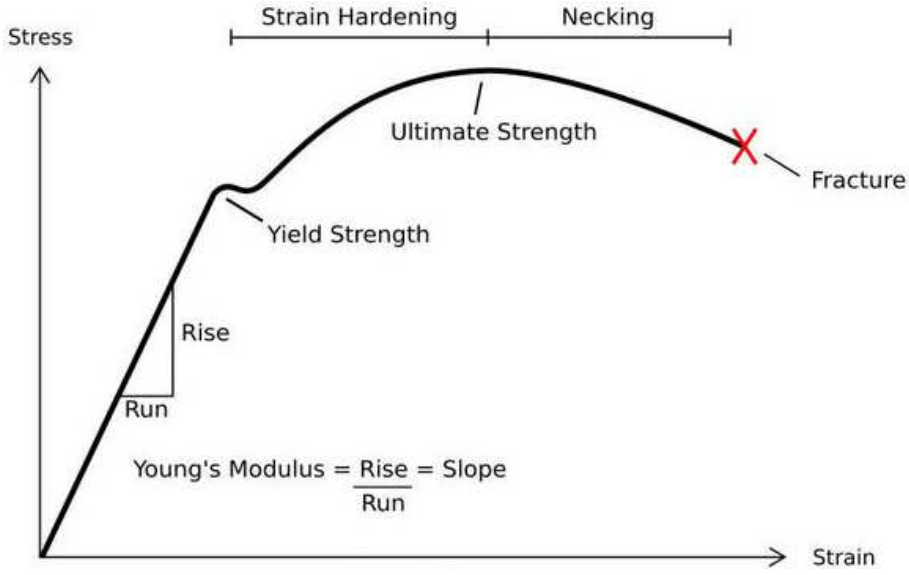

Fig. 3.20 *Example of a common stress-strain curve of a material stretched until its failure.*

4. Results and discussions

As described in the introducing chapters, there exist many ways in order to harvest the kinetic energy from human movement, involving different electrochemical phenomena. However, not all of these are suitable for the conditions that occur when harvesting energy in a shoe, *i.e.* low excitation frequency, that commonly range between 0.5 and 3 Hz, and high amplitude/pressure, in the case of stretchable or static harvesters respectively. Electromagnetic systems can be a good choice due to high generating current density, but when miniaturization is needed different practical aspects, like coil manufacturing and resistance (that increases inversely proportional to the cross section area of the coil) and magnetic field intensity, dramatically compromise the efficiency of devices based on this phenomenon. In the case of piezoelectric systems, two material sub-classes are available: piezoceramics (like PZT) and piezoelectric polymers (PVdF). Piezoceramics tends to be stiff materials and when large stroke mechanical excitations are available, a low mechanical energy transmission is obtained, thus decreasing the efficiency of the process. On the other hand, piezoelectric polymers are softer but suffer from a much lower piezoelectric coefficient compared to piezoelectric ceramic materials, that in turn give lower harvested energy in respect to piezoelectric ceramic bimorphs[42]. From these considerations, our attention was consequently directed on electrostatic systems, in particular on *reverse electrowetting on dielectric* (REWOD) and *electrostrictive polymer composites* (EPCs). The REWOD was chosen due to high power output achievable in all the arrangements (vertical, sliding or microchannel). Moreover, since this phenomenon is a recent discovery and REWOD-based energy harvesters are few, new dielectric materials and deposition techniques can be investigated, to make the device more efficient and easier to fabricate. However, realization of electrically robust thin films (nanometers) of both dielectric oxide and fluoropolymer, and conductive fluid management (Mercury, Hg), makes the fabrication far from trivial.

On the other hand, EPCs-based energy harvesters are small and simple to fabricate, since, ideally, only the active film and the bias voltage supply are needed. These harvesting systems can reach high power densities (up to several mW/cm^3) and the wide range of unexplored polymer/filler combinations is attracting our attention as a possible method to harvest energy embedded in a shoe. In particular, efforts have been directed on increase the dielectric constant by fillers inclusion; maintain the elasticity to achieve high strains and films arrangements (polymer stack) to produce more energy in a compact fashion.

4.1 REWOD materials

As described previously, REWOD devices are composed by a conductive liquid droplet (Hg) placed onto an electrode coated with a dielectric layer. This dielectric layer, in turn, is composed of two sub-layers: a high-k dielectric oxide, deposited directly on the electrode, and a fluoropolymer film, deposited (spin-coated, to date) on the oxide. Krupenkin *et al.*, in their pioneering work, developed an energy harvester system composed of Hg, or Galinstan™ (Gallium-Indium-Tin alloy), dropped on Ta_2O_5/Cytop™ dielectric layer, on quartz[30].

Since Galinstan™ undergoes fast oxidation even in the presence of oxygen traces, the choice of mercury as the conductive drop was mandatory, at least during the experimental stage. In fact, in the case of Galinstan™, the fabrication should be carried out in a glove box and the device itself should be air-tight. So, the use of Hg as the conductive drop was considered for at a first stage, with the intent to replace it later with safer materials.

Krupenkin *et al.* in their work, used tantalum pentoxide as the high-k oxide. In particular, they first deposited via *sputtering* a thin film of metallic Ta (1 µm), and then by anodization they grown a thin layer of the oxide directly on it (200 nm). Our intent during this research project was to evaluate zirconium oxide (ZrO_2) as the dielectric film to replace Ta_2O_5, also with the aim to simplify the oxide layer fabrication. In fact, as evidenced in Table 4.1, that lists the electrical properties of some common inorganic oxides used as insulators in electronic devices, ZrO_2 has both higher dielectric constant, *k*, and insulating properties (*Gap* and *CB offset*). Therefore, zirconium oxide

Table 4.1 *Table of common dielectric oxides properties. Adapted with permission from ref. 43.*

Material	K	Gap (eV)	CB offset (eV)
SiO_2	3.9	9	3.2
Si_3N_4	7	5.3	2.4
Al_2O_3	9	8.8	2.8
Ta_2O_5	**22**	**4.4**	**0.35**
TiO_2	80	3.5	0
ZrO_2	**25**	**5.8**	**1.5**
HfO_2	25	5.8	1.4
La_2O_3	30	6	2.3
Y_2O_3	15	6	2.3

should be able to sustain higher applied electric fields with lower leakage currents with respect to tantalum pentoxide

In this project, to deposit both the Ta_2O_5 and ZrO_2, we used the sputtering process described in detail in the materials and methods section. Depending on the sputtering conditions, it is possible to deposit the oxides directly (from a bulk target or powder), or, via *reactive sputtering* process, from the respective metallic targets with oxygen injection into the sputter chamber.

Commonly, on the top of the dielectric oxides a thin film (few nanometers) of a fluoropolymer has to be deposited in order to prevent charge trapping in the oxide films and promote wetting/dewetting of the conductive drop without contact angle hysteresis. In fact, even at low bias voltages, REWOD films are subjected to huge electric fields, and some charges stored at the electrode/oxide interface can be injected into the dielectric. This means that charges are "trapped" into the dielectric layer and are unable to move back and forth, thus reducing the harvesting efficiency of the device. To date, the most used material to avoid charge trapping and contact angle hysteresis is a fluoropolymer called Cytop™ (Fig. 4.1). It is an amorphous fluoropolymer that can be solubilized in a proper fluorinated solvent and spin-coated on the substrate. However, Cytop™ is very expensive and need to add a procedure step in the fabrication of the device.

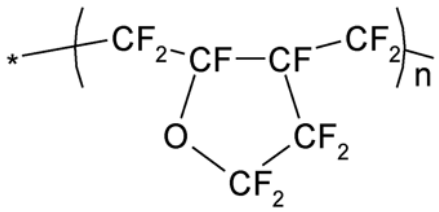

Fig. 4.1 *Cytop molecular structure obtained by radical polymerization*

In this basis, I also focused my efforts to obtain a fluoropolymer coating onto the dielectric oxide without complicate the fabrication of the energy harvester system and, at the same time, to exploit a low-cost material. We chose poly(tetrafluoroethylene) (PTFE) as the fluoropolymer, deposited by RF sputtering. In fact, in literature, deposition of PTFE to obtain super hydrophobic surfaces via sputtering is well known[44, 45, 46]. The choice of this material permits to reduce costs and the number of steps for the device fabrication, that can pass from at three (1. Ta metallic deposition; 2. Ta_2O_5 growth by anodization; 3. Cytop™ spin coating) proposed by Krupenkin *et al.*, to only one (sputtering of the oxide followed by PTFE), simplifying considerably the fabrication process.

Finally, I used doped silicon wafers (Si(100), p-doped, ρ=16-24 Ωcm) as the back electrodes on which to deposit the oxide thin films. It permits to have a very low surface roughness and good electrical contact without depositing a conductive layer under the oxide.

4.1.1 Tantalum pentoxide (Ta_2O_5)

Table 4.2 shows the deposition conditions used to obtain Ta_2O_5 nanometric films by sputtering. In this case, I performed a reactive sputtering deposition from the corresponding Ta metallic target. In fact, oxygen was fluxed into the chamber to react with the Ta atom following the reaction:

$$4\,Ta_{(s)} + 5\,O_{2\,(g)} \rightarrow 2\,Ta_{\,2}O_{5\,(s)}$$

Tantalum pentoxide, at different deposition times, was deposited on Si(100) substrates previously cleaned following a RCA process (detailed description at Chapter 3.1). Briefly, this cleaning process involves 3 steps that permit to consider the substrate completely cleaned from both organic and inorganic impurities, leaving only Si atoms exposed on the surface.

On these substrates, Ta_2O_5 layers of different thickness were deposited, depending on the duration of the deposition. The thickness of the films was obtained by measuring the height of the step between the substrate (masked during the deposition) and the deposited film, by means of profilometry, or by ellipsometry measurements.

Table 4.2 *Sputtering deposition conditions for Ta_2O_5 dielectric layer. High temperature of deposition are useful to obtain better adhesion and morphology of the dielectric layer.*

Ta_2O_5	
Target	Ta metallic target (99.95%)
Temperature [°C]	600
Pressure [mbar]	$1.4 \cdot 10^{-2}$
Power density [W/cm^2]	5.5
Deposition time [h]	0.5, 2, 4, 6
Ar flux [sccm]	20
O_2 flux [sccm]	3.5

Table 4.3 *Deposition times and thicknesses of tantalum pentoxide deposited on cleaned Si(100) substrates.*

Deposition time [h]	Thickness [nm]
0.5	520
2	735
4	1463
6	2258

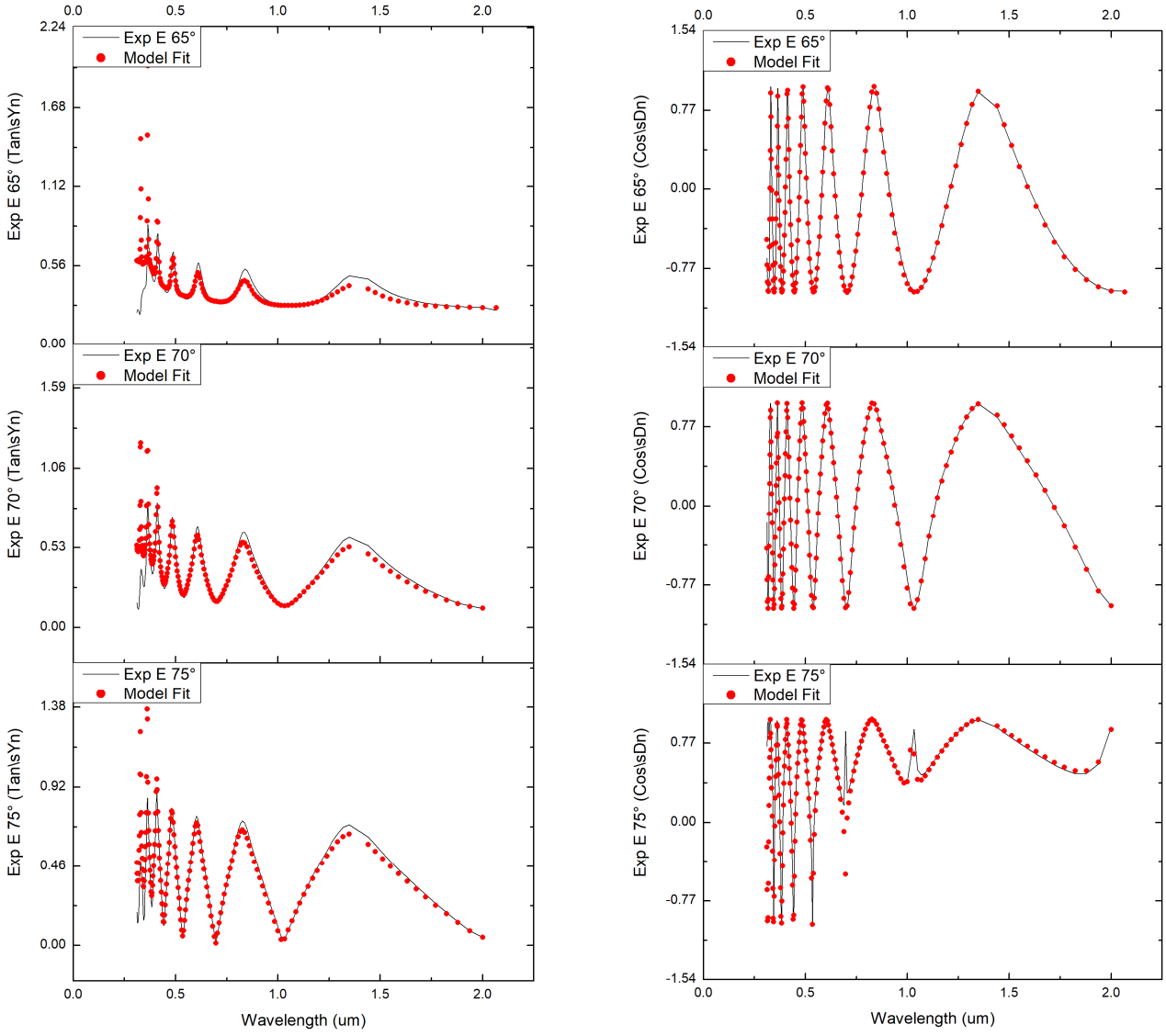

Fig. 4.2 *Tanψ and CosΔ of 500nm thick Ta2O5 sputtered film.*

Fig. 4.2 shows the ellipsometry outputs obtained for a 500nm thick Ta_2O_5 film sputtered on silicon. Since the output curves (ψ and Δ) are not directly related to the optical properties of the film under investigation, they have to be fitted to obtain the parameters related to the sample analyzed. On the other hand, these graphs are useful to verify the fitting quality obtainable for the sample under investigation, thus the reliability of the parameters measured with this technique. In the graphs reported, the outputs obtained by irradiating the sputtered film at three different angles of incidence of the light beam at 65, 70 and 75 degrees, are showed. As can be observed, the fitting curves (red dots) fit well with the experimental outputs (black lines) for Δ, while for ψ there is a little difference between the fit and the experimental curves at the top of peaks, but it still be considered a good fitting. The values obtained by the two techniques were comparable and are listed in Table 4.3. As can be noted from Table 4.3, the growth of Ta_2O_5 on Si(100) is rapid during the first 2 hours of deposition, then it stabilizes and continue with a linear trend for higher deposition times. From these values we obtained an average deposition rate of 343 nm/h.

Further, the structure of deposited Ta_2O_5 was investigated by X-ray diffraction analysis (XRD). The crystalline nature of thermal treated Ta_2O_5 films was investigated, since is reported that crystalline Ta_2O_5 have better ε[47]. Fig. 4.3 reports the X-ray patterns recorded for annealed Ta_2O_5 films, while the as deposited films are amorphous. Here, is evident that Ta_2O_5 films are amorphous until 600°C and from 700°C crystallize in the β-Ta_2O_5 orthorhombic phase. Can be noted also that the relative intensity of the peaks at 22.81, 28.24 and 37.12 (corresponding to (001), (200) and (201) respectively) changes when thermal treatment pass from 700° to 800°C. This change in intensity, but not in the diffraction angle, means that no structural changes occur in the material, but that probably preferential orientation took place in the 800°C treated films. X-ray diffraction pattern of 700°C thermally treated film was used to obtain the cell parameters of sputtered films and to be compared with that reported in literature. XRD pattern was thus subjected to profile matching analysis. We obtained that our sputtered films has an orthorhombic Pccm structure with lattice constants of a= 6.220(1) b = 3.617(6) c = 7.757(1) (numbers between parenthesis refer to the error on the third decimal number), with an according parameter χ^2=2.25. These values are in good agreement with those reported in literature[48].

Fig. 4.4 shows the AFM scans obtained for Ta_2O_5 films sputtered for different deposition times. For a better view of the sample surface, we analyze the sample over a square area of 60 µm of side.

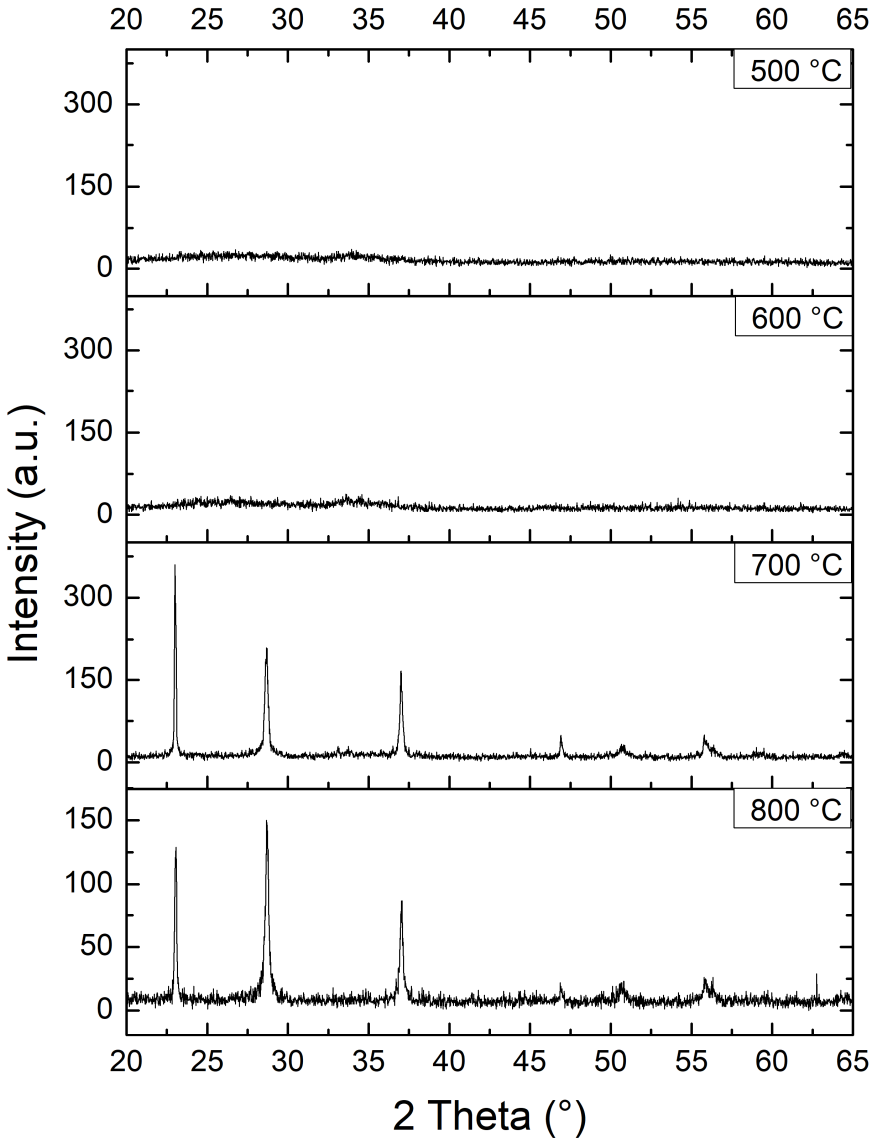

Fig. 4.3 *XRD patterns of annealed Ta_2O_5 rf. sputtered films on Si(100) as the substrate.*

As can be noted from AFM scans, increasing the duration of the deposition (thus the thickness of the film) the roughness value decrease. In fact, the roughness passes from 10nm for thinner films to 7nm for thicker ones. Considering the scans showed in Fig. 4.4, it can be noted that at higher depositions times the films surface presents imperfections like grains that become bigger as the film thickness increases. In contrast, the ground surface present a lower roughness that makes the average roughness of the entire sampled area lower. A general consideration that can be made on this films, is that thinner films present a more regular surface and a less quantity of defects with respect to thicker films. This is a good result for this application where lower film thicknesses lead to higher induced electric fields, at the same bias voltage. The surface of sputtered Ta_2O_5 films was

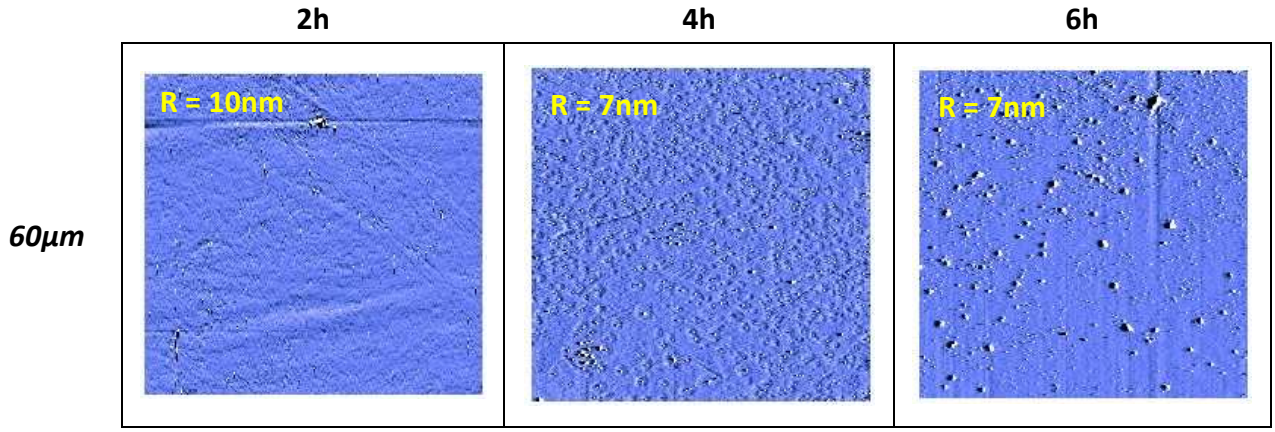

Fig. 4.5 AFM scans of sputtered Ta2O5 films on Si(100) substrates at different deposition times.

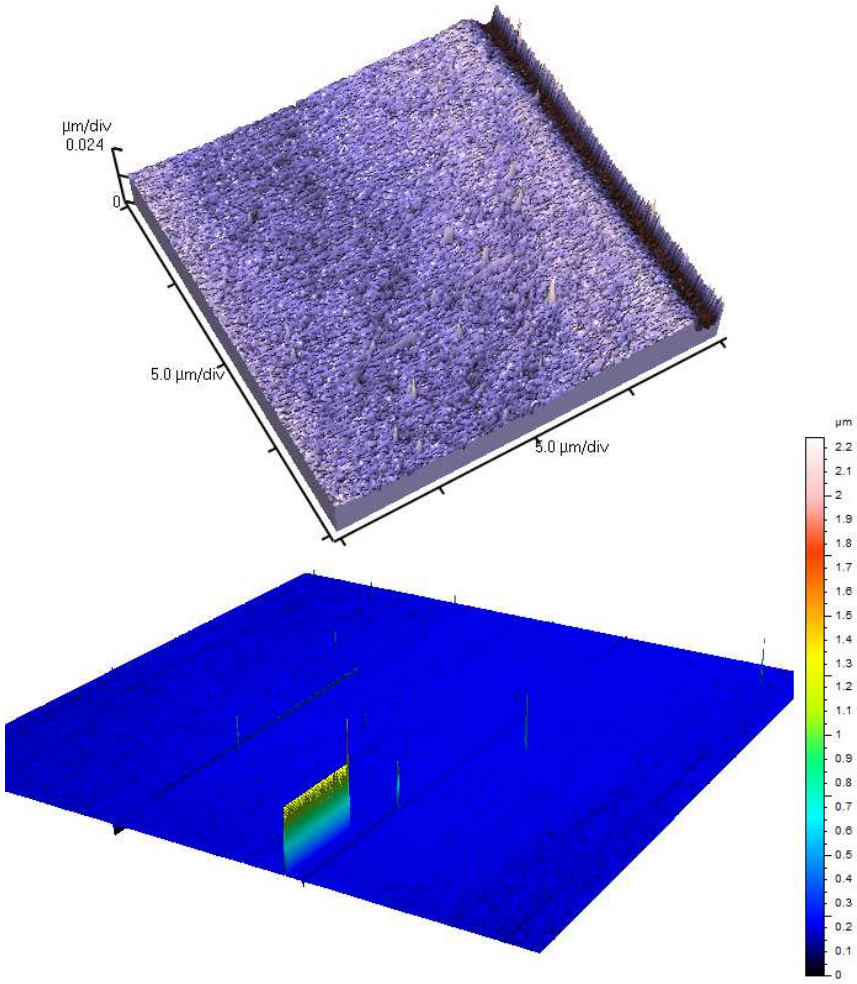

Fig. 4.4 AFM (40x40µm area) and profilometer (500x500µm area) 3D surface analysis of Ta_2O_5 film deposited on Si(100) substrate.

also analyzed by profilometry analysis. This technique, similar to AFM (see differences in sub-Chapter 3.5.8), scans the surface thank to a micrometric tip and measure its morphology. The main difference between profilometer and AFM analysis is the sample area that can be analyzed at the

same time: while for AFM a 60x60µm area can be considered as standard, for profilometer areas of 500x500µm or more can be analyzed in a routine study. Obviously, the time needed to analyze such big areas is much higher than that needed by AFM, but this technique permits to investigate the morphology of larger surface giving more information about it. In Fig. 4.5 it is reported a 500x500µm area analyzed by profilometry, and a 3D image of the 2h AFM scan. As can be noted, in the lower part of the profilometer surface a relatively tall and narrow defect is present, that can be ascribed to impurities (like dust particles) that were present on the substrate before the deposition, or by a rebound of the tip after met a grain on the surface. By further investigation on the sample we found that such type of defect is absent in other parts of the film, thus permitting to be considered as an isolated defect. Finally, profilometer analysis shows a surface that can be considered smooth, but also shows the presence of some small grains that reaches heights up to hundreds of nanometers.

4.1.2 Zirconium dioxide (ZrO_2)

Zirconium dioxide films were obtained by the sputtering technique. With respect to tantalum pentoxide, some differences exists in the deposition conditions of ZrO_2. The first consists in the target nature: while in Ta_2O_5 it was a bulk Ta metallic, that under reactive conditions was deposited as the corresponding oxide, here the target material was directly the oxide, in the form of powder (SIGMA-ALDRICH, *Zirconium(IV) oxide*, 204994). Table 4.4 summarized the experimental conditions used to deposit ZrO_2 thin films. As it can be noted, even if the deposition is not *reactive*, also in this

Table 4.4 *Sputtering conditions used for ZrO2 deposition*

ZrO_2	
Target	Powder (99%)
Temperature [°C]	rt.
Pressure [mbar]	$9 \cdot 10^{-3}$
Power density [W/cm²]	2.5
Deposition time [h]	4, 6, 8
Ar flux [sccm]	10
O_2 flux [sccm]	1.5

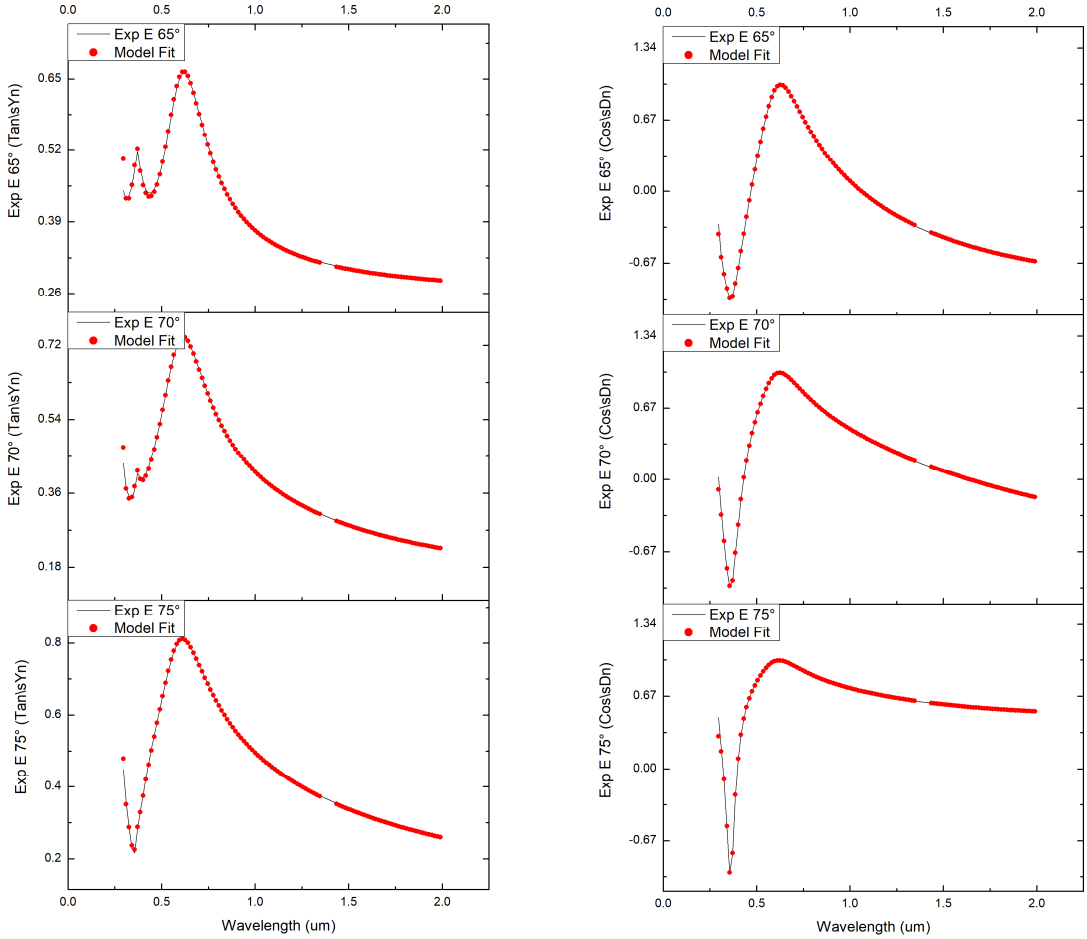

Fig. 4.6 *Ellipsometry output of a 60nm thick ZrO2 sputtered film*

Table 4.5 Sputtering deposition times and relative measured thicknesses

Deposition time [h]	Thickness [nm]
4	65
6	122
8	133

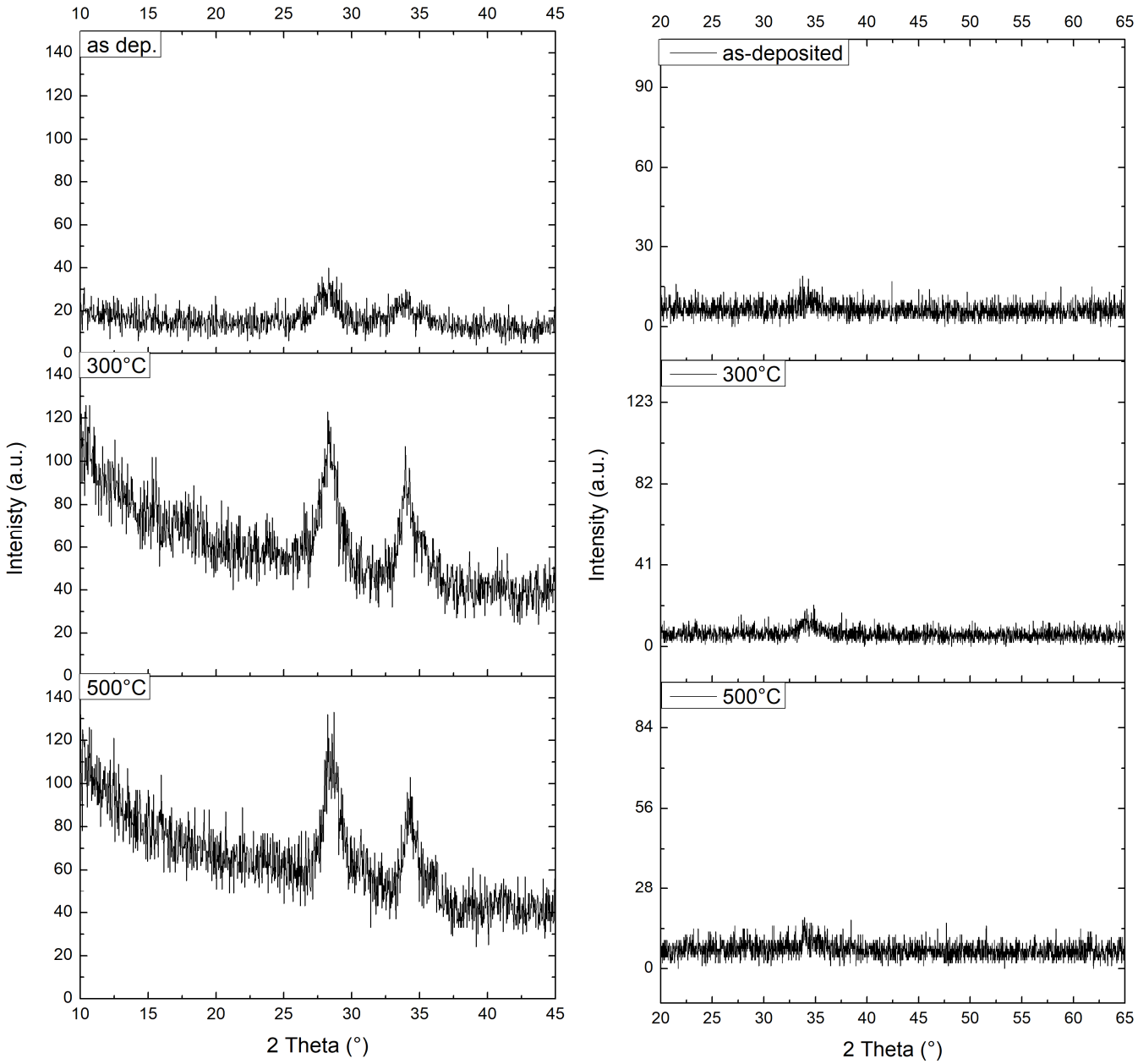

Fig. 4.7 Bragg-Brentano (right) and grazing incidence (left) X-ay diffraction patterns of 60nm thick ZrO2 film deposited on Si(100), as deposited and after thermal treatment.

case oxygen flux was injected into the sputtering chamber during deposition. This was done to ensure the deposition of stoichiometric ZrO_2 films. In fact, only argon flux could lead to sub-

stoichiometric samples. Another important difference is related to the deposition duration of ZrO_2. In fact, due to differences discussed before, the deposition of nanometric ZrO_2 films took more time with respect to Ta_2O_5 films. As in the case of Ta_2O_5 films, also the thickness of ZrO_2 sputtered films were measured by profilometry and by ellipsometry measurements. The values obtained by these two techniques were comparable, and the average values were reported in Table 4.5. From the data listed in the table, it can be noted that ZrO_2 deposition rate is much lower (18nm/h) than that of Ta_2O_5. Fig. 4.6 reported the outputs (ψ and Δ) of ellipsometry recorded for an as-deposited 60nm thick ZrO_2 film sputtered on Si(100) at three different angles of the incident beam. At a first sight, we observe a much lower number of fringes with respect to the output of Ta_2O_5. This is due to the lower thickness of ZrO_2 films. Another consideration regards the quality of the fits of the output signals. As can be seen, fitting curves (red dots) matches well the experimental ones for all the angles and for both ψ and Δ (black lines), permitting us to consider thickness values obtained from ellipsometry as reliable.

The crystalline structure of sputtered films of ZrO_2 was then analyzed by X-ray diffraction technique. Unfortunately, due to very low thickness of the films under normal Bragg-Brentano configuration of the X-ray measurement was not possible to clearly understand if the film were completely amorphous or if they contained crystalline parts. In fact, as showed in Fig. 4.7-right, the

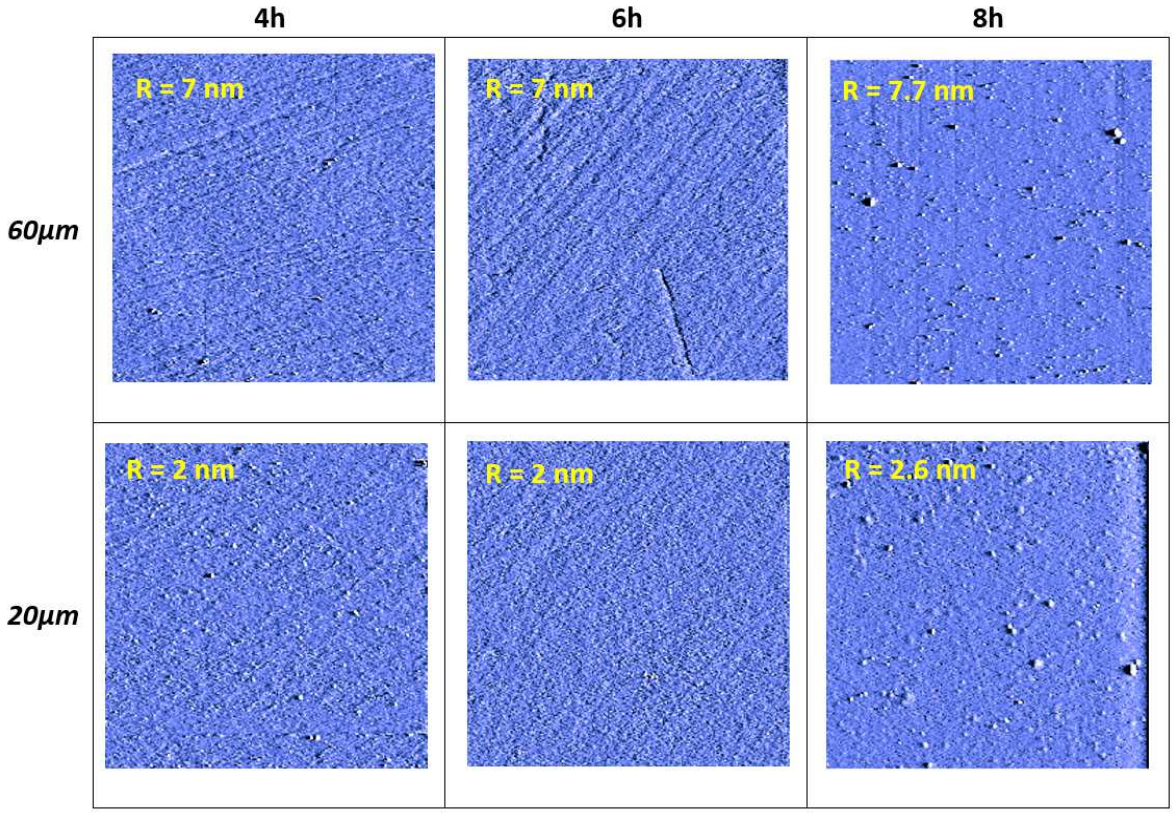

Fig. 4.8 *2D AFM scans of sputtered ZrO2 film on Si(100) substrates at different deposition times and for different sampling areas.*

diffraction patterns are similar for all the samples investigated, displaying a little signal at about 30-35°, that can be due to crystalline domains but it is still not enough resolved to allow to determine the crystalline structure. In order to verify the presence of crystalline domains inside the sputtered ZrO_2 films, a grazing incidence diffraction configuration of the X-ray measurement was used. It consists in keeping the position of the emitter constant during all the measure at small angles, while the detector position is varied over the angle range of interest. This permits to the incident beam to interact with a higher amount of deposited material during all the measure, but needs much more time for each step to record a signal. The X-ray patterns recorded by using this technique are reported in Fig. 4.7-left. As can be seen from these graphs, the peaks present in the x-ray patterns are well resolved for all the samples. Moreover, they are higher in intensity permitting to note that, even in as-deposited samples, there is a crystalline portion in the sputtered films, corresponding to the typical monoclinic structure of ZrO_2 at room temperature. This structure is maintained and

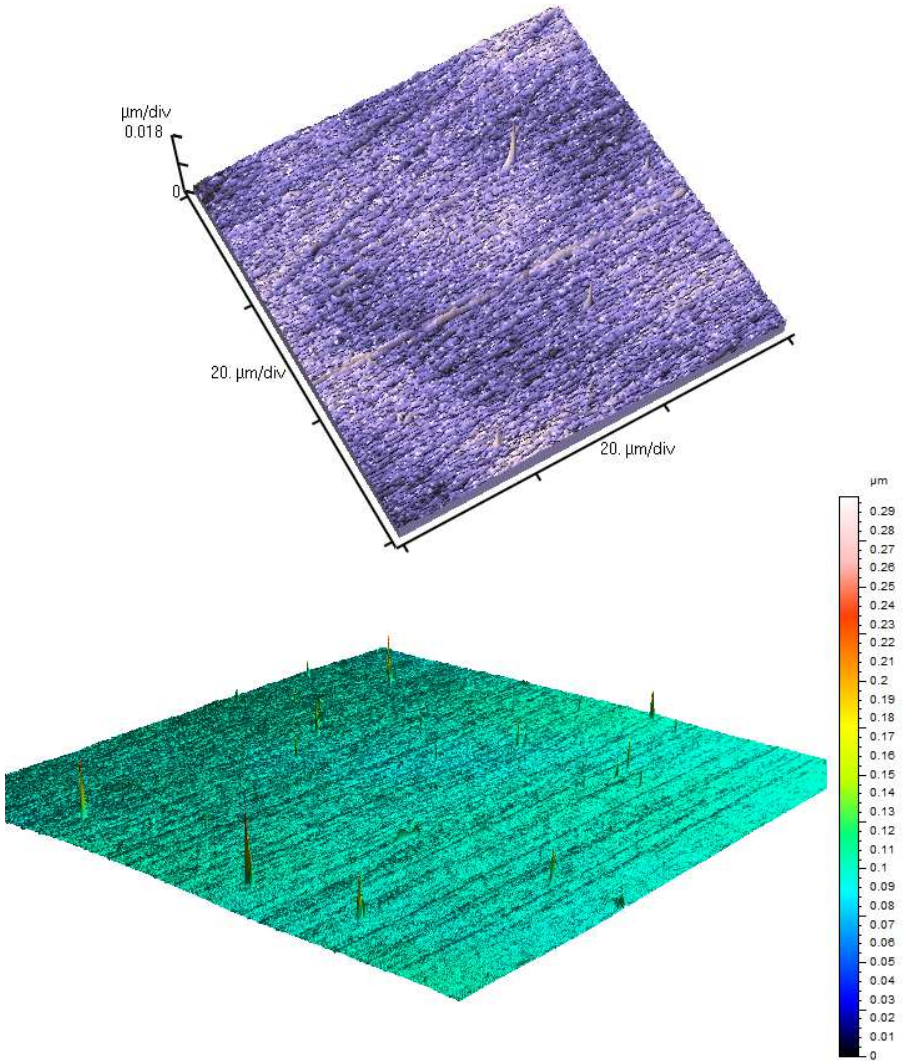

Fig. 4.9 *AFM (Upper, 40x40µm area) and profilometer (Down, 500x500µm area) 3D scans of a 60nm thick sputtered ZrO_2 film on Si(100) substrate.*

consolidated in all the thermally treated samples, as shown by the X-ray diffraction patterns of 300°C and 500°C specimens.

Finally, the surface morphology of the sputtered samples was analyzed by AFM and profilometry techniques. In particular, 2D-AFM analysis, as in the case of Ta_2O_5 deposition, was employed to determine the surface roughness (Fig. 4.8). For this material, two dimensions of the sampled area were considered to obtain the average roughness of the sputtered films. As it occur for Ta_2O_5, also for ZrO_2 film deposition the roughness increases with deposition time, or thickness of the film. This trend is confirmed for both the areas, 20 and 60µm squares. Moreover, some scratches were recorded on some samples, like that showed in Fig. 4.8 - 4h/60µm. They can be ascribed to the Si(100) substrate damages got during the mounting on the mask of the sputtering system or during manipulation.

Another consideration about the surface morphology regards the grains defects present on the sputtered films. While for 4 and 6 hours deposition times few defects were found on the surface, for the 8 hours films a discrete number of defects was detected for both the areas. This trend is the same observed for tantalum pentoxide films, and is related to the sputtering deposition technique. In fact, at higher thicknesses of the film, a local preferential growth of the some film sites on the surface can occur, leading to the formation of grains on the surface.

This is confirmed by 3D-AFM and profilometry analysis showed in Fig. 4.9. Here, the presence of a little amount of grains on the films surfaces can be clearly noted, but, beside them, the ground of the film remains smooth and the roughness is quite constant. Moreover, looking at the bigger profilometer area, the film shows a homogeneous surface without important defects detected on it. This is a good achievement for REWOD application because defects, or thickness variations of the film, can lead to dielectric breakdown, in particular for thin ZrO_2 sputtered films.

4.1.3 PTFE Coating

Krupenkin *et al.* demonstrated that, for REWOD devices, the presence of a fluorinated coating on the dielectric oxide thin layer might improve the performances of such devices. In particular, they found that organic fluoropolymer coating have best performances in terms of avoiding contact angle hysteresis of the conductive drop and to reducing charge trapping in the dielectric oxide, with respect to inorganic fluorinated coatings, when high electric field are applied.

Table 4.6 Experimental conditions investigated for PTFE sputtering deposition.

Polytetrafluoroethylene (PTFE)			
Target	Bulk PTFE disc		
Power density [W/cm^2]	1.25	2.5	3.75
Pressure [mbar]	$5 \cdot 10^{-2}$		
Deposition time [min]	30 ÷ 5		
Ar flow [sccm]	20		
Distance [cm]	5 ÷ 10		

During my investigation on these systems, I performed sputtering deposition of polytetrafluoroethylene (PTFE) to obtain a hydrophobic and low-friction coating on both Ta_2O_5 and ZrO_2 sputtered films. It should permit to obtain a REWOD preparation process involving only one deposition technique in a two-stage fabrication (oxide and PTFE depositions).

Even if in literature different works on PTFE sputtering are reported[44, 45], the deposition of fluoropolymer coatings by this technique is not trivial due to its high sensitivity to the experimental conditions. In fact, to obtain a good and reliable PTFE coating, a deep study on conditions optimization was mandatory. Table 4.6 lists the experimental conditions investigated during this project. As can be noted, I fixed some experimental conditions, extracted from the literature, in order to simplify the optimization of the deposition. For example, I kept fixed the nature of the target, that was a disk of bulk PTFE, the sputtering chamber pressure during deposition at $5 \cdot 10^{-2}$mbar and the argon flow. In particular, it was important to maintain fixed the chamber pressure, because the sputtering process was very sensitive to it. In fact, in this case, even small variations of this parameter lead to inefficient and/or not reproducible depositions with also the risk to damage the electronics of the instrument. Accordingly, deposition time, target/substrate distance and power density were varied in order to understand how they could affect the deposition rate and morphology of PTFE films. However, in order to address the role of experimental conditions on the PTFE films thickness and morphology, before to deposit it onto the dielectric oxides, it was deposited on virgin Si(100).

Since REWOD devices are covered with a very thin layer of fluoropolymer of about 12nm, during our study on PTFE deposition we want to individuate the experimental conditions that permit us to obtain comparable film thicknesses. In Fig. 4.10 the thickness values obtained by varying the target/substrate distance and the power are reported. As can be expected, a power decrease and

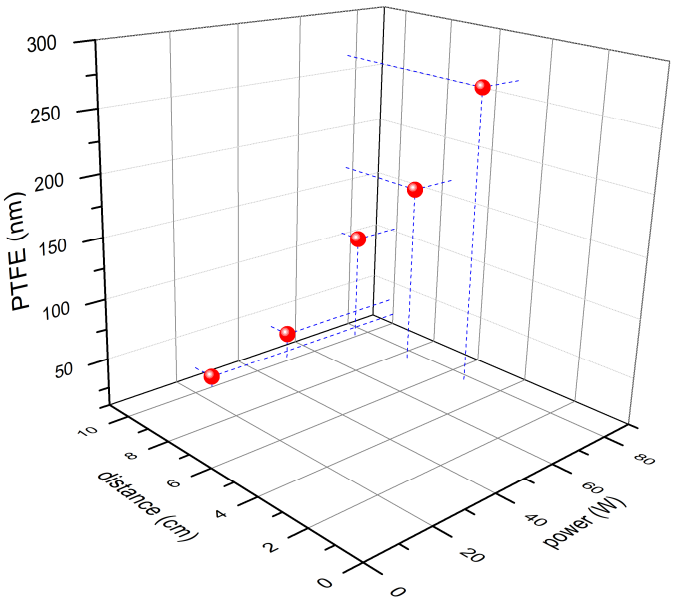

Fig. 4.10 *PTFE sputtered thickness as function of target/substrate distance and deposition power (t=25min; substrate=Si(100))*

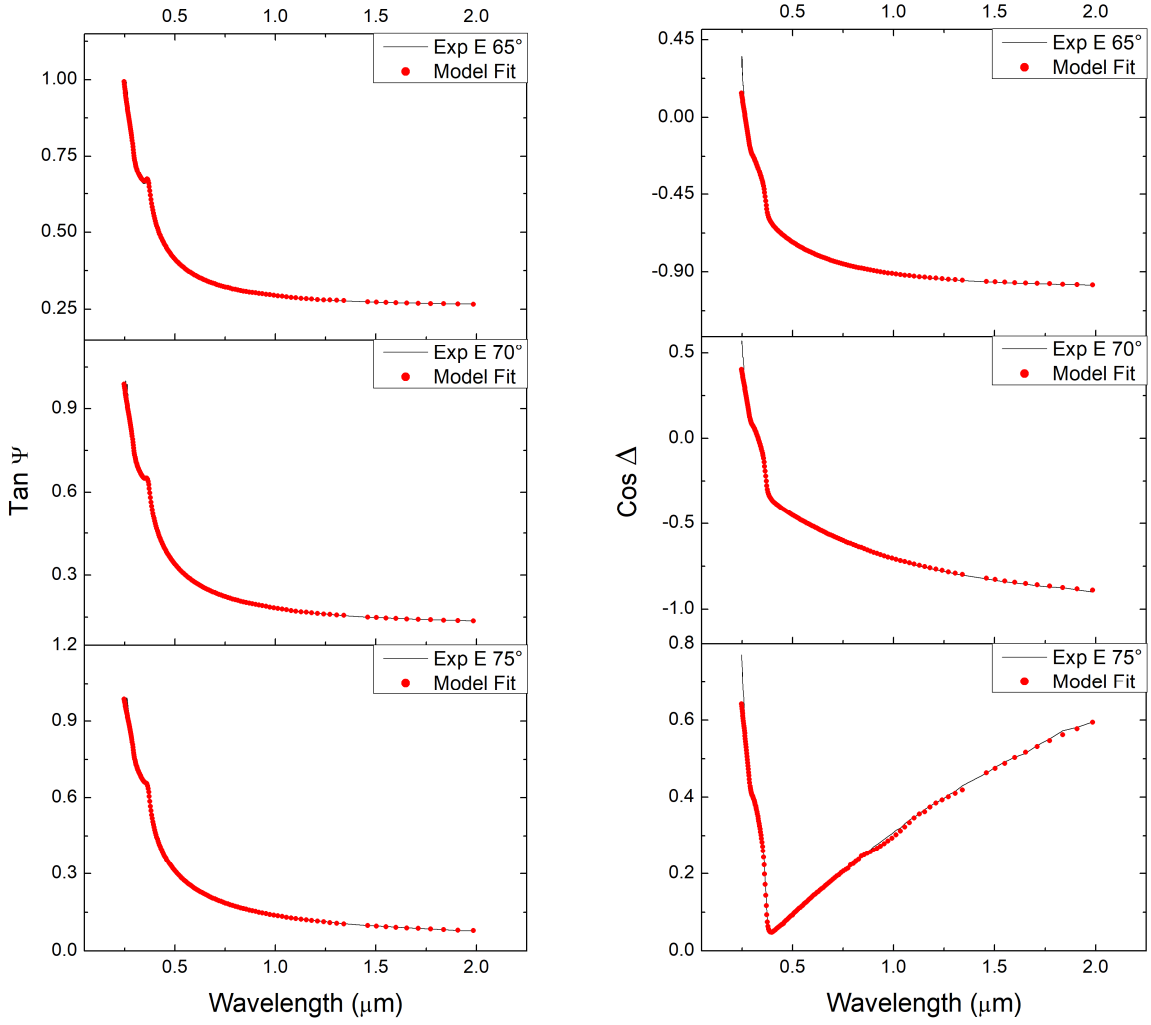

Fig. 4.11 *Ellipsometry output and fitting curves of 19nm thick PTFE sputtered film on Si(100) at different incident angles*

an increase in target/substrate distance leaded to thinner films, passing from 263nm obtained at 75W (3.75W/cm^2) - 5cm to 19.4nm at 25W (1.75W/cm^2) - 10cm. In particular, this last value can be considered as a good achievement because it is comparable with that obtained by Krupenkin *et al.* by spin-coating of Cytop^{TM}.

As in the case of ZrO_2 and Ta_2O_5, the thickness of the sputtered PTFE films was determined by ellipsometric measurements. Fig. 4.11 shows the experimental and fitting curves obtained for the 19.4nm sputtered film. Also in this case, the fitting curves match well with the experimental ones permitting to extract to film parameters. Even if not displayed, the model curves fit well, at all the angles, the experimental curves for all the samples prepared. Therefore, all the thickness data were considered as reliable.

Further, since the final application includes contact between fluoropolymer and conductive drop, the morphology of the film obtained was investigated by AFM and profilometry analysis. The results of these two techniques are reported in Fig. 4.12a. All the scans refer to the 19nm films, obtained under the experimental conditions discussed above. In the 2D scan the surface relative to scanning a 40x40µm square area is reported. As it can be noted, many grains are present on the surface, indicating that the film is not completely smooth. This is confirmed also by 3D-AFM that shows many grains on the surface. In fact, the RMS roughness of the sampled area resulted of 7nm, that is one third of the film thickness, indicating that the film growth on Si(100) is not homogeneous and grain defects are spreaded on the whole surface. On the other hand, when considering thicker film surfaces, of more than 100nm, the film morphology is quite different (Fig. 4.12b). In fact, here the surface roughness (1.1nm) is considerably lower than that of thinner films. Moreover, looking at 2D scan of the surface, little cracks and ripples are present on thinner PTFE films, indicating that, beside the higher roughness due to defects, some kind of strain occurs leading to cracks formation. This doesn't happen for thicker films where the next growth of PTFE defects generate again an irregular surface, as it can be seen from 2D scan in Fig. 4.12b.

Once having individuated the experimental conditions to obtain film thicknesses comparable to that of Krupenkin *et al.* by spin coating Cytop^{TM}, the following step of the project involved the deposition of PTFE films directly on ZrO_2 and Ta_2O_5 dielectric oxides. Due to changing of the substrate for PTFE growing, the chemistry of the surface and the nature/strength of the PTFE/substrate interaction changes considerably and thus an investigation on deposition conditions was conducted again. The first difference to be accounted for was how the substrate material affects the final film morphology and thickness during sputtering deposition. To do this, I replicated

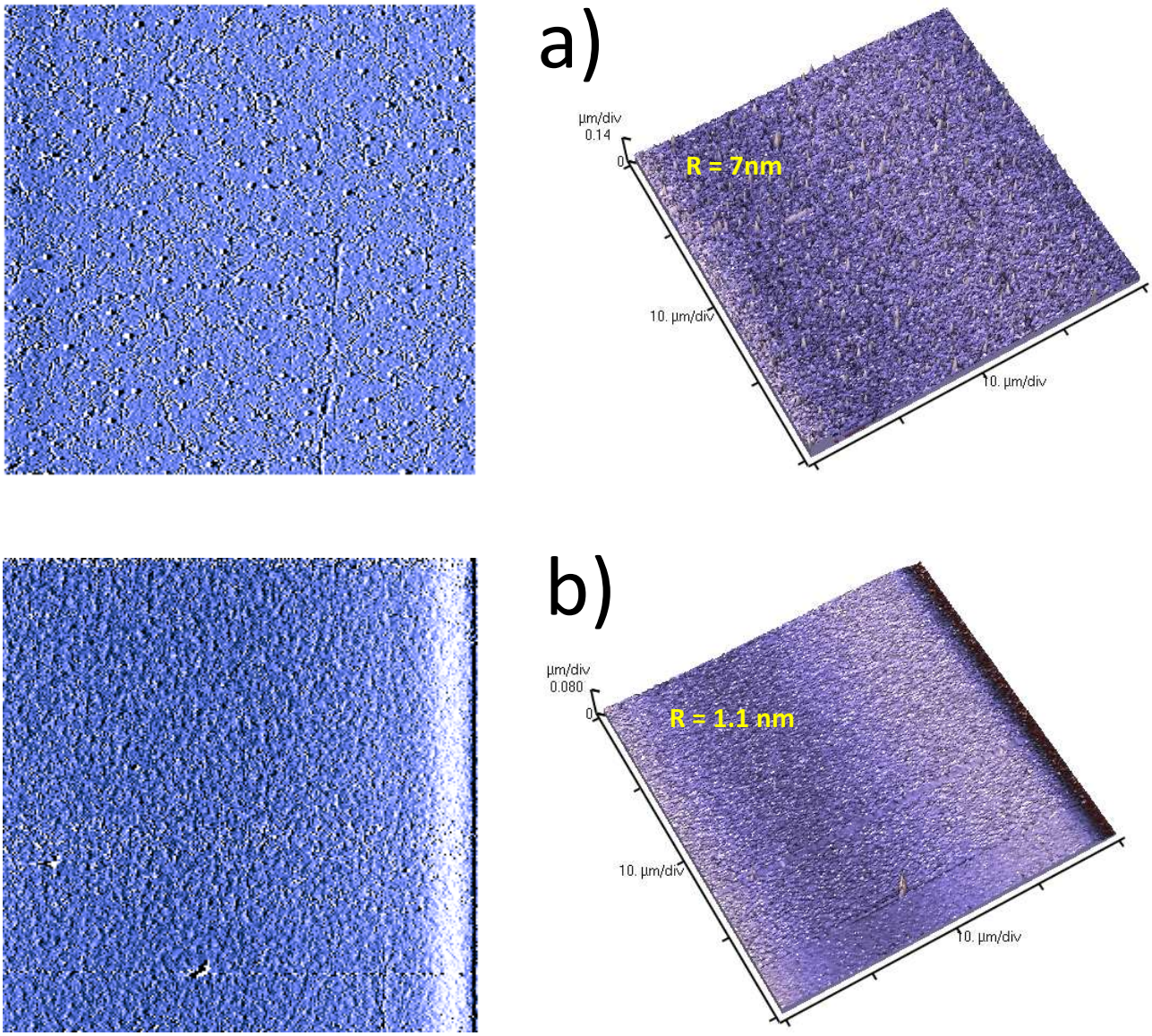

Fig. 4.12 *2D and 3D-AFM scans analysis of 19nm and 165nm thick PTFE films deposited on Si(100) substrates.*

experiments under the conditions optimized to obtain thin films (of about 20nm) on Si(100) substrates (see Fig. 4.10). Moreover, the preparation of Si(100)/ZrO_2/PTFE systems were carried out in a *one-pot* fabrication. In other words, both the target materials (pressed ZrO_2 powder and PTFE) were mounted on two cathodes in the sputtering chamber and deposited sequentially on the Si substrate. During deposition, the inactive targets were protected by shutters to prevent the materials from cross-contamination.

Unfortunately, for Si(100)/Ta_2O_5/PTFE systems a sequential deposition procedure was not possible because of the high temperature employed in Ta_2O_5 deposition (600°C). In fact, if PTFE target were present in the sputtering chamber, it could melt, or even burn, leading to damages to the sputtering instrument. Thus, these systems were prepared by a two-step fabrication involving

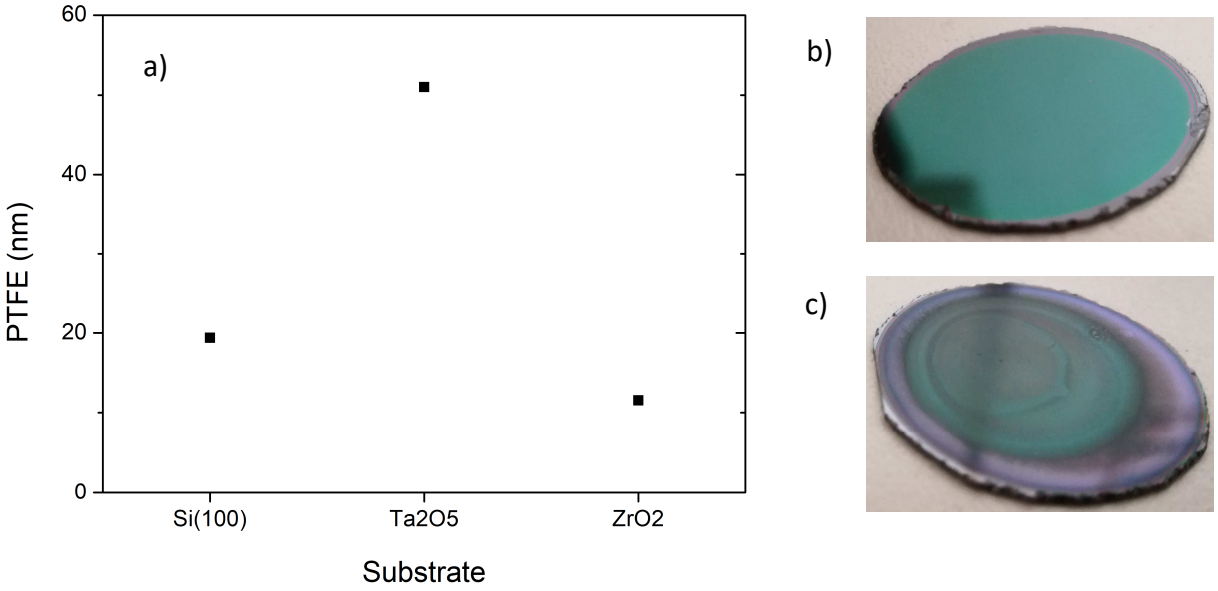

Fig. 4.13 *a) PTFE film thickness as function of the deposition substrate; b) Ta_2O_5 substrate deposited on Si(100) wafer); c) Si(100)/Ta_2O_5/PTFE final system (P=25W; d=10cm; p=5·10^{-2}mbar; t=20min.)*

deposition of a Ta_2O_5 film at first, followed by cooling of the sputtering system and PTFE deposition on Ta_2O_5 film. Fig. 4.13a shows the film thicknesses obtained for different substrates used in PTFE deposition. From this picture is evidenced as the substrate influences the amount of material that will be deposited. In fact, in the graph is clear that PTFE grows more rapidly in the case of Ta_2O_5 than in the case of ZrO_2 as the substrate material.

However, the sputtered film resulting from deposition on Ta_2O_5 or ZrO_2 are quite different. In fact, even if on Ta_2O_5 PTFE shows a deposition rate higher than that showed for ZrO_2, the quality of the resulting films is worse and they appear opaque and inhomogeneous. Fig. 4.13b-c shows the photographs of a Ta_2O_5 substrate before and after the deposition of PTFE on it. As can be clearly seen, the final PTFE film on Ta_2O_5 is opaque and presents circular concentric layers of PTFE. The reasons of this curious behavior of PTFE films grown on Ta_2O_5 are still under investigation. However, I think that it could be possible due to difference in surface tensions between PTFE and Ta_2O_5 or ZrO_2 films. This surface energy difference could lead to instability of the PTFE films on the oxide surface and develop strain forces that contracts the PTFE layer. In fact, film opacification is not directly seen after PTFE deposition. The “transformation” of PTFE films on Ta_2O_5 occurs gradually with time: it starts from a transparent film (appearing similar to Fig. 4.13b), then it passes from a transient, where opacification gradually covers all the sputtered area from the periphery to the center of the sample, and finishes with the complete opacification of the film (Fig. 4.13c). It is also observed that the opaque PTFE films are smaller than that they should be theoretically (considering the area exposed during sputtering deposition). In fact, as can be noted in Fig. 4.13c, the film is not

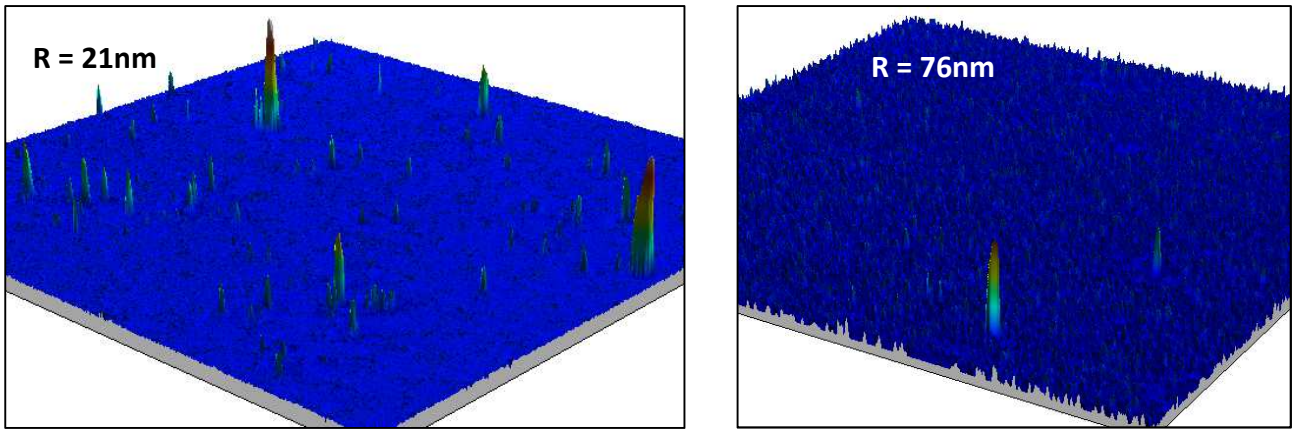

Fig. 4.14 *Profilometer analysis of sputtered PTFE film on Ta_2O_5: as-deposited (left) and after one week of aging (right)*

present at the edges of the substrate, due to film restriction. As previously said, this behavior of the PTFE films is observed only for Ta_2O_5 films as substrates, while for ZrO_2 no PTFE differences or opacification, with respect to the as deposited film, were observed.

The morphology of PTFE films on Ta_2O_5 was investigated by profilometry analysis on an as-deposited film (just after PTFE sputtering) and on the same sample aged for a week under atmospheric conditions (Fig. 4.14). From profilometry scans, the "transformation" taking place on PTFE films sputtered on Ta_2O_5 is clearly observable. From the profilometry scans of the as-deposited sample (Fig. 4.14-left), even if the roughness is high, if compared with PTFE on Si(100), the film can be considered homogeneous with the presence of granular defects. Examining a 2D profile extracted from the surface of the as-deposited sample, it can be noted that the trend of the roughness is similar to that found for PTFE films on Si(100), and that all the oxide surface was covered by the film. However, after aging for a week (Fig. 4.14-right), the surface morphology undergoes a deep change. In fact, roughness passes from 21nm to 76nm. Many of the grain defects observed for the as-deposited sample were included in the roughness of the aged sample. If a 2D profile is extracted from the surface, we can immediately observe that the PTFE is not yet equally distributed on the sample surface. Now, very thin regions are alternated by peaks that are considerably taller than those observed in the roughness profile of the as-deposited sample. At a first sight, it seems that the sample is composed of closed grains spread on the oxide surface. As said before, it's like if the PTFE sputtered film was instable and tend to contract itself through the center of the sample, leaving uncovered (or less-covered) areas. Since this contraction let portions of the oxide surface almost uncovered, this film is not suitable for REWOD measurements, where a complete coating is mandatory, not only for contact angle hysteresis, but also for insulating properties and charge trapping protection.

4.1.4 Energy harvesting tests

The last characterization performed on REWOD Ta_2O_5 and ZrO_2 samples, with and without PTFE coating, concerned their ability to perform mechanical-to-electrical transformation. As described in detail in the introduction section, this kind of energy harvesters belong to the electrostatic class. In fact, an external bias voltage to charge the parallel capacitor constituted by Si(100)/oxide-PTFE/liquid conductor, is needed in order to perform any energy harvesting cycle. Briefly, a REWOD device is composed by a parallel plate capacitor, where one of the two plates (liquid conductor) is mechanically deformable. Once the capacitor is charged, a mechanical excitation changes the contact area of the conductive liquid drop placed onto the oxide-PTFE layer, thus changing the *C* value of the capacitor. This, as for EPCs, causes an alternating flow of charges in the circuit, generating energy.

Because of the difficulty to obtain homogeneous and reliable PTFE films on Ta_2O_5, as discussed in the previous section, during this research project we tested under energy harvesting conditions only ZrO_2 and ZrO_2/PTFE systems. In particular, free oxide thin films and the ZrO_2/PTFE system were characterized in terms of energy generation and leakage current (I_L) as a function of the bias electric field (bias voltage, V_b).

In a typical reverse electrowetting measurement, the dielectric oxides were sputtered on Si(100) substrate disks of about 2cm of diameter. These samples were placed onto the back electrode test cell (Chapter 3.3, Fig. 3.5b(1)) were a brass plate, provided with a welded cable, works as electrical contact for the lower plate of the REWOD capacitor (Si(100) substrate) to the measurement circuit. Then, the cylindrical mercury container (Fig. 3.5b(2)), was placed onto the sample and clamped by the four screws present on the sidewalls of the back electrode test cell part. Finally, a 500mg Hg drop was placed onto the REWOD capacitor, confined by cylindrical container, and then the top mobile electrode (Fig. 3.5b(3)), was inserted into the cylindrical container to complete the assembly of the test cell. After the test cell was correctly assembled, the mobile electrode was fixed to the threaded piston rod, while the lower part of the cell was fixed to an aluminum slab, that is in turn fixed to the basement of the instrument, to avoid unwanted movements of the test cell during energy harvesting tests. At this point the REWOD device is ready for energy harvesting tests.

Fig. 4.15 shows the graphs obtained for the REWOD energy harvesting measurements and for the leakage currents detected for both the ZrO_2 and PTFE/ZrO_2 films. Looking at first to Fig. 4.15b, that reports the leakage current density of our systems, it can be noted that for both the systems

investigated the I_L is quite similar, with the PTFE/ZrO_2 one that at higher bias voltages conducts a little bit more than the pure ZrO_2. The measured values of I_L were plotted as current density values, also to facilitate the comparison with other REWOD works.

Fig. 4.15a shows the generated energies for the two systems. The REWOD experiments were carried out at 0.5Hz. As can be clearly noted, the PTFE/ZrO_2 generates much more energy with respect to the simple ZrO_2 film, confirming what observed by T. Krupenkin and J. A. Taylor. In fact, the presence of a thin fluoropolymeric film on the oxide layer (PTFE in our case) enhance the REWOD process performances due to reduction of contact angle hysteresis and charge trapping, that instead takes place with the only oxide layer, strongly reducing the system efficiency. The beneficial effect of the PTFE layer on ZrO_2 films is traduced into an increment of the harvested energy up to 450% at $2 \cdot 10^8$ V m^{-1} and 1.3 µJ $cycle^{-1}$ of generated energy value. Correctly, the trend of the generated energy is quadratic with the applied electric field, as discussed by the discoverers of REWOD phenomenon. In order to perform an easier comparison of the performances of our REWOD systems with other works present in the literature, energy and power density graphs were showed in Fig. 4.16. As it can be seen from the energy graph, our PTFE/ZrO_2 system is able to produce up to 7.5 nJ $cycle^{-1}$ mm^{-2} that results quite smaller if compared with energy density values reported by Krupenkin *et al.*, of about 100 nJ $cycle^{-1}$ mm^{-2}. This high difference could be ascribed to effective active area during harvesting cycles. In fact, during the treatment of REWOD results we considered that the effective active area of the capacitor during compression of the Hg drop, was the entire area of the hole of

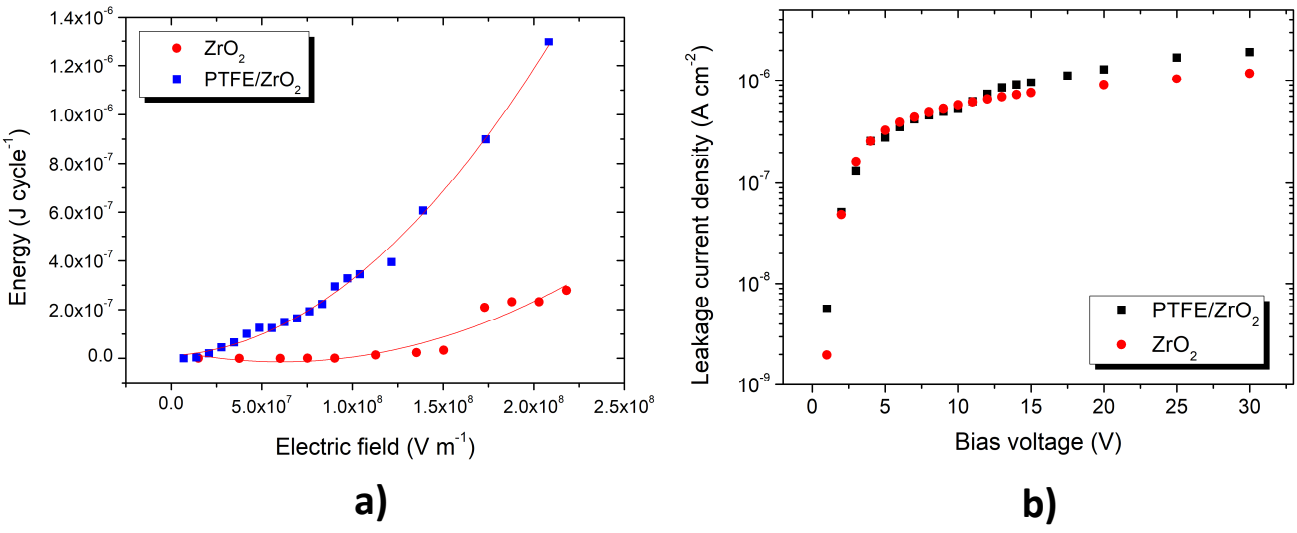

Fig. 4.15 *a) Comparison of generated energy between ZrO_2 and ZrO_2/PTFE REWDO systems as function of the applied electric field; b) leakage current density as function of the bias voltage*

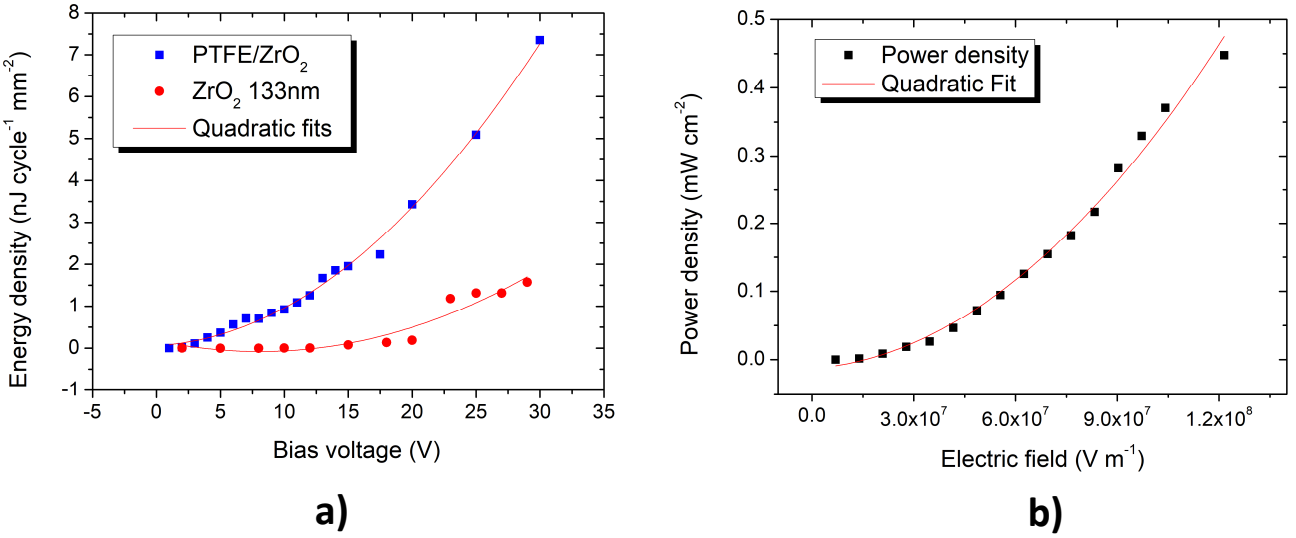

Fig. 4.16 *a) energy density comparison between PTFE/ZrO_2 and ZrO_2 REWOD systems; b) power density as function of the applied electric field.*

the cylindrical test cell. Since mercury has a very high surface energy, it is possible that, during compression, the Hg drop goes back to the internal walls of the cylindrical container, in the space between it and the mobile electrode. This could lead to an effective active area less than the theoretical one. The same observations made for energy density can be made for power density graphs. Also in this case, the output power density values were considerably smaller than that founded by other researchers. In fact, we obtained a maximum power density of 0.45 mW cm^{-2} at $1.2 \cdot 10^8$ V m^{-1}, while in literature values of 10 mWcm^{-2} are reported[49].

In conclusion, the leakage current density has been found in agreement with values reported in literature for similar sputtered systems, and it was not strongly affected by the presence of a thin layer of PTFE. Moreover, the presence of PTFE has a beneficial effect on the energy generation, that increases up to 450% with respect to the oxide without PTFE. However, values obtained for energy and power density were much less than those reported in literature. The cause of this was suggested to be the effective active area during measurements, which requires a careful analysis of drop behavior during the REWOD process.

4.2 Electrostrictive polymer composites (EPCs)

During the introduction section, among the electrostatic methods for harvest kinetic energy, we also discussed a class of materials called *electrostrictive polymer composites* (EPCs). These materials are composed of a filler (micro- or nanometric) dispersed into an elastomeric polymer matrix, to obtain higher dielectric constants ε with respect to the polymer itself. The elastomeric nature of the matrix is mandatory. In fact, stretching and relaxing a composite film when subjected to an electric field will generate an alternated current due to capacitance oscillation.

In theory, any type of material that possesses elasticity can be employed to build up such type of energy harvesters, but the combination of Young's modulus Y and dielectric constant ε of the polymer are key parameters to be considered to maximize the power output. Many polymers have been tested during years: silicones, poly-dimethylsiloxane (PDMS) in particular, are high stretchable, mechanical resistant and moisture resistant, but suffer from low dielectric constants. Another class are fluorinated polymers (p(VDF-TrFE) and p(VDF-TrFE-CTFE)), that have high ε (up to 60 at 1Hz) but also high Y, that reduces the efficiency and complicate the application of high strains. Also polyurethanes have been employed, combining good ε values, commonly between 5 and 15, and good Y, making them a good choice for this task.

Obviously, the filler employed is the other key component in EPCs fabrication. It can be conductive (carbon black, copper nanoparticles, graphene and so on), at loading level below the percolation threshold, or a high-k insulating material (*e.g.* PZT, $BaTiO_3$, $SrTiO_3$, etc.) at high %wt loading. The choice of the filler can be done also considering the type of polymer matrix, *e.g.* using a silicone matrix one could employ a high-k ceramic material at high loadings to increase the ε value while maintaining a good Y.

Another factor to be considered are the electrodes. They, ideally, should be compliant enough to follow the stretch/relax cyclic movement of the film during work, maintaining unchanged its conductivity properties, and, obviously, they should be as conductive as possible, to reduce the losses. Unfortunately, not many solutions are available, to date. The most common material employed when a dynamic electrode is needed, is *carbon grease*. It is a silicone rubber filled at high loadings with carbon black, which can be spread on the film, giving it the shape and dimensions desired, and then thermally cured to obtain an elastic and self-standing electrode. Further, carbon grease have a very high compliance under stretching but also high electrical resistivity, leading to loss increase. Another technique used recently for making dynamic electrodes is the sputtering process. By this technique is possible to deposit metals (*e.g.* gold) in the form of thin layers on the

surfaces of the EPCs, to be the plates of the capacitor. They, inversely to carbon grease, have a quite low compliance, but very low resistivity (*e.g.* ρ_{Au}=2.44 Ω·m). Thus, again, the most suitable type of electrode to be employed can be chosen considering the polymer matrix used to fabricate the harvester.

During our research project, we chose an ether-based thermoplastic elastomer (Estane 58887, Lubrizol) as the polymeric matrix, that combines good ε and Y values with a good moisture resistance due to the ether polyol monomer, that is less susceptible to degradation by hydrolysis with respect to the polyester-based polyurethanes. As the filler, I synthesize calcium copper titanate ($CaCu_3Ti_4O_{12}$) by sol-gel method, in the form of nanoparticles. This material has a giant dielectric constant up to 50,000, which remains constant over a very wide range of temperatures. These composites, at various vol% loadings, were obtained in the form of micrometric-thick films, as described in detail in the materials and methods section, coated with gold by *sputtering* to obtain compliant electrodes and tested into the measuring instrument designed and fabricated in our laboratories.

4.2.1 $CaCu_3Ti_4O_{12}$ nanopowder inclusion

Calcium copper titanate (hereafter abbreviated as CCTO) is an inorganic compound that crystallizes in the body-centered cubic lattice (s.g.: Im3, No. 204). The interest of CCTO as filler for EH devices is due to its large permittivity (up to 10^5) that is almost constant in a wide range of temperature[50]. CCTO can be prepared by conventional solid-state synthesis, by mixing of the oxide precursors and subsequent reaction at 1000-1100°C for many hours, or by the sol-gel process. This last method was used during our experiments to perform the reaction at lower temperatures and time (800°C, 30min), to obtain smaller particles size. After the sol-gel process, and after having acquired the X-ray diffraction pattern (Fig. 4.17a), the powder was subjected to a ball milling step, to further reduce the particle size of the powder. As shown in Fig. 4.17b, the most intense diffraction peak of the milled powder gets larger after this step, indicating a decrease in the size of the crystallites, according *Scherrer equation* for the determination of crystallites mean size:

$$\tau = \frac{K\lambda}{\beta cos\theta} \qquad \text{(Eq. 4.1)}$$

where τ is the mean size of the crystallites, K is a shape factor, λ is the radiation wavelength, β is the line broadening at half-maximum intensity (FWHM) and ϑ is the Bragg angle. Immediately after the thermal treatment of the precursor, the size of the crystalliytes is about 80nm, while after the ball milling step it ranges between 50-40nm. Fig. 4.17a shows the X-ray pattern acquired from the milled powder. Here all the peaks are attributable to CCTO without the presence of any impurity.

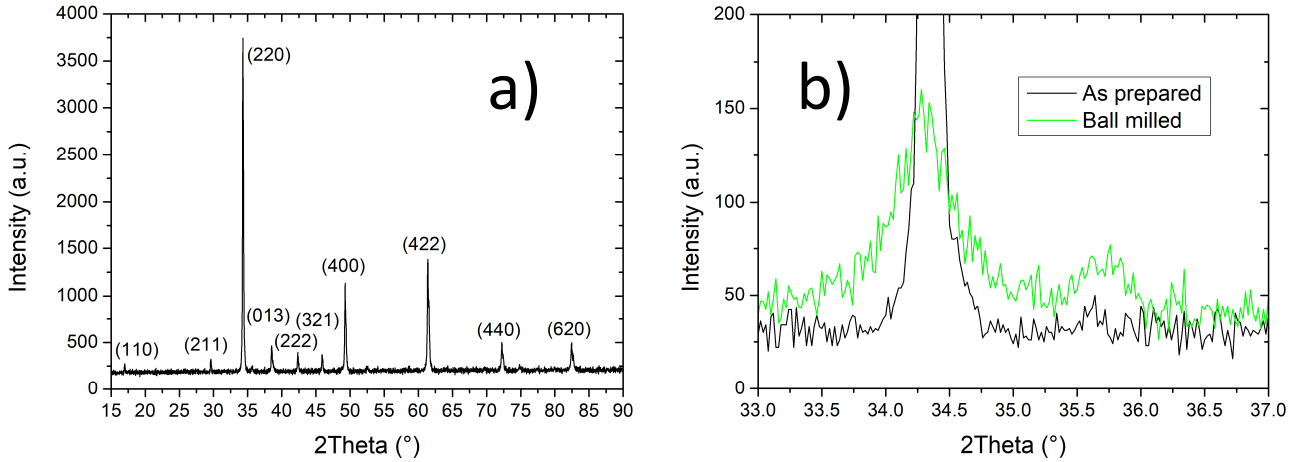

Fig. 4.17 *a) X-ray pattern of CCTO powder after ball milling, with the corresponding hkl indices; b) comparison between major peaks of CCTO powder before and after the ball-milling step. Ball-milled curve intensity is lower respect to the as prepared due to different measuring parameters used to perform the two measures.*

Once determined the correct synthesis and crystallites mean size of CCTO, the next step is its inclusion in the polyurethane matrix to obtain the nanocomposite. To do this, Estane 58887™ (Lubrizol Corp.) pellets were dissolved into DMAc (dimethylacetamide) and then a proper amount of CCTO was added to obtain from 10 to 70 vol.% loadings (d_{CCTO}=4.7g/cm^3). The obtained suspension was stirred, sonicated, poured onto a glass sheet and put into an oven at 80°C to evaporate the solvent and to obtain the final composite film. Fig. 4.18 shows the X-ray diffraction pattern obtained for the composite loaded at 30 vol.% with CCTO nanopowder. At a first sight, it is clear that the diffraction pattern is similar to that of the CCTO, except for a broad signal at about 20° that is due to the amorphous phase of the TPU matrix.

To investigate the morphology of the composites, scanning electron microscope (SEM) analyses were carried out for all the composites prepared, observing the cross-section and both up and bottom surfaces. Fig. 4.19 shows the images acquired for the cross-section of the composites prepared. As one can see, only for 10 and 70 vol% composites the dispersion of the filler can be considered homogenous in the polymer matrix.

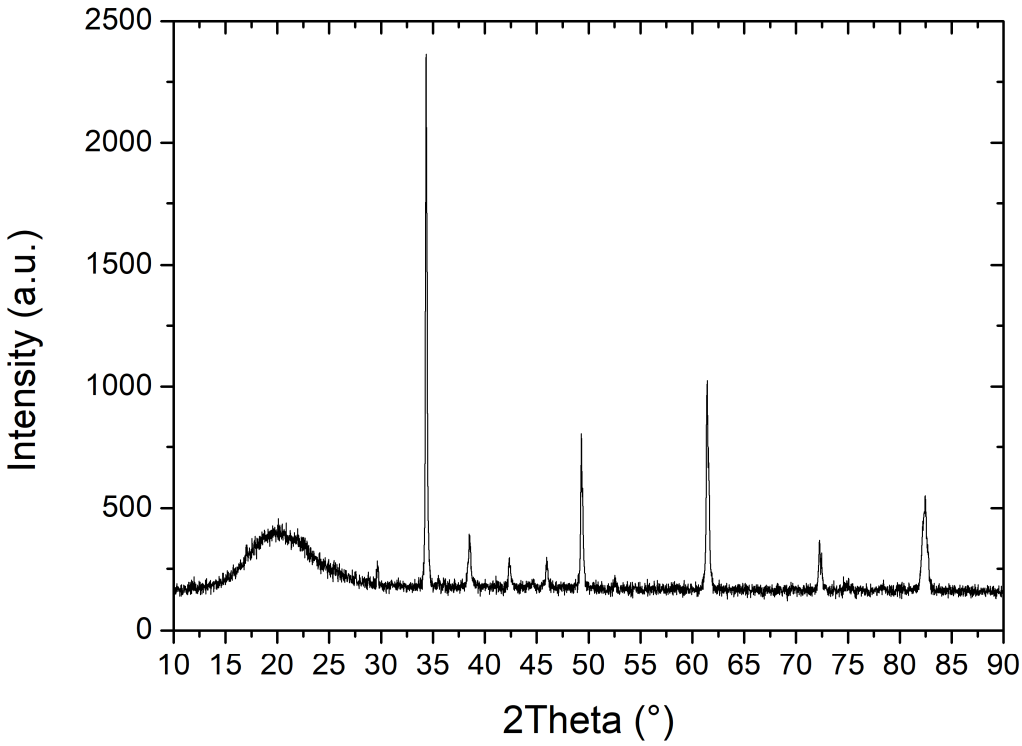

Fig. 4.18 *X-ray diffraction pattern of Estane58887-CCTO 30 vol% composite.*

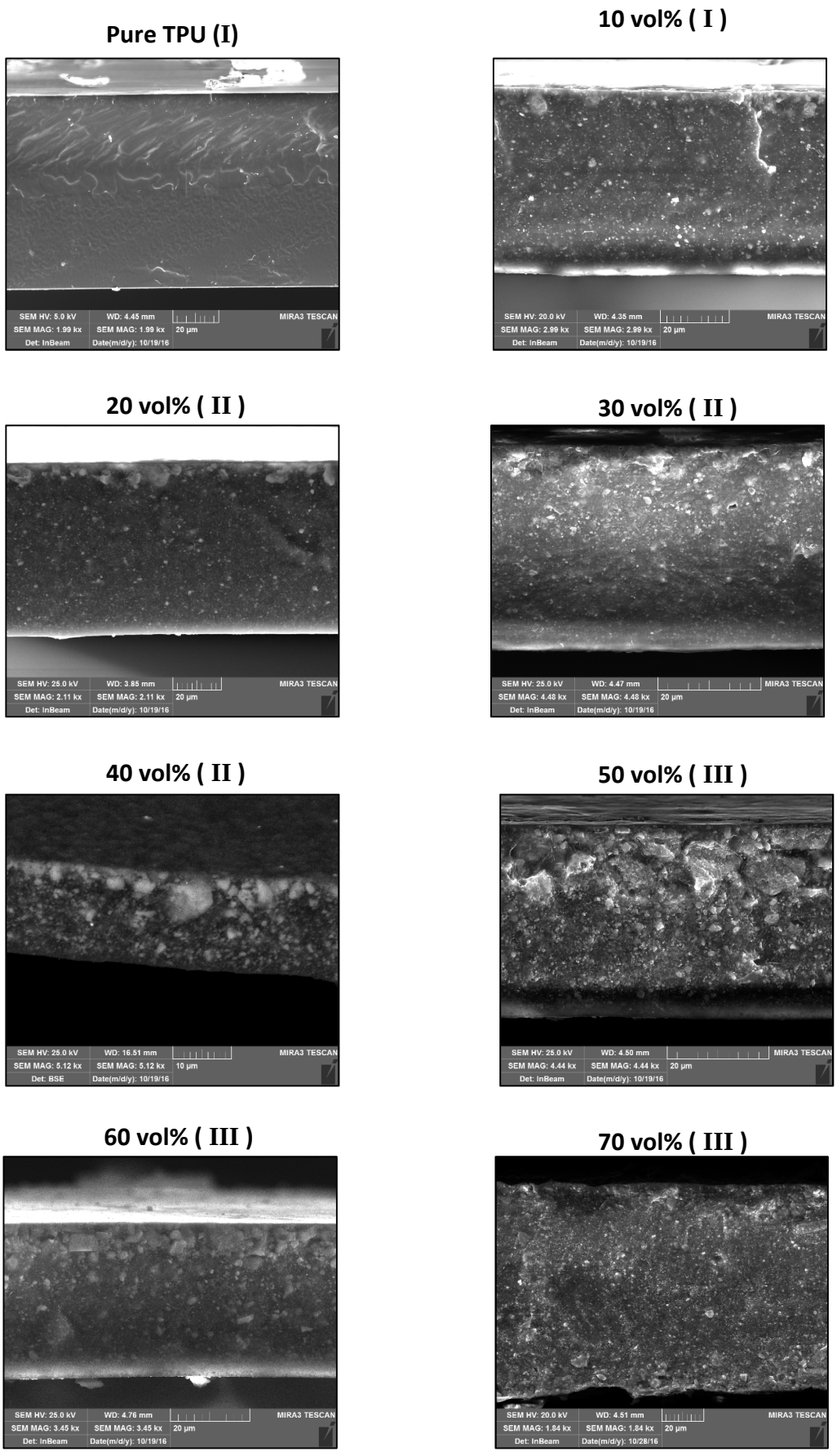

Fig. 4.19 *Cross-section SEM images for all the composites TPU-CCTO prepared. The 40 vol.% composite image was acquired using back-scattering detector, due to polarization problem during normal acquisition.*

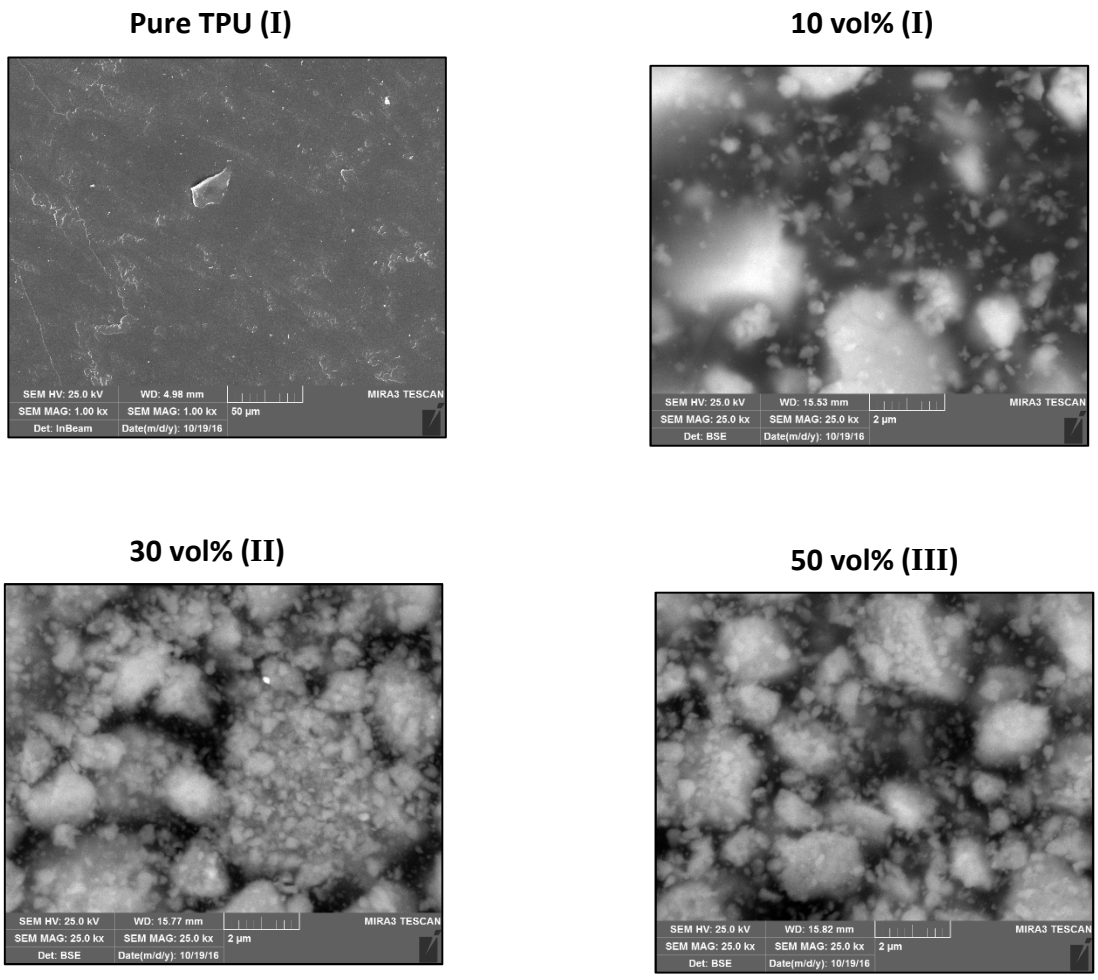

Fig. 4.20 *Representative back-scattering SEM images of bottom surfaces of the composites prepared.*

For all the other composites, it is clear that the dispersion is not homogenous through the cross-section, but that there is an enrichment of CCTO on the bottom surface (facing upwards in SEM images), that tends to be more marked by increasing the amount of CCTO loading up to 60 vol%. This trend can be attributed to the sedimentation of CCTO NPs due to agglomeration during the evaporation step. The inhomogeneous dispersion of the filler in the composite, with enrichment of the lower side, is a typical effect of solvent casting film fabrication, as reported for different polymeric matrixes, like P(VDF-TrFE)[51]. SEM images of the surfaces confirm what just established from cross-section images (Fig. 4.20). Increasing vol% CCTO loading, the agglomerates dimension increases, leading to a more pronounced sedimentation of the included filler. As observed from Fig. 4.20, for 10 vol% the agglomerates are quite small and well dispersed in the matrix, while for 30 and 50 vol%, that are similar, the agglomerates are sensibly bigger and not well dispersed. However, despite of the observed agglomeration and sedimentation of the high-loaded composites, all these materials conserve their insulating and elastomeric properties up to 50 vol%. Beyond this value, the

resistance starts to decrease and the composites become fragile, until 70 vol% composite that breaks even when subjected to moderate strains.

After morphology studies, also thermal properties of the composites were investigated. Fig. 4.21a shows the differential scanning calorimetry (DSC) thermogram of pure TPU matrix. Both heating and cooling steps were carried out with a temperature ramp of 10K min^{-1}. As one can see from 1st Heating DSC graph, at about 125°C is evident an endothermic event due to the melting of the polar crystalline domains in the TPU (Hard segments, HS). These HS are composed by sub-segments of MDI-BDO-MDI (MDI=1,1'-Methylenebis(4-isocyanatobenzene); BDO=1,4-butandiol) in the polymer backbone, that alternate with polyol soft segments (polytetrahydrofuran, p-THF), that constitute the amorphous and non-polar part of the polymer chain. HS of different near chains are also able to establish non-covalent interactions, leading to formation of crystalline regions, and thus creating a phase-separated material composed by crystalline domains inside an amorphous phase of p-THF.

Once 1st heating step reaches 230°C, the cooling step can start. At about 60°C there is a clear exothermic peak due to the crystallization of the HS parts discussed above for 1st heating step.

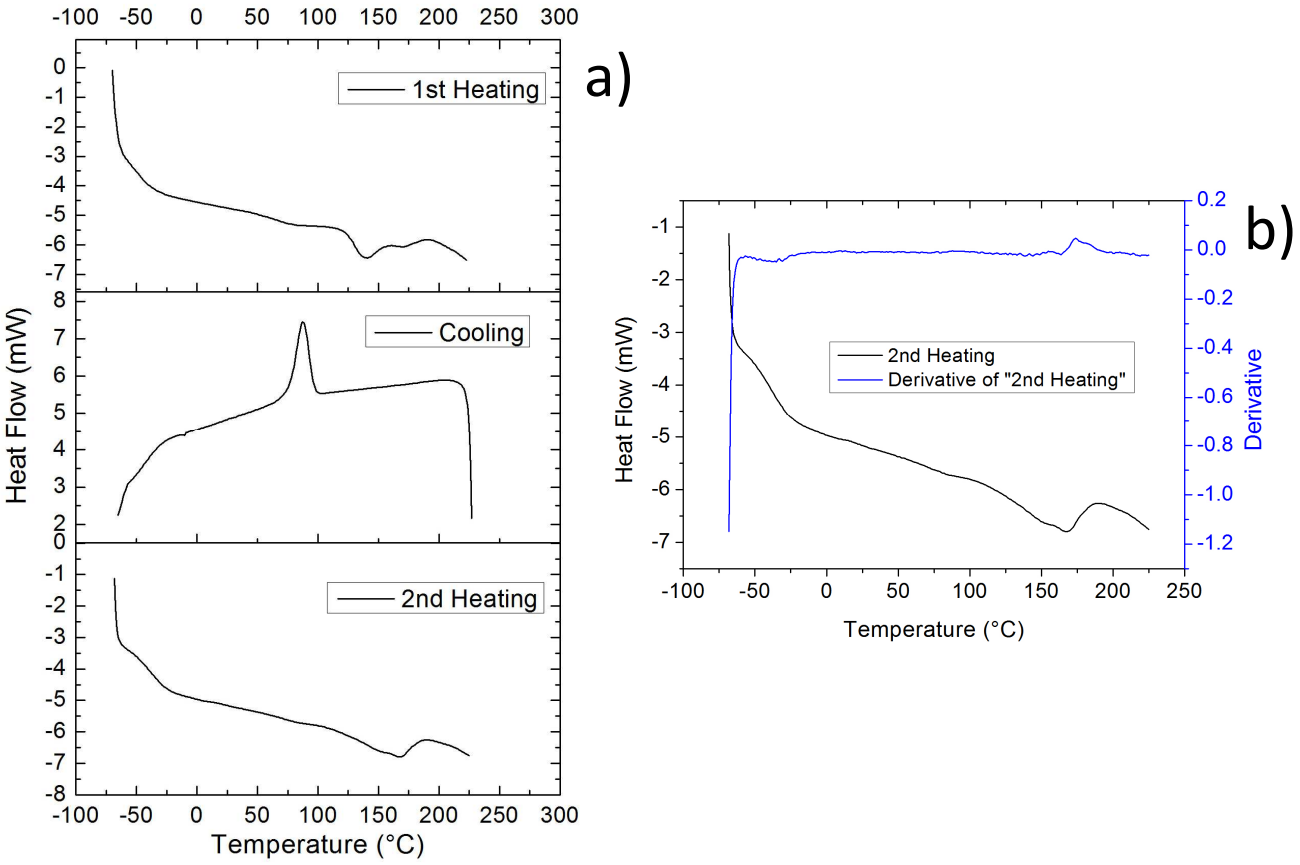

Fig. 4.21 *a) DSC graphs of pure TPU. Heating step: Trange= -70 – 230°C, 10K/min; Cooling step: Trange= 230 – -70°C, 10K/min; b) 2 nd heating step derivative to evidence exo- and endothermic events.*

Finally, the 2nd heating step, performed to evaluate the repeatability of the process, is showed in the lower quadrant of Fig. 4.21a. Also here the endothermic peak caused by HS melting is evident, but in this case the temperature is higher, passing from 150°C to 175°C. This behavior can be attributed to the *thermal annealing* to which the sample is subjected during the DSC measure. This annealing melts the crystalline part in the polymer, permitting them to reorder in a more organized fashion that melts again at higher temperatures. This is confirmed when comparing the shape of the two endothermic events in 1st and 2nd heating steps: the first peak is composed of two partially superimposed melting events (at 140°C and 175°C, respectively), attributable to short and long ordered HS, respectively; while in the second, only the higher one is present. Another clue to support this hypothesis, is given by the integrals of both the endo- and exothermic events, that are numerically equal in the three temperature scans at about 10J g^{-1}. This means that all the crystalline segments melted in the 1st heating, recrystallize during cooling and melt again in the 2nd heating step. As one can see, in both heating steps, from -50°C to 0°C a glass transition T_g occurs. This is more evident when considering the derivative of the DSC curve, as showed in Fig. 4.21b. Here, the changes in the slope of the DSC curve are more evident, and the T_g occurring at -40°C is quite evident and in a good agreement with the value of -45°C reported for this material.

Further, thermal characterizations were also carried out for all the vol.% composites. Fig. 4.22 shows the DSC scan graphs recorded using the same experimental conditions discussed for the pure TPU matrix. Starting from the 1st heating step, some considerations can be done. As can be seen from 1st heating DSC scans, the slope of the 10 vol.% curve is lesser than that of all the other composites, and is more similar to that of the pure TPU. This means that the 10 vol.% CCTO-TPU composite has a lower C_p with respect to the other composites prepared. In fact, as observed with SEM analysis, this composite is still quite similar to the pure polyurethane matrix due to still low percentage of filler volume included in it. On the other hand, all the other composites possess comparable slope of their DSC curves. Another consideration regards the HS melting event that occur in the range of 125-175°C for the pure matrix. As it can be seen, during the first heating step all the composites presents the signal relative to this event with no significant differences among them. However, in the cooling and second heating steps, neither crystallization nor subsequent melting were measured, meaning that the HS crystallization was inhibited by the presence of the filler, even at low loadings.

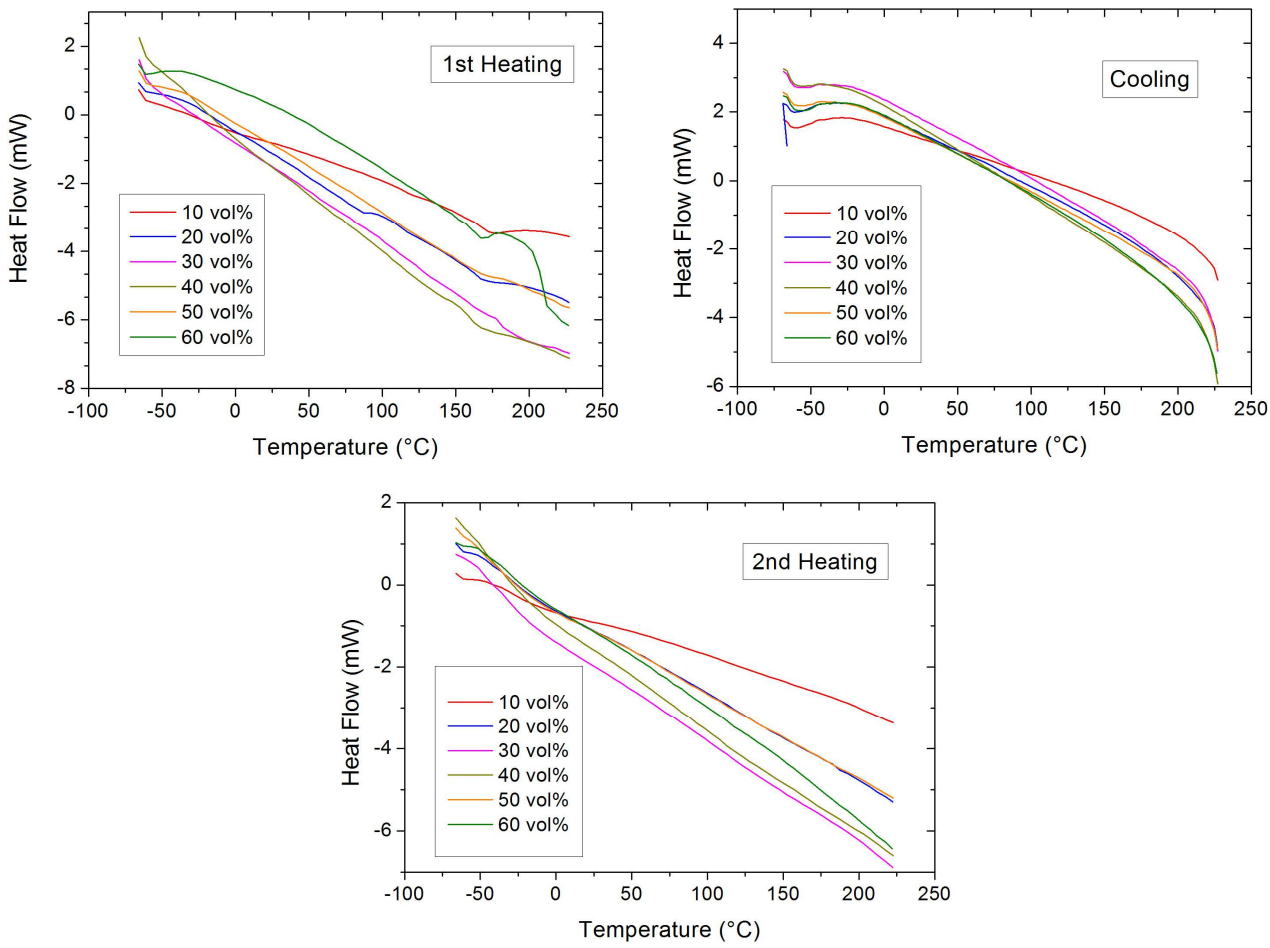

Fig. 4.22 *DSC scan curves relative to all the vol% composite $CaCu_3Ti_4O_{12}$-TPU prepared. All the thermal scans were performed in the temperature range of -70 – 230°C, with a ramp of 10K/min.*

The electric response of TPU-CCTO composites was investigated by Broadband Electric Spectroscopy (BES) at room temperature (25°C) and in the frequency range from 10^{-3} to 10^{7} Hz. The profiles of complex components of permittivity ($\varepsilon^*(\omega) = \varepsilon'(\omega) - i\,\varepsilon''(\omega)$) and conductivity ($\sigma(\omega) = \sigma'(\omega) + i\,\sigma''(\omega)$) with $\sigma^*(\omega) = i\,\varepsilon_0\varepsilon\,\omega$) are shown in Fig. 4.23. A careful analysis of the real and imaginary components of $\sigma^*(\omega)$ and $\varepsilon^*(\omega)$ allowed us to identify two electric response regions named P and D (Fig. 4.23). In agreement with other dielectric studies[52], carried out on conventional polymers, the polarization processes are peaked in P region, while the dielectric relaxation is observed in D. In P region, an electrode (σ_{EP}) and an inter-domain polarization event (σ_{IP}) is measured at low and high frequencies, respectively. σ_{EP} and σ_{IP} events are attributed to the accumulation of charges which occurs at the interfaces electrode/sample and [low-k]/[high-k] bulk domains, respectively. The σ_{EP} and σ_{IP} conductivity values are easily measured on the plateaus of $\sigma'(\omega)$ profiles at low and high frequencies of P region, respectively[53]. In D, the typical α-mode of polyether chains is observed[53,

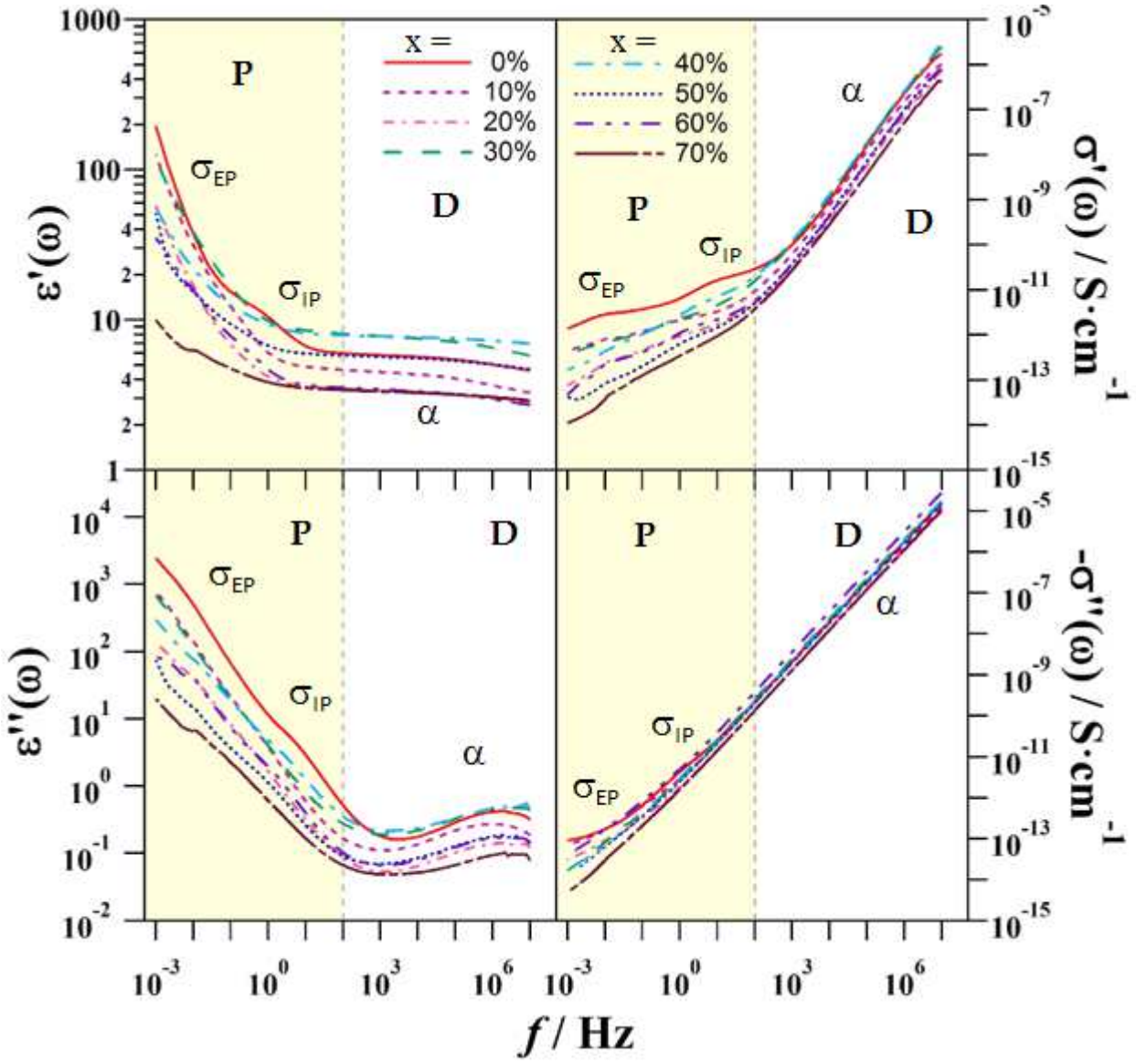

Fig. 4.23 *Real and imaginary components of complex permittivity (ε*(ω) = ε'(ω) – i ε''(ω)) and conductivity σ*(ω) = i ε0ε ω = (σ(ω) = σ'(ω)+i σ''(ω)) spectra as function of frequency (f in Hz) and x (v/v %). P and D indicate the regions dominated by polarizatio*

[54]. It is associated to the diffusion of conformational states, which occurs along polyether chains of soft polymer component, and corresponds to the dynamic glass transition temperature of the material. The relationship existing between relaxation rate of α-mode and the assignment of these event to the diffusion of conformational states, which corresponds to the segmental motion of polymer chains, can be easily proved by analyzing the dependence on 1/T of the f_α. This last profile, in our case, shows a Vogel-Fulcher-Tammann-Hesse (VFTH) behavior (data not shown) and accounts of the cooperativity of underlying molecular motions in polymer domains, which are significantly correlated to the viscosity of macromolecular component.

The dependence of σ_{EP} and σ_{IP} values on the volumetric fraction of filler (x) is reported in Fig. 4.24a. It is observed that on x: 1) three different conductivity regions (named I, II and III) may be

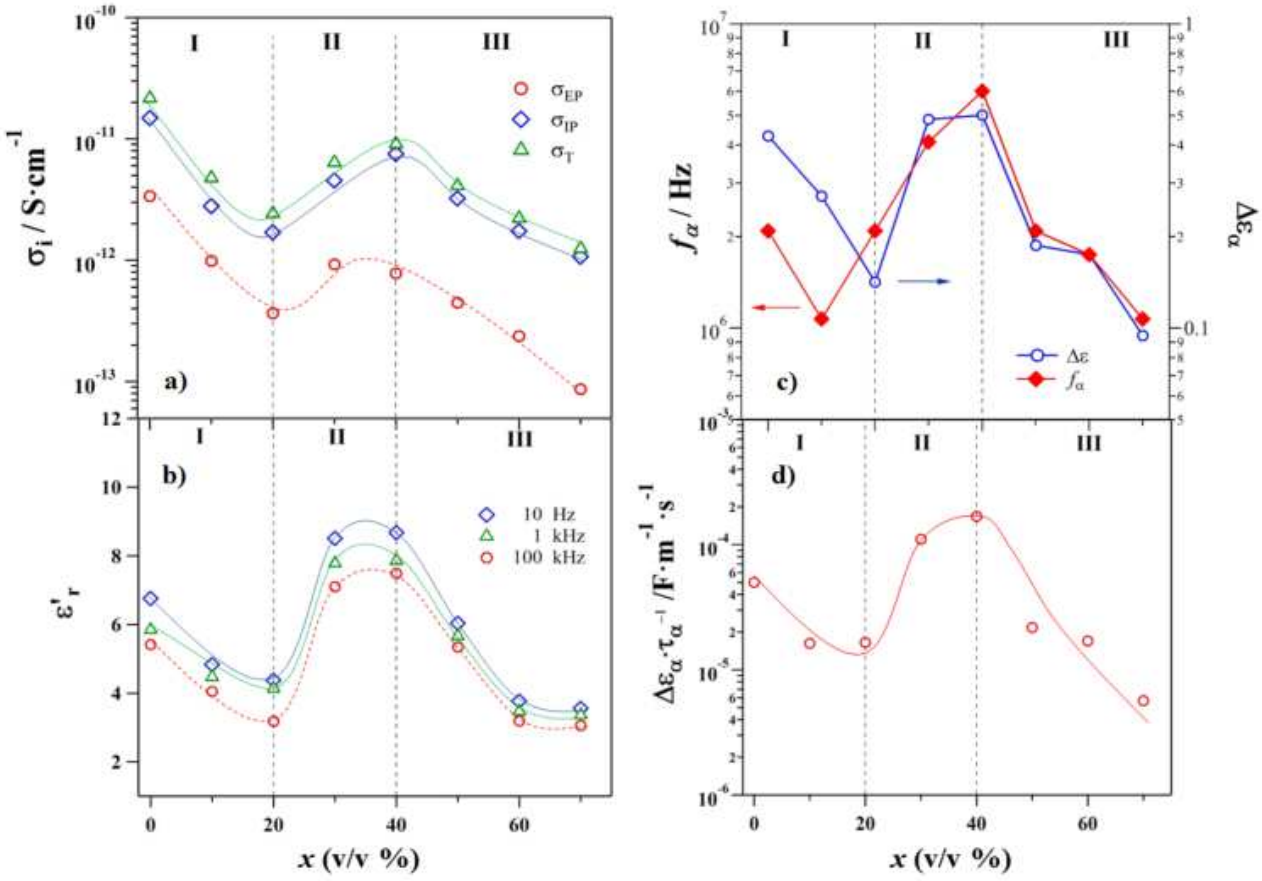

Fig. 4.24 *Behaviour of some relevant physical quantities vs. the volume fraction x (v/v %): (a) contribution of the different polarization processes to σi'; (b) ε'r at f=10-3, 1 and 100 kHz; (c) fα and Δεα (see text); (d) η = Δεα·τα-1 (see text).*

identified; 2) for all materials, $\sigma_{EP} << \sigma_{IP}$. In addition, on x, the conductivity values of σ_{EP} and σ_{IP} are monotonically decreasing in I ($0 \leq x < 20$ v/v %) and III ($x > 40$ v/v%) regions, while showing the opposite behavior in II ($20 \leq x \leq 40$ v/v %). These results demonstrate that in the investigated materials the long-range charge migration phenomena mainly occur along conductivity pathways, which are formed at the interfaces between high-k (the CCTO nanofiller) and low-k (the polymer matrix) domains. Actually, the overall conductivity of these materials is $\sigma_0 \approx \sigma_{EP} + \sigma_{IP} \approx \sigma_{IP}$.

On this basis, we should admit that in region I, polymer domains are larger and the density of charge "free to move" decreases as the filler concentration increases. In region II, most of the polymer component is involved in the formation of a polymer "shell" wrapping the filler nanoparticles (NPs). This interstitial NPs "shell" forms a "soft" and more efficient conductivity pathway. At $x > 40$ v/v % (region III) the polymer matrix starts being minority, whereas the CCTO phase is the main component. In this case, as it is expected by considering the conductivity of the two components, the conductivity of composite materials decreases as the amount of polymer decreases. Taking all together, BES studies demonstrate that the electric response of these nanocomposite material is significantly correlated to the ion and dipole dynamics taking place

within the thin interstitial layer of the polymer "shells" which are wrapping the high k-CCTO nanoparticles. A naïve picture of the three regions (I, II and III) is below reported in Fig. 4.25b. The dependence on *x* of the real component of permittivity at 10^{-2}, 1 and 100 kHz (Fig. 4.24b) is in perfect agreement with the trend above discussed for σ_{EP} and σ_{IP} values. The highest permittivity is observed for samples in region II.

Indeed, in this case the inter-domains polarization process is significantly influenced by the properties of interfaces between the polymer and the CCTO nanofiller. It results that the high-k component acts to polarize the "soft" material by increasing the intensity of dipole moments per unit of volume of polymer matrix, and thus concurrently increasing the overall permittivity of materials. This suggests that the polymer dipole moments are significantly coupled to the external applied field. This latter coupling phenomenon gets its maximum for samples with a concentration of nanofiller in the range $20 \leq x \leq 40$ v/v %. Further information on understanding the electric response of materials is obtained by analyzing the dependence vs. x of the frequency (f_α in Hertz) and dielectric strength ($\Delta\varepsilon_\alpha$) parameters of the α-relaxation mode (Fig. 4.24c). Here, f_α is defined as the frequency of the peak maximum, whereas $\Delta\varepsilon_\alpha$ is defined as the peak height. We can observe that in regions I and III both f_α and $\Delta\varepsilon_\alpha$ are decreasing vs. x. This can be easily explained by considering that the reorientation rate and the intensity of the overall dipole moment of polymer matrix is decreasing on x. Therefore, we can summarize that the dynamics and the intensity of the overall dipole moment per unit volume of the "soft" material: 1) is lower when one of the two phases composing the material is predominant in the sample; 2) is higher when x is ranging from 20 to 40 v/v %, i.e. when, in agreement with the SEM images, the size of polymer and inorganic CCTO domains are comparable. Thus, at the interface between high-k (filler) and low-k (polymer) domains strong interactions take place, which are responsible of the secondary structure of the polymer matrix and of the reorientation phenomena modulating the dynamics of polymer component. These results are confirmed by analyzing vs. x (Fig. 4.24d) the reorientation energy dissipation, η (i.e. the energy dissipated in heat owing to the dipole moment reorientation phenomena of polymer domains), determined using the equation:

$$\eta = \frac{\Delta\varepsilon}{\tau_{max}} = \frac{16\pi}{E_0^2}\xi \qquad \text{(Eq. 4.2)}$$

where E_0 is the amplitude of the applied electric field, τ_{max} is the relaxation time of the peak maximum of the α-mode, and ξ is the energy heat-dissipated per second and per unit volume of the sample. Fig. 4.24d shows that in I and III regions η decreases with x. In region II, η parameter increases with x, in agreement with the above-described results. This confirms that the interactions occurring between the low and high-k domains of materials are crucial to modulate and improve the mechanical energy harvesting effects exhibited by these materials. Finally, the correlations between σ_{EP}, σ_{IP}, σ_0 and f_α values (Fig. 4.25) were investigated, with the aim to discriminate how polarization and the α-dielectric relaxation are related to the electromechanical coupling processes at the basis of the energy harvesting capabilities of these materials.

The analysis of correlations shown in Fig. 4.24 confirms the presence of two correlation regions (C1 and C2). It is observed that σ_{EP}, σ_{IP} and σ_0 are strongly correlated to the α-mode and all behave similarly. Indeed: 1) in C1, they are decreasing and increasing monotonically on x and f_α,

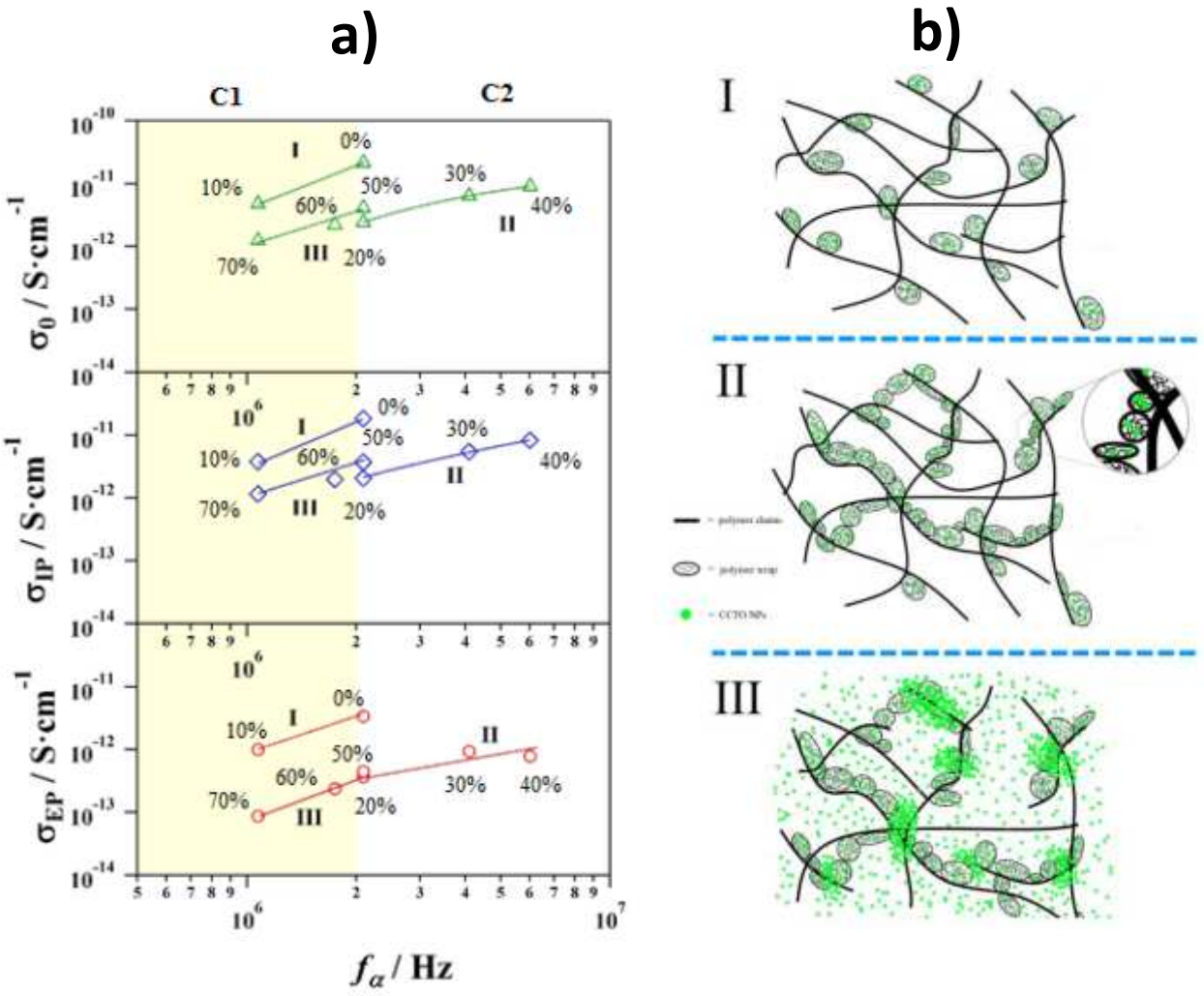

Fig. 4.25 *(a) Correlation between σ0 (top), σIP (middle) and σEP (bottom) and the frequency of dielectric α-mode (fα). I, II and III regions are indicated; (b) naïve picture of the three regions vs. x parameter.*

respectively; 2) in C2, they are increasing on both x and f_α. In addition, in C1, σ_{EP}, σ_{IP} and σ_0 of region I are better modulated by α-mode with respect to same values of region III. On this basis, we can admit that, with respect to III, in region I segmental motion is better modulating the long-range charge migration events. C2 included only region II, which shows conductivity values better modulated by the α-mode, with respect to III. Taken all together, if we consider a Smoluchowsky-Einstein process[55] for the long-range charge migration event, $\sigma_i \propto \langle r^2 \rangle f_\alpha$, a smaller slope is observed in II with respect to I and III. This suggests that the charge migration distance in II is smaller. In summary, the polarization phenomena occurring at the polymer-nanofiller interfaces (polymer "shells" directly interacting with high-k nanofillers) are strongly modulated by the segmental motions characterizing the polyether fragments of polymer domains.

The last measurements we performed on our TPU-CCTO composites were that concerning their ability to perform mechanical-to-electrical conversion when subjected to an external electric field. Since, to date, no existing instruments are available to perform such type of characterization, we built up (a prototype, at first, and then the optimized version) a home-made instrument able to do it. All the parts and features of both prototype and optimized versions were described in detail in the "Materials and method" section of this thesis (Chapters 3.3 and 3.4). In a typical energy harvesting (*EH*) test, a rectangular composite film strip (5x2 cm), provided with sputtered gold electrodes on both faces to form a parallel plates capacitor (A=6.8 cm^2), is clamped at its ends by a mobile jaw (connected to the rod of the piston) and by a fixed jaw. Inside the jaws, two electrical contacts connect the plates of the thin film capacitor to the circuit. Once the sample has been clamped, the pneumatic piston movement allows the user to set the frequency of activation (stress/relax cycle frequency). A bias constant electric field is induced across the strip by a power supply. Since the film is not an ideal insulator, the equivalent electric circuit must consider a loss resistance, R_L, in parallel to the variable film capacitance (Fig. 4.26). A leakage current, I_L, will then exist, which will be detectable with the oscilloscope placed across the experimental resistor (R_e). The current generated during the stress/relax cycles, I_G, must be higher than I_L to have a positive energy balance. In the case of polyurethanes actual film resistance is in the range 10^9 - 10^{11} Ω, which gives origin to $I_L \leq 10^{-7}$ A, in comparison with strain-induced currents, I_G, of the order of 10^{-5} - 10^{-6} A.

Fig. 4.26 reports the scheme of the electric circuit used to characterize EH properties of our composites. Within this experimental setup arrangement, in principle, the user can control the applied electric field (*E*), the frequency (*f*) and the amplitude of strain (γ).

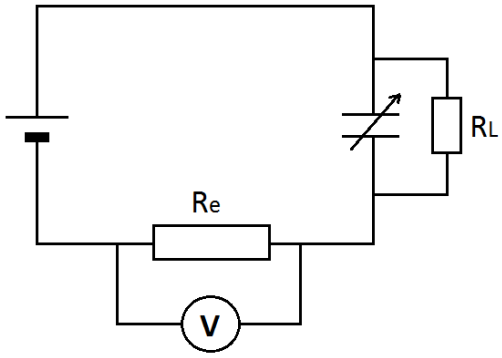

Fig. 4.26 *Scheme of the electric circuit for EH characterization. R_e: experimental resistance; R_L: loss resistance; V(circled): digital oscilloscope.*

Once the sample is clamped and the measuring conditions are set, the measure can start. The mobile jaw moves up and down inducing stress/relax cycles to the film strip. During the stress state, the film strip is subjected to a strain γ and experiences a capacitance increase of ΔC, that depends on many factors like filler content, amplitude of strain, frequency and derivative of strain. During our experiments on single strips we set a frequency of 1 Hz, a strain amplitude equal to 12% of film length and a square wave exciting profile. Fig. 4.27 reports two representative graphs that show the capacitance variation as the function of the applied strain. As one can see from these graphs, the capacitance variation has a linear relationship with the strain applied on the electrostrictive film. Considering data showed in Fig. 4.27, the filler content seems to affect ΔC and the value of capacitance at relax state, C_0. For example, $\Delta C_{12\%}$ are 120pF and 490pF for pure and 40 vol% filled samples, respectively, indicating that the filler provide a 400% increase in the capacitance variation. This is then reflected on the harvested energy by TPU-CCTO composites, that will be discussed in detail further in this section.

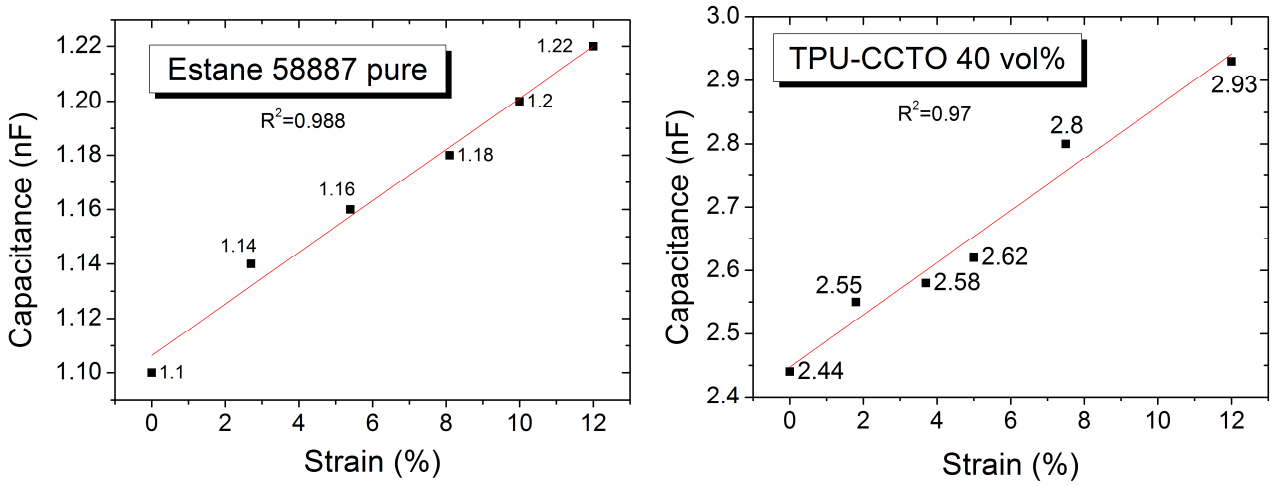

Fig. 4.27 *Capacitance vs strain graphs for unfilled and 40 vol.% CCTO loaded samples.*

As treated in the introducing section of this thesis, electrostrictive polymers need a bias voltage applied across their thickness (thus an electric field E=V/d, where d=film thickness) to perform mechanical-to-electrical conversion. In our experiments, the electric field is applied during time thanks to a high voltage power supply. When a bias voltage is applied to the film through its electrodes, it charges as a classic capacitor: higher the bias voltage is, higher will be the amount of charges stored on the film. When a strain γ is applied to the film strip, the area increases and thickness decreases leading to a capacitance increase (Fig. 4.27). Once stressed, the film is subsequently relaxed to its initial state causing a capacitance drop from ΔC_γ to C_0. This means that, to keep V_b constant, the *extra*-charges that have been stored during the stress state cannot be maintained and are pushed away from the electrodes to the external circuit. Positive and negative currents, generated during stress and relax cycles, pass through R_e causing a voltage drop across it, which is recorded by the oscilloscope. Fig. 4.28 reports some representative voltage graphs at different bias voltages, for the pure TPU matrix. The amplitude of the voltage scale was kept fixed to highlight the increase in current generation as function of the applied voltage. As evident, the voltage signal increases with the applied voltage, and the generated peaks are reproducible during

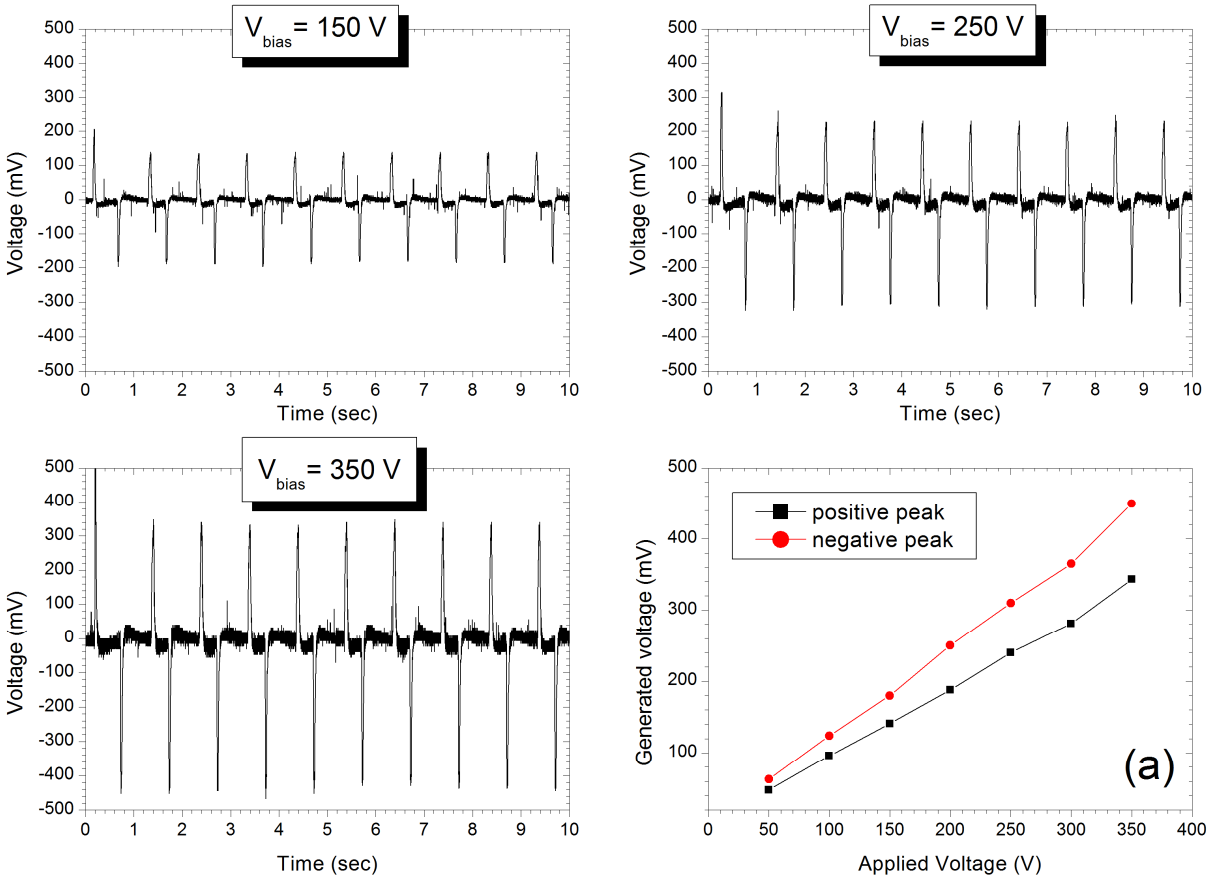

Fig. 4.28 *Voltage drop across experimental resistance (1MΩ) for different bias voltages applied to pure TPU films (f=1Hz; γ=12%). (a) Positive and negative peak values at different bias voltages.*

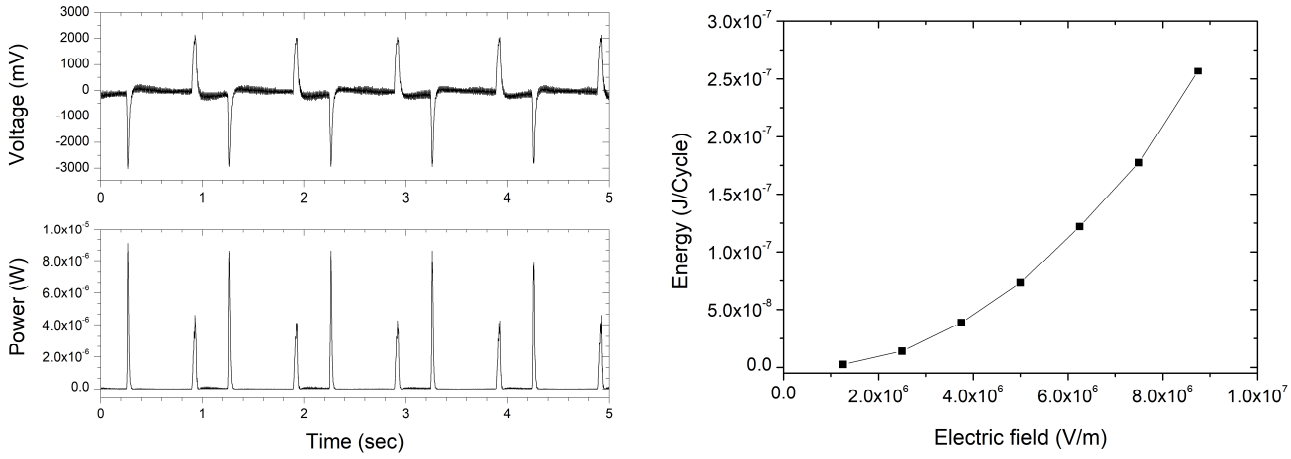

Fig. 4.29 *Left: Voltage and power graphs obtained from EH tests at E=8.75MV/m; Right: Energy vs Bias electric field graph. All the graphs refer to the 50 vol% composite (f=1Hz, γ=12%)*

all the measuring scans. Another point that can be noted is the asymmetry of the positive and negative voltage peaks, with these last which are more intense than the others. In Fig. 4.28a are reported the absolute values of positive and negative voltage peaks recorded for the bias voltages investigated. Noteworthy, the intensity ratio between negative and positive peaks is constant at about 1.3, suggesting that this discrepancy is not related to the electrochemical phenomenon occurring in the electrostrictive polymers. The peak asymmetry can be explained from a mechanical point of view: when performing a stress, the film elongates and an opposite force, $F = -kx$, acts against the exciting direction slowing the attainment of the maximum applied stress. This is reflected in the current generation that gives a larger and less intense peak. On the other hand, passing from stress to relax state, the movement has the same direction of the elastic force, so leading to a more rapid completion of the relax phase, with respect to the stress one, that give a narrower and more intense peak on the voltage versus time graph.

When all the voltage graphs at different bias voltages are recorded by the oscilloscope, these can be converted into power vs time graphs by combining the Ohm's law (V=IR) with the equation of power (P=VI) to obtain the well know equation of power as function of voltage and resistance: $P = V^2/R$ (Fig. 4.29 – left). Subsequently, from P vs t graphs, the energy per cycle is obtained by integration of two power peaks, one deriving from positive current and the other from negative current. The energy values were then plotted as a function the bias electric field, as showed in Fig. 4.29 – right. As clearly visible, the energy generation has a quadratic relation with the applied electric field, confirming that the bias voltage to which electrostrictive films are subjected is an important factor to be accounted to maximize energy generation. Asymmetry of positive and negative peaks found in the voltage graphs, is even more evident in the power graphs. Furthermore, considering the integral values of power peaks deriving from positive and negative currents, it can

be noted that, as in the case of voltage signals, the integrals ratio oscillates around the 1.3 value (data not showed). Hereafter, for comparing the energy harvesting capabilities of different composites, we decided to consider energy instead of power because it is independent from derivative of strain, permitting us to consider only frequency, bias electric field and amplitude of strain as affecting experimental conditions.

As we said previously in the case of ΔC, among different energy generation variables, filler loading seems to be one of the most important in order to increase EH capabilities of these materials. Fig. 4.30 shows the energy generation profiles as function of the applied electric field for different CCTO-loaded composites. What can be immediately noted from Fig. 4.30 is that the quadratic relationship between generated energy and electric field is maintained for all the composites investigated. The other fact that arises clearly is that the higher the CCTO content is, the higher the energy generation is (at the same applied electric field). This is true only for composites up to 50 vol.%, beyond which the energy generated starts to decrease. This can be ascribed to the filler volume that is more than that of the polymer, making losses (*e.g.* loss of elasticity) more remarkable, thus reducing the efficiency of the harvesting process. Energy generation increase for TPU-CCTO composites arises from capacitance variation ΔC, as discussed above. Increase of filler content in TPU matrix leads to an increase of both C_0 and ΔC (Fig. 4.27), that are in turn related to the ε_r value increase of the final composite because of the inclusion of CCTO NPs (Fig. 4.24b). The beneficial effect of CCTO inclusion

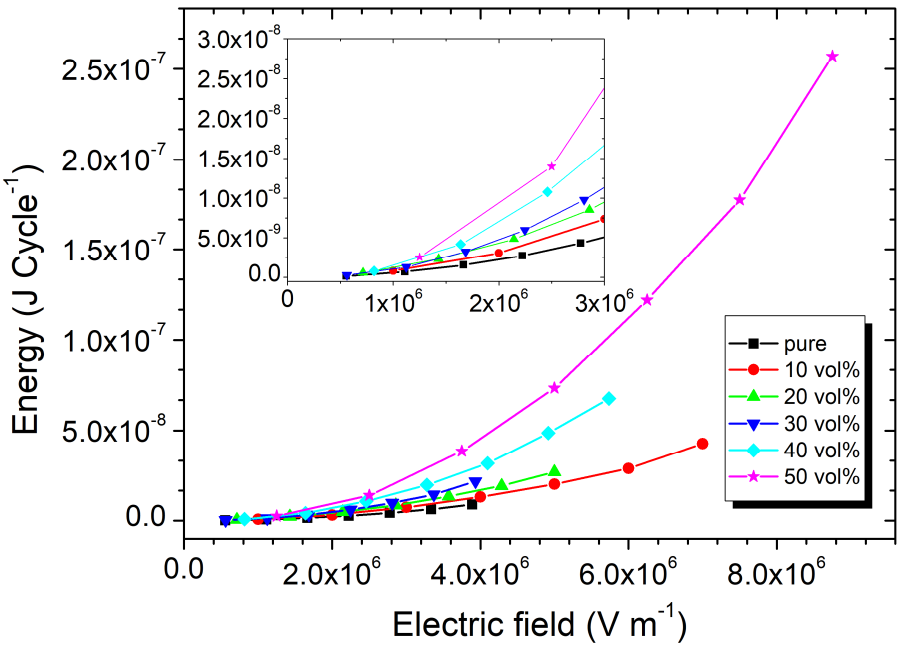

Fig. 4.30 *Energy generation of composite as function of bias electric field E, for different CCTO loadings. The inset show clearer the energy values for low applied E (f=1Hz; γ=12%).*

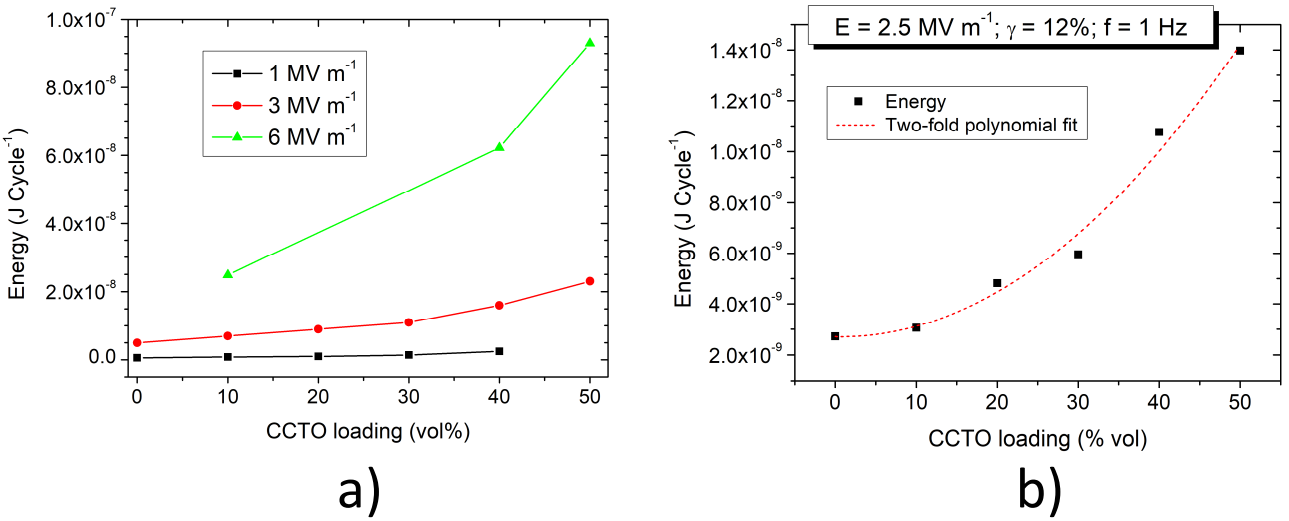

Fig. 4.31 *a) energy generation as function of filler loading for different bias electric fields (f=1Hz; γ=12%); b) quadratic trend of energy generation as function of filler loading*

on energy generation is evident even at low electric fields, as showed in the inset of Fig. 4.30. As the filler content increase, the slope of the energy curve increase. This lead to a significant improvement in the EH properties of these materials with respect to the TPU matrix itself. In fact, comparing generated energy values at E = $4 \cdot 10^6$ V m^{-1}, the energy generation passes from 9 nJ $cycle^{-1}$ to 40 nJ $cycle^{-1}$, for pure TPU and 50 vol.% composite; corresponding to a 444% increase in energy generation and an energy density of 1.48 µJ cm^{-3}. These values become even larger at higher electric fields up to $8.75 \cdot 10^6$ V m^{-1}, where the TPU-CCTO 50 vol.% composite generates 8 µW of power peak and 0.25 µJ $cycle^{-1}$, that correspond to a power density of 296 µW cm^{-3} and an energy density of 9.5 µJ cm^{-3}. It corresponds to the half of the best value obtained for electrostrictive energy harvesters, that correspond to 607 µW cm^{-3} [56], but some considerations must be accounted. In fact, the authors obtained this value in different (more energetic) conditions with respect to us: being E = 10^7 V m^{-1} (quadratic relation with power), f = 10 Hz (linear relation with power) and γ = 4.5% (linear relation with power). Thus, it is reasonable that our system can reach similar or even higher power values under those conditions.

The dependence of the generated energy as function of the CCTO content into the polymeric matrix, is even more evident in Fig. 4.31b. Here, considering constant experimental conditions, it is clear that the filler content has a quadratic relation with the energy generation level. However, the quadratic trend is true only up to 50 vol.% loading of CCTO in TPU matrix, while for higher loadings (60 and 70 vol.%) the energy generation starts to decrease. This is in accordance with BES results: increase in CCTO content from 0 vol.% to comparable vol.% between low-k matrix and high-k filler leads the an increase in CCTO/TPU interface that increases the overall dielectric constant. But, while for ε_r the best value is reached at 40 vol.% of filler loading, here the maximum generation is achieved with composites at 50 vol.% of included CCTO NPs. A possible explanation of this can be obtained by considering what arose from BES studies. When the polymer and filler volume fractions become comparable, the TPU matrix, into which CCTO is dispersed, forms a sort of wrappings (see Fig. 4.25b-II) that surround CCTO NPs, maximizing the high/low-k interfaces and, thus, maximizing ε_r, that reach its maximum at 40 vol.%. At the loading of 50 vol.%, almost all the CCTO NPs are wrapped, but a little amount is excluded from them, contributing to the formation of phase III, as showed in Fig. 4.25b-III. It is possible that this condition is true in a relaxed state, where wrappings are static (giving BES results in region III), but can be dynamically changed by stretching the composite. This concept has been visualized as in Fig. 4.32. Upon stretching, the film decreases its thickness causing a decrease of the inter-chain spacing and thus leading to the approach of polymer wraps. When

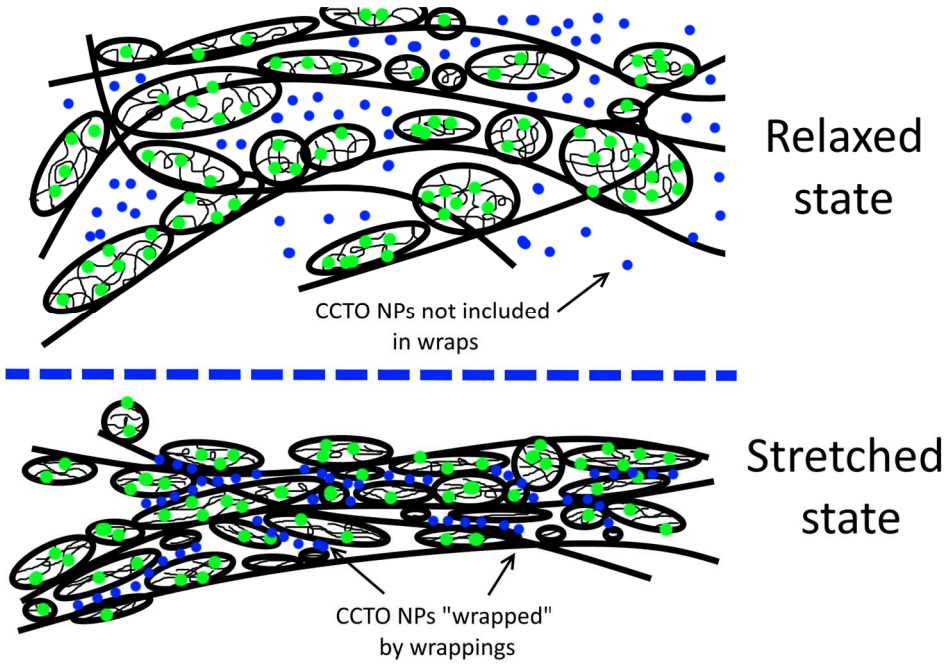

Fig. 4.32 *Naïve picture of dynamic "wrapping" of excluded CCTO NPs in 50 vol.% composite. Green dots: CCTO NPs wrap-included; Blue dots: CCTO NPs wrap-excluded; black lines: polymer backbone chains; black ovals: polymer wraps.*

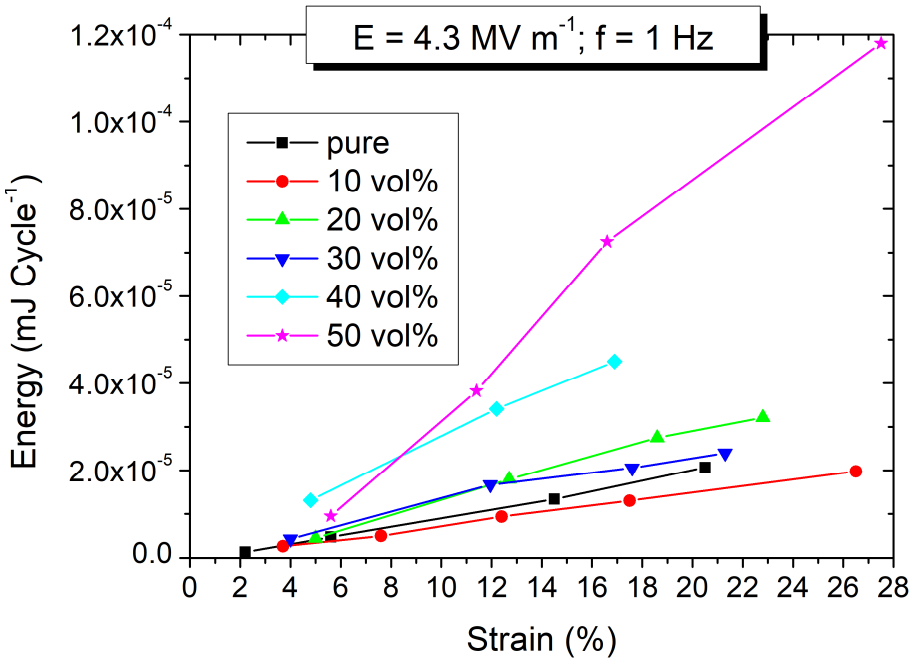

Fig. 4.33 *Dependence of energy generation as function of the applied strain for different CCTO-loaded composites.*

wraps are numerous, as in the case of 50 vol%, their approaching fulfill the inter-chain space, constraining excluded CCTO NPs into a wraps network that has the final effect to increase the overall number of high/low-k interfaces in the material, and thus to increase the capacitance due to higher polarizability of this material.

Fig. 4.31a shows how the maximization of both CCTO content and electric field can affect the energy generation. Passing from pure TPU matrix at E =10^6 V m^{-1} to 50 vol.% at E = $6 \cdot 10^6$ V m^{-1}, the energy raises from 0.6 nJ $cycle^{-1}$ to 93 nJ $cycle^{-1}$, respectively, that is more than two orders of magnitudes higher. When starting this discussion, we considered the variables that affect the energy generation when using EPCs. Beyond that discussed above, also the applied strain has a role on the amount of energy harvested by these materials. Fig. 4.33 shows the trend of energy harvesting vs the applied strain, for different composites, under constant experimental conditions (E = $4.3 \cdot 10^6$ V m^{-1}; f = 1 Hz). For all the samples, there is an almost linear relationship between the applied strain and the generated energy. Except for 10 vol.% composite, which constitutes an outlier, the higher the loadings the higher the slope is. In particular, for composite 50 vol.%, the slope of the curve undergoes a marked increase, reaching much higher energy values with respect to all the other samples. This can be attributed to what said for the dependence of energy generation on *E* and CCTO loading, as depicted in Fig. 4.32. In the particular case of the 30 vol% composite, at large strains the generated energy increase is less than expected from the linear behavior. This could be caused by an inhomogeneous dispersion of CCTO in the sample, with the formation of percolating pathways

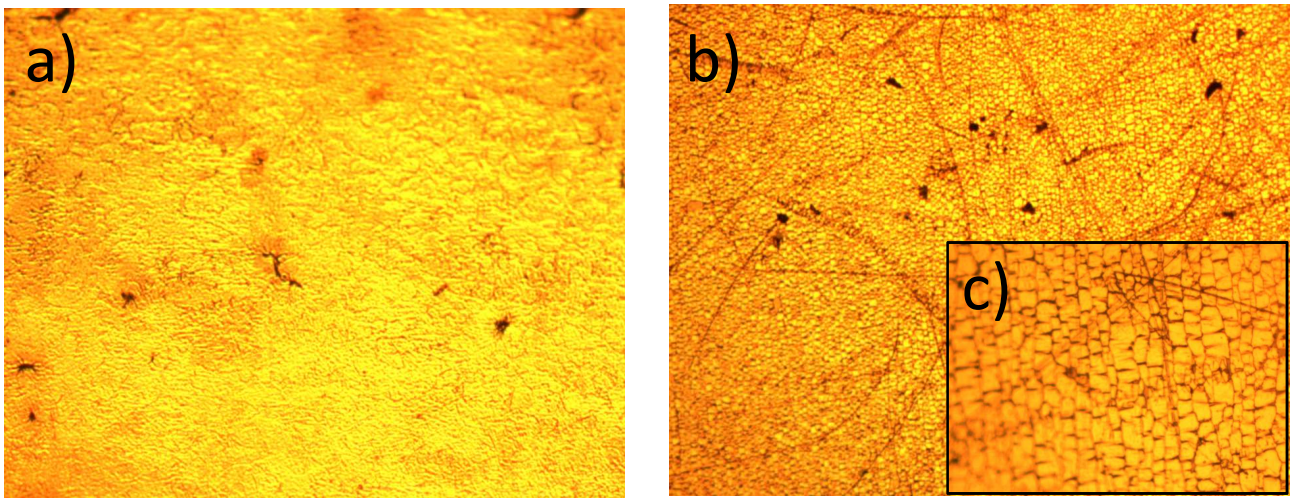

Fig. 4.34 *Optical microscope photographs of gold electrodes sputtered on TPU films: a) as-deposited gold electrode at 5x zoom; b) gold electrode after 1000 activations at 5x zoom; c) zoom at 10x of the same electrode showed in b).*

through its section. The 50 vol.% is able to generate an energy value about one order of magnitude higher than the pure one. Unfortunately, due to limitations related to the components of the measuring instrument, it was not possible to investigate the relation between energy generation and frequency for the CCTO composites prepared. This will be the object of future investigations that will become possible with improvements of the measuring instrument.

In the introduction of this section, we also mentioned the importance of compliant electrodes on the reliable energy generation properties of electrostrictive polymers. Since the EPC film has to be stretched to work, the electrodes must be able to sustain the strain without losing their conductivity properties. Fig. 4.34 shows the optical microscope photographs taken before and after generation measurements (about 100000 cycles). As it can be seen comparing Fig. 4.34a and b, the working process of the generating films has an effect also on the structure of the gold electrodes. In particular, as said in the introducing part, sputtered metal electrodes possess very high conductivity, but tend to be less compliant with respect to their polymeric counterparts. This is confirmed even looking at Fig. 4.34b and c where the “cracking” to which the electrodes are subjected during EH cycles is observed. Despite the evident cracking of the electrodes, no evidences of conductivity lost was found even after more than 100000 cycles of activation, leading to energy generation stable and constant during time.

Another important aspect to be considered when designing EPCs energy harvesters is the elasticity of the generator film. This means that the composite fabricated should be elastic enough to be easily stretched, in order to harvest a range of exciting forces as wide as possible, and to restore its initial dimensions when exciting forces are absent. A typical analysis to study the mechanical properties of a material, is the tensile testing. This type of test involves the stretching

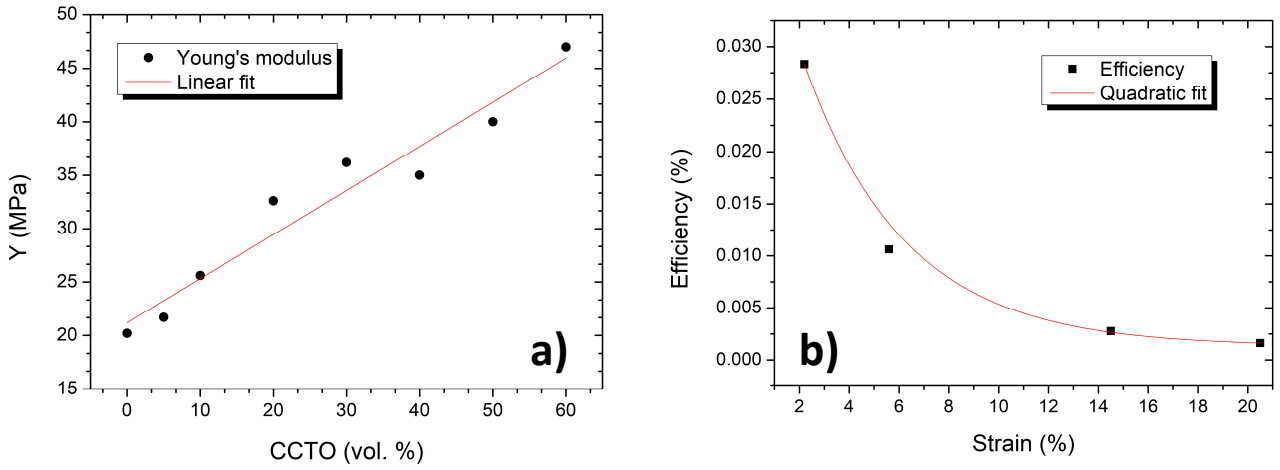

Fig. 4.35 *a) Young's modulus of TPU-CCTO composite as function of CCTO vol. % loading; b) Energy generation efficiency of pure TPU matrix as function of applied strain.*

of an homogeneous sample, of known section area and initial length, for a given stretching amplitude (or until rupture) while recording the force applied to reach such strain (see Chapter 2.5.7 *Tensile testing*). This analysis permits us to obtain stress-strain curves of all the composites prepared, and thus to extrapolate the Young's modulus *Y* from the slope of their curves. Fig. 4.35a shows the *Y* values obtained as function of CCTO content in the polyurethane matrix. As clearly observable from this graph, the increase in CCTO content leads to the increase of *Y* of the composite, as expected. In particular, this increase is linear with the CCTO content and causes an increase of almost 100% of *Y* from pure matrix (20 MPa) to TPU-CCTO 50 vol.% composite (39 MPa). However, despite of the Young's modulus increase, composites up to 50 vol.% can be considered as feasible for EH because the force needed to stretch it up to 12% is still quite low. In fact, passing from pure to 50 vol.% composite, the force to stretch the a 5x2cm film strip at γ=12% increases from 2.6N to 7.5N, that can be considered compatible with forces developed during human motion.

Beside elastic information, *Y* permits us also to obtain the mechanical power given to the system (P_{mech}) when stretched, and thus to calculate the efficiency of the process, comparing it with generated electrical power. By considering the classic equation for elastic energy per unit volume and the frequency of activation, the equation to calculate the input mechanical power per unit volume is:

$$P_{mech} = \frac{YS^2}{2f} \left[\frac{mW}{cm^3}\right] \qquad \text{(Eq. 4.3)}$$

where *Y* is the Young' modulus of the material, *S* is the applied strain to the film and *f* is the frequency of excitation of the generator. Once calculated P_{mech}, the efficiency (‰) can be calculated as:

$$\eta\ (‰) = \frac{P_{gen}}{P_{mech}} \cdot 1000 \qquad \text{(Eq. 4.4)}$$

As it can be noted from data available in Table 4.7, the efficiency increases with the increase of CCTO content in the polymeric matrix until it reaches its maximum at 50 vol. %. This is in agreement with energy generation graphs showed previously (Fig. 4.30). The low values of efficiency obtained can be explained considering the high strain (12%) value and the quite low applied electric field. In fact, as showed in Fig. 4.35b, the strain has a quadratic relation with efficiency, as expected considering P_{mech} equation. Thus, low strain-high electric field are the best conditions in order to maximize efficiency.

Moreover, in a recent work, H. Yang *et al.*[49] proposed a figure of merit for electrostatic systems that we used to compare different multistrip systems:

$$FoM = \frac{P}{V^2 \cdot A \cdot f} \qquad \text{(Eq. 4.5)}$$

here *P* is the generated power in μW, *V* is the bias voltage applied to the generator, *A* is the generator area and *f* is the working frequency. Fig. 4.36 shows the values of FoM obtained for the composites. As expected, the composite with load of 50 vol.% possesses the higher FoM value. Is also interesting to note the similar trends between efficiency and FoM in Fig. 4.36, that evidence the effect of CCTO inclusion on the electromechanical properties of electrostrictive polymers.

Table 4.7 *Efficiency table of TPU-CCTO composites (f=1 Hz; E=5MV/m; γ=12%)*

CCTO [vol. %]	Y [MPa]	P_{mech} [mW/cm^3]	P_{gen} [mW/cm^3]	Efficiency [‰]
0	20.19	145.4	0.005	0.031
10	25.6	184.3	0.014	0.075
20	32.6	234.7	0.018	0.076
30	36.2	260.6	0.076	0.291
40	35	252	0.07	0.277
50	39	280.8	0.176	0.627
60	47	338.4	0.084	0.249

To conclude, CCTO NPs have been prepared by a sol-gel synthesis, subsequent thermal treatment and final ball milling step. Their inclusion has been found to be an efficient way to increase the energy generation of electrostrictive TPU polymer matrixes (Estane^{TM} 58887), that showed to have a quadratic relation with harvested energy. Moreover, bias electric field and applied strain were found to have quadratic and linear relationships with generated energy, respectively. Sputtered gold electrodes were used to obtain compliant parallel plates on the films. Moreover, these electrodes are subjected by diffuse micro-cracking phenomenon when stretched, but this doesn't affect their conductivity properties, that are stable even after 100000 cycle of activation. Further studies must be focused on investigating the lifetime of sputtered gold electrodes in terms of cracking and conductivity, in order to verify their suitability to be employed in a real application.

Finally, I observed that 50 vol.% composite possess the best EH properties, due to maximization of CCTO/TPU (high-k/low-k) interfaces, that permit to it to reach energy generations up to 2.57 nJ cycle^{-1}, power peak of 9µW (E = 8.75·10^{6} V m^{-1}, γ = 12%, f = 1 Hz), efficiency up to 0.06% and a FoM of 10.7.

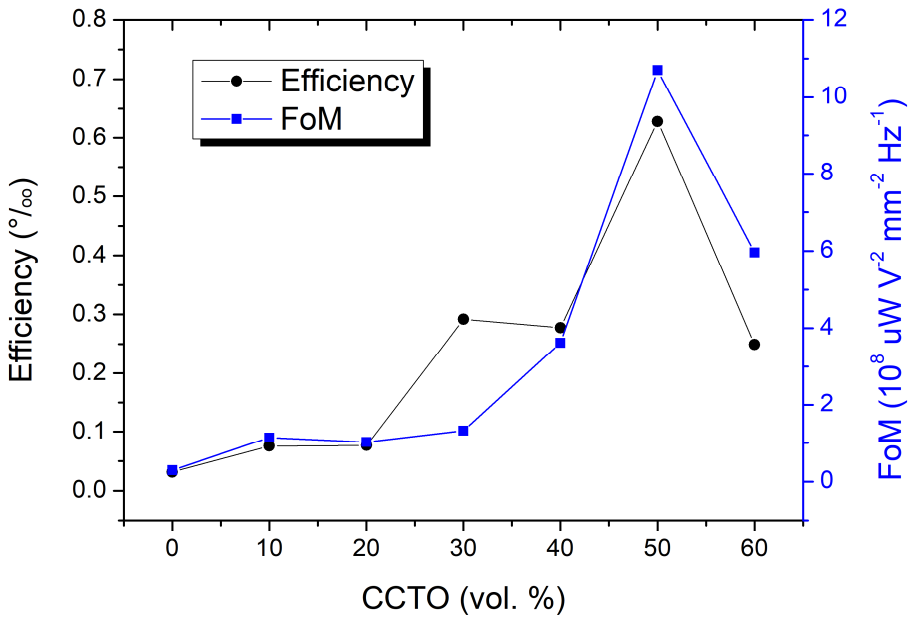

Fig. 4.36 *Efficiency and figure of merit trends as function of CCTO loading.*

4.2.2 Electrostrictive polymer stacking

In the previous section, we discussed the effect of CCTO NPs inclusion on EH properties of electrostrictive TPU matrixes. All the investigations were carried out on single films, in order to understand the effect of experimental conditions and materials properties on energy generation, giving less attention to absolute values of power and energy developed each cycle. As conclusion, the energy production is function of different experimental conditions, like *E*, γ, $d\gamma$ and *f*, but mostly on material dielectric properties like ε_r, that in turn affect ΔC between relaxed and stretched states. Since $C = \varepsilon_0 \cdot \varepsilon_r \cdot A/d$, dielectric constant maximization has a key role in capacitance maximization, leading to higher harvested energies.

Obviously, in the optic of *C* maximization, not only ε_r is available as a way to produce more energy, but also the area of the capacitor *A* and its thickness *d*, are parameters commonly used to increase *C*. For what concern *C* increasing by thickness decrease, it is a possible but tricky way to enhance *C*, because too thin films (below 30 µm) become susceptible to rupture under stretching. On the other hand, increase in capacitor area *A*, could lead to higher *C* without incur in additional problems. The only limitation of this approach is the available area that can be effectively exploited. Considering what said in the *state of the art* section (Chapter 2), heel region is the most suitable place were to perform EH. Considering an average foot sole area of 83 cm^2 [57], and taking into account that heel area is 1/3 of the total foot area, we obtain an available area of 27.6 cm^2, that is 4 times higher with respect to that investigated for our TPU-CCTO composites. Considering a linear relation of *A* with power *P* and harvested energy, we could obtain just 36µW and 1.03µJ $cycle^{-1}$ at

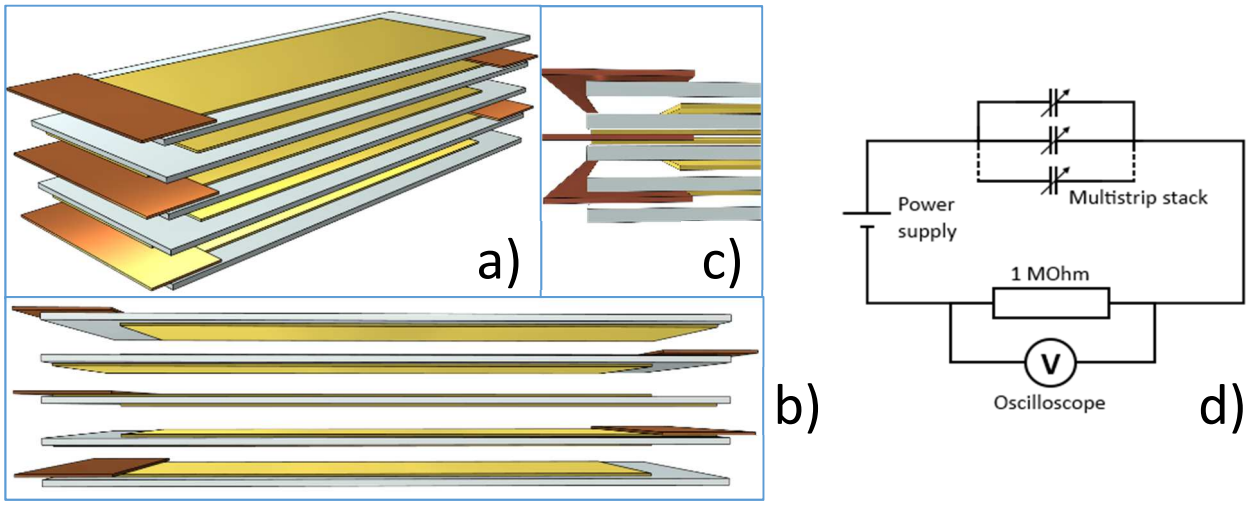

Fig. 4.37 *3D representation of strip stacking in the case of five single strips (mx5). a) perspective view; b) cutting view; c) compressed bridges in mx5, cutting view. The stack parts are thus represented: grey=polymer strip, yellow=gold electrode, brown=copper bridge. d) equivalent measuring circuit when using multristrip as generator.*

E=8.75 MV m^{-1}, exploiting all the available area, which is not yet sufficient to power micro-electronic nodes.

Taking into account a threshold value of about 100µW, in order to power a micro-electronic node, we have to increase the area (thus the generated power) of many times with respect to the single strip considered until now. Considering the simple calculation on heel area, it is obvious that even exploiting all the available space it is not enough to achieve the goal.

Here in this section, I present a novel stacking method to increase the active area of the electrostrictive generator by connecting in parallel different films strips (from 3 to 11) in order to maximize the energy generation, keeping the device hindrance practically unchanged. Fig. 4.37a-c shows the stacking arrangement used to connect in parallel pure Estane 58887 polymer strips, to obtain the final polymer stack (here called *multistrip*, or *mxN,* where N is the strips number in the stack). As it can be noted from the scheme, gold electrodes are not symmetrically deposited but are slightly offset by each other in order to avoid unwanted current flow between electrodes when connected to the circuit. Moreover, in the arrangement showed in Fig. 4.37a-c, the approaching electrodes of different films are in a *top/top – bottom/bottom* fashion, thus, facing electrodes are connected at the same pole of the power supply and there is not current flow. Copper protruding foils ensure the parallel connection between different strips: they act as bridges, connecting each other all the electrodes of the same pole. The main advantage of this stack arrangement, respect to that in the *top-bottom* fashion, is that it doesn't need any insulating additional layer between strips. Once the multistrip is simply assembled, it is mounted on the same measuring instrument described

Table 4.8 *Estane 58887 single strips electrical characterization. Cstress values were obtained from strips strained at 4%; ΔC=Cstress-Crelax.*

Sample	Thickness [µm]	C_{relax} [nF]	C_{stress} [nF]	ΔC [pF]	Resistance [GΩ]
1	45	0.87	0.901	31	1.2
2	55	0.68	0.695	15	1.87
3	43	0.883	0.91	27	1.1
4	38	1.14	1.18	40	1.1
5	54	0.77	0.782	12	1.9
6	62	0.72	0.744	24	2.9
7	40	1.1	1.14	40	0.9
8	35	1.27	1.315	45	0.6
9	34	1.29	1.33	40	0.5
10	32	1.26	1.3	40	0.6
11	28	1.51	1.58	70	0.4

before for single strips, for EH characterization. The equivalent circuit used to obtain power and energy values is that showed in Fig. 4.37d.

Before to proceed with the assembly and the electrical measurements of different multistrips, the single strips were characterized in terms of capacitance, in relaxed and stressed states, resistance and thickness. Table 4.8 summarized all the properties of the strips used in this work to build up the multistrips. Capacitance values were measured with a bridge capacitance meter working at 1.5 kHz. Resistance measurements were carried out by bringing the strip in the cell (mobile and fixed jaws), connecting it to the measuring circuit and submitting it to a bias voltage of 600V. The film resistance value was extrapolated from the voltage drop across the experimental resistor. The bias voltage was maintained constant for 3 minutes, until the voltage drop signal is stable during time. Subsequently, multistrips were assembled, accordingly with the arrangement described previously, and their electrical properties were measured, in the same conditions used for single strip characterization. Table 4.9 report the electrical measurement values obtained for multistrips from mx3 to mx11. As expected, both the values of C_{relax} and C_{stress} increase with the number of strips connected in parallel, compatibly to the sum of the capacitance of single strips involved in the stack. Another expected trend is that related to resistance: strips parallel connection involves also parallel connection of strip resistances. This leads to a decreasing of resultant resistance that follows the well know equation for parallel resistances:

$$\frac{1}{R} = \frac{1}{R_1} + \frac{1}{R_2} + \frac{1}{R_3} + \cdots + \frac{1}{R_n} \qquad \text{(Eq. 4.6)}$$

In turn, this is reflected on the leakage current (I_L) that passes through the strip when an electric field is applied (E). Fig. 4.38 reports the current vs time curves relative to the AC generation due to stress/relax cycles, for single strip and mx3. As expected, I_L increases with in the number of parallel strips, but the ratio between it and the generated current is still the same (7,4 and 7,5 for single

Table 4.9 *Multistrips electrical characterization. The measurement condition are the same as that used for single strips.*

Multistrip	C_{relax} [nF]	C_{stress} [nF]	ΔC exp. [nF]	ΔC calc. [nF]	Resistance [GΩ]	Average thickness [µm]
mx3	2.6	2.7	0.1	0.07	0.45	48
mx5	2.75	2.9	0.15	0.12	0.23	47
mx7	6.6	6.8	0.2	0.19	0.14	48
mx9	9	9.3	0.3	0.27	0.125	45
mx11	12.1	12.6	0.5	0.38	0.06	42

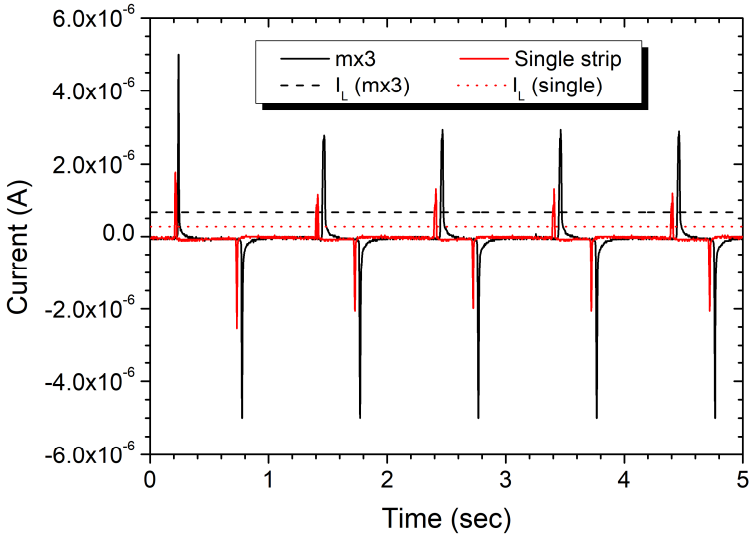

Fig. 4.38 *I vs t comparison graph between mx3 and single strip (Table 3.3, Sample 3), with leakage currents, at E=13MV/m, γ=4%; f=1Hz.*

strip and mx3, respectively). Moreover, is also evident that the generated current raises considerably from single strip to mx3, and this trend is confirmed also for all subsequent multistrips. This is a good achievement because one of the main problems related to EPs harvesting systems is the rectification of the generated AC current: higher output currents (thus voltages, at constant load) could permit the use of common full-wave bridge rectifiers to power small electronic devices. The effect of polymer stacking as function of *E* is reported in Fig. 4.39. Here, as in the case of single strips, a quadratic relationship between generated energy and *E* was found for all the multistrips prepared. However, what results out from the graph is the increase in energy generation with the

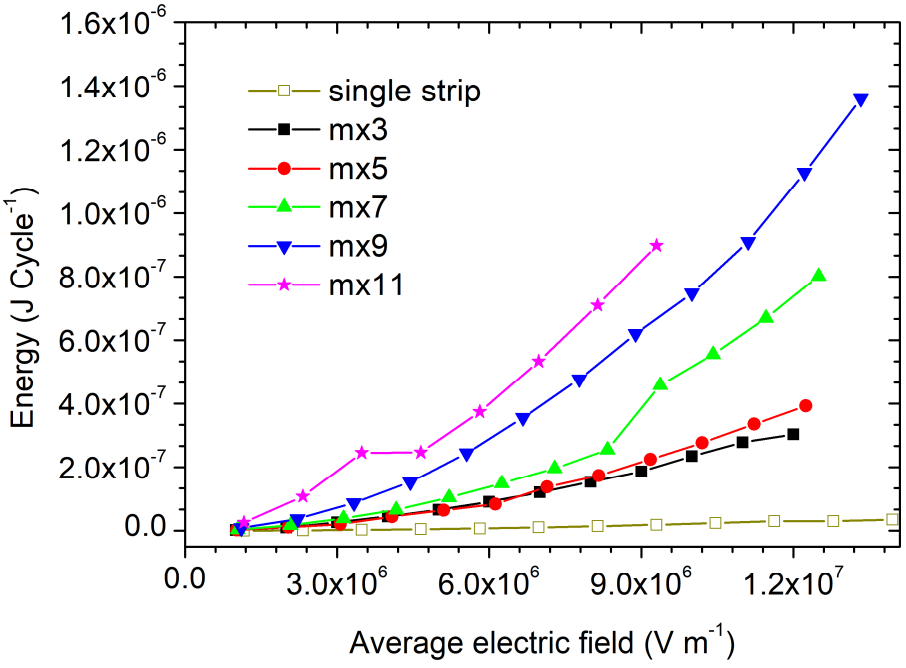

Fig. 4.39 *Multistrips energy generation as function of applied electric field at f=1Hz; strain=4%.*

increase of parallel strips. The energy increase is clearly visible yet with mx3: energy generation increases of one order of magnitude with respect to the single strip. This trend becomes dramatic when considering higher multistrips. For example, considering mx9 at 13 MV m^{-1} the energy generation increase reaches 3000% with respect to the single strip, reaching 1.4 µJ $cycle^{-1}$. Under these experimental conditions, mx9 reaches power generations up to 115 µW, enough to power small electronic devices like sensors and MEMS, wasting (due to leakage current) only 5 µW of that power.

Further investigations on multistrip systems have involved their mechanical behavior when working. Fig. 4.40 shows the tensile measurements carried out on a single film and on multiple systems. The specimens were stretched at γ=13.5% (ΔL=5mm) of their initial length with a ramp of 1 mm/sec, then were maintained at that length for 10 seconds and finally were relaxed until their original length. As expected, the force needed to stretch the different systems increases linearly with the number of strips measured at the same time. In fact, if 3N are needed to stretch one film of pure TPU, 15N are needed for 5 films and 30N are needed for 10, as clearly observable from the graphs. Data obtained from tensile measurements were used to extract stress-strain curves of the

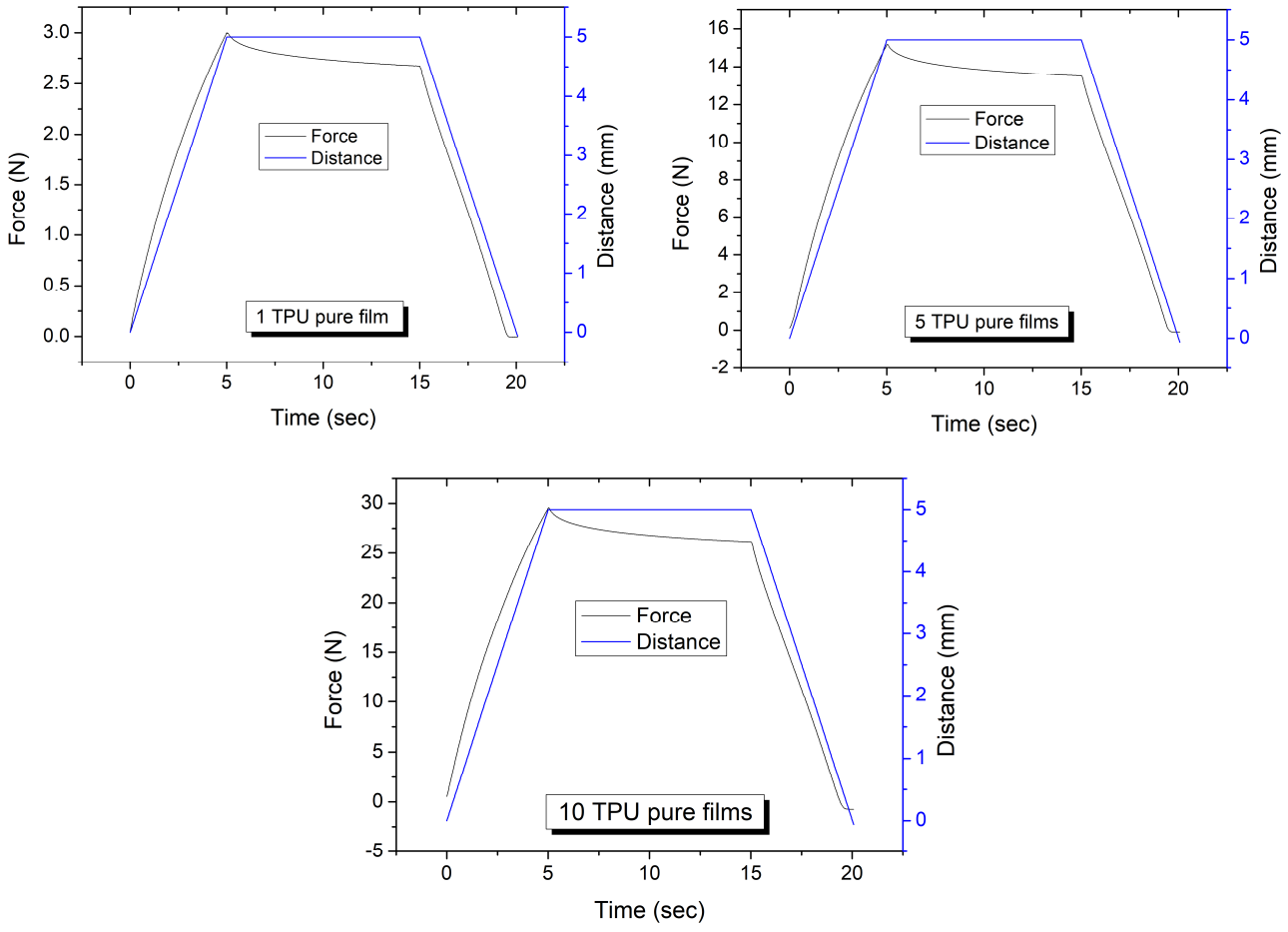

Fig. 4.40 *Tensile measurements carried out on pure 1, 5 and 10 TPU films. The films were stretched until γ=13.5% at 1mm/sec.*

Table 4.10 Figure of merits and efficiency values calculated for all the multistrip fabricated (f=1 Hz, γ=4%)

Multistrip	FoM [10^8 μW V^{-2} mm^{-2} Hz^{-1}]	P_{mech} [mW/cm^3]	P_{gen} [mW/cm^3]	η (%)
Single	1.74	16	0.14	0.9
mx3	7.08	48	0.25	0.54
mx5	2.35	80	0.16	0.2
mx7	4.43	112	0.33	0.29
mx9	5.4	144	0.43	0.3
mx11	6.09	176	0.44	0.25

measured systems, and to obtain the Young's modulus *Y* from the slope of that curve. From this calculation, we obtained a *Y* value of 20 for the TPU matrix (Estane 58887).

As expected, considering mx3 sample as an outlier, the FoM increases with number of strips connected in parallel. However, this is not true when considering the efficiency ($(P_{gen}/P_{mech}) * 100$). In fact, it undergoes a rapid decrease from single to multiple systems, and than reaches a maximum at mx9. This trend can be ascribed to different slopes of P_{mech} and P_{gen}. In fact, the slope of P_{mech} is higher than that of P_{gen} leading to decrease of efficiency by increasing the number of films connected. However, always facing to η maximization, efficiency trend can be reinterpreted by considering the context of energy harvesting from human gait. In fact, considering that the higher multistrip systems need 33N as maximum force to be stretched (at 13.5%, much higher than that investigated here), this means that at most a weight of 3.4Kg is needed to stretch completely these systems; much lower than that a common person, even the lightest ones, can impress on their foot soles.

In conclusion, even if *η* values decrease with *N*, this trend can be neglected, because of the huge excess amount of available mechanical energy with respect to that needed to activate the generator, making, to date, the absolute value of P_{gen} the real important value to be considered. In this frame, the parallel system can be a good way to increase the power generation to reach values high enough to be effectively employed to power small electronic nodes, as happened for our mx9 and mx11 multiple systems.

4.2.3 Pressure-to-tension mechanism (PT-bridge)

Until now, all the energy harvesting experiments were carried out on a test bench where single strips, or multiple systems, were clamped by two jaws and excited by an alternating movement of the mobile jaw. This, concurrently with an applied electric field, causes the energy generation. However, in order to transpose the concept in a real application, forces, available space and positions suitable to perform efficient EH from EPCs, must be individuated. Since EPCs films work under tension/relax cycles, the suitable foot region is the metatarsal one. Here, tension occurs when the foot pushes forward the body during the pass from single to double support in the stance phase. Unfortunately, despite tension occurs at the metatarsal region, the most present and intense form of excitation in feet during walking is the pressure exerted by the body weight on the ground. Moreover, intensity and presence of pressure on the sole area is almost independent from the type of shoe (*e.g.* trekking or elegant) and from its shape, while metatarsal tension can change as function of shoe stiffness. In this frame, in order to employ EPCs into shoe soles, a way to convert the pressure of body weight into tension to stretch the EPC film must be individuated. In our particular case, a vertical force (applied by body weight) has to be converted into a horizontal force, acting first in a sense and then, when the vertical force decreases (lifting of the foot), in the opposite sense to restore the initial state of the film and to proceed to another cycle.

To meet this need, we thought to a bridge-shaped elastic material able to perform the above-mentioned conversion (Fig. 4.41a-b). As it can be seen from the 3D scheme, a vertical force applied on the top of the arch corresponds to two horizontally directed forces, working on opposite verses, at its ends. Further, when the foot lift from the ground (thus in the absence of an applied force) the elastic nature of the bridge-shaped converter should restore its initial condition. To fabricate a so-called *PT-bridge* (from “pressure-to-tension” converter) the same TPU material (Estane 58887 – Lubrizol) used to fabricate our TPU-CCTO composites, was employed. In a typical laboratory fabrication procedure, in an Al_2O_3 rectangular mold, TPU pellets were placed in an amount enough to cover the bottom of the mold. The pellets were then put into an oven and melted at 190°C. The pellet melting permits to obtain a bulk rectangular sheet of TPU. Once the pellets are fused together, the mold is extracted from the oven then the TPU sheet, still hot, is removed, bended in the form of an arch and let cool until room temperature. The PT-bridges were fabricated to apply a γ=4 - 12% to a 5x2 cm film strip. Fig. 4.41c shows a PT-bridge obtained with this procedure.

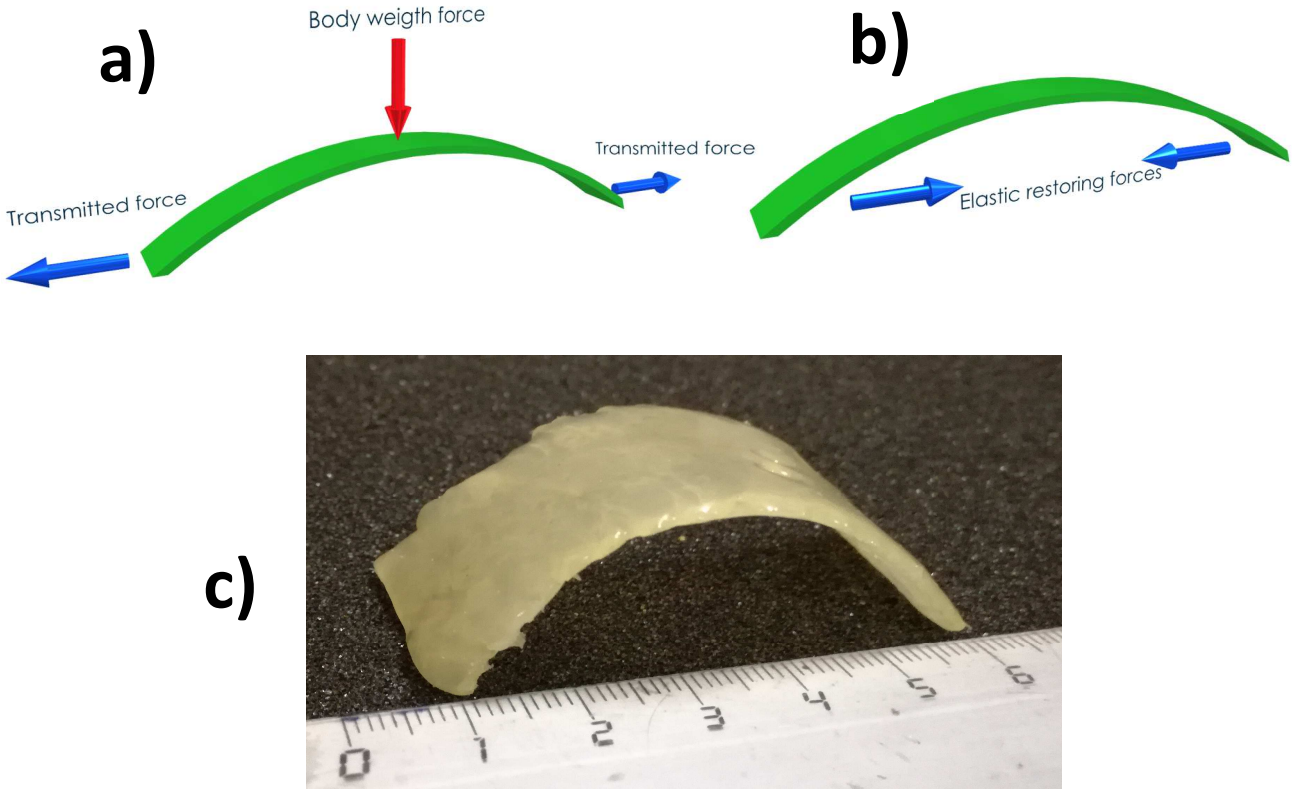

Fig. 4.41 *a) 3D-scheme of pressure to tension converting mechanism, under pressure, b) pressure to tension converting mechanism, without pressure, c) photograph of the fabricated converting mechanism.*

Considering clamping the electrostrictive film strip at the ends of this converting mechanism, the result of foot pressure and lift will be similar to that performed by the testing instrument (stress/relax cycles), so permitting the application of EPCs into a realistic context. To do this, the ends of the PT-bridge were bent to be flat and parallel (Fig. 4.42a). To afford a strong connection between the PT-bridge ends and the electrostrictive film, this last was directly melted onto the ends of the PT-bridge. In this way the movement of the PT-bridge ends will performs stress/relax cycles on the electrostrictive film. On the other hand, also the electrodes were modified to be applied into a real context. In fact, since the ends of the film are fused with the PT structure, the electric connection with capacitor plates (gold sputtered electrodes) is not available from the upper side anymore, thus it should be available from the side of the film. Copper sheets, employed in *multistrip* systems, even if permitting a rapid and sure electrical connection, result stiff and tend to break. To resolve this problem, an electrical conductive polymer composite was prepared. This was made by using the same TPU matrix (Estane 58887) loaded with 50% w/w with carbon black. Also this was obtained as film by solvent casting procedure, as described for TPU-CCTO samples. However, while CCTO loaded films still maintain their elastomeric properties, these conductive films, even still flexible, break down if subjected to high strains, but they are still able to tolerate the experimental

conditions of EPCs testing for many cycles. Further, two strips of this conductive composite were melted onto the opposite ends of the film, to connect only one side of the electrostrictive film each. The result is showed in Fig. 4.42a. As it can be seen, the protruding of the polymeric electrodes eases the electrical connection of the capacitor plates. Then, the devices obtained as showed in Fig. 4.42a-b were connected to the same testing electric circuit as that employed for single CCTO-loaded samples (Fig. 4.26). Once connected, the PT-bridge device was tested with the application of a force by the action of foot pressure directly on it. To protect the user from electrical contacts, the foot pressure was applied to the PT-bridge through a PTFE sheet. The result of foot pressure conversion in this arrangement are reported in Fig. 4.43. As it can be seen, the intensity of stress (down) and relax (up) signals are quite symmetric. Moreover, the intensity of the negative signal (stress state) is also function of the velocity with which the foot pressure is applied to the PT device (strain derivative). The dependence of the signal produced with the force applied (intensity and velocity) is also evident comparing power peaks. As it can be noted, the power peaks relative to relaxation (that depends by PT-bridge material elasticity) are reproducible both in intensity and width, while the signal relative to stress state (depending on foot pressure) are different from one excitation to the other. However, during testing of PT-bridge actuator we found a malfunction. In fact, after a few dozens of actuation cycles, the energy generation stopped suddenly and the voltage across the capacitor fell down to zero, like if there was an interruption in the electrical circuit. After an investigation about this, we found that an erosion of the lower gold electrode (in contact with the

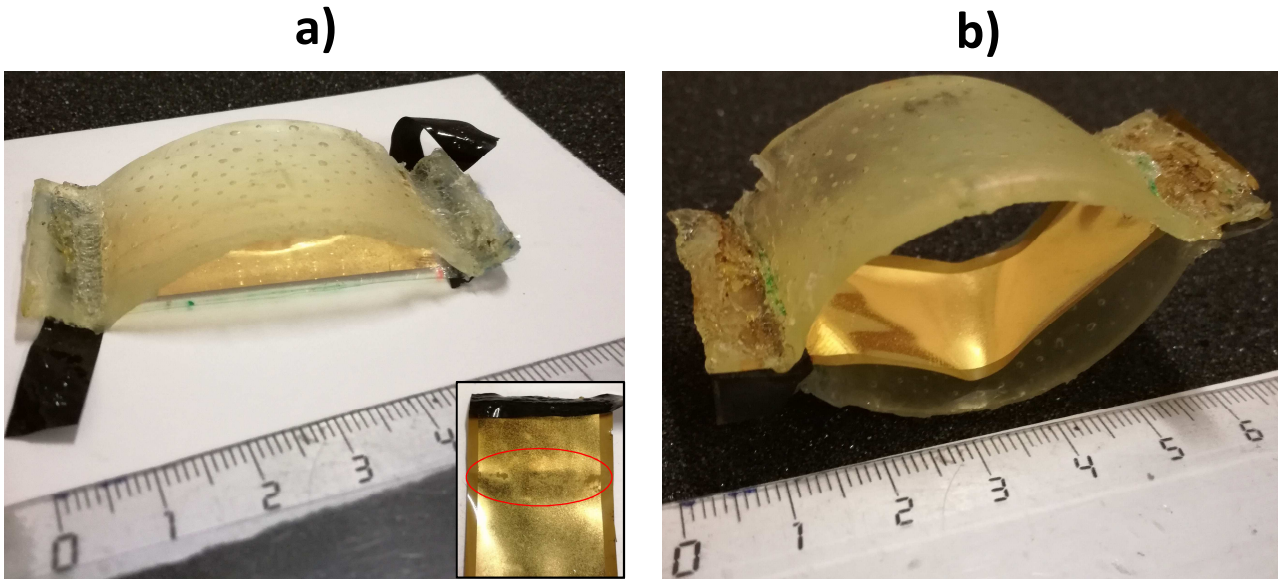

Fig. 4.42 *a) single PT-bridge structure with electrostrictive film (Estane 58887 pure) and conductive composites mounted on. Inset: gold electrodes erosion by friction with the ground; b) double PT-bridge structure with TPU-CCTO 50 vol.% film mounted on.*

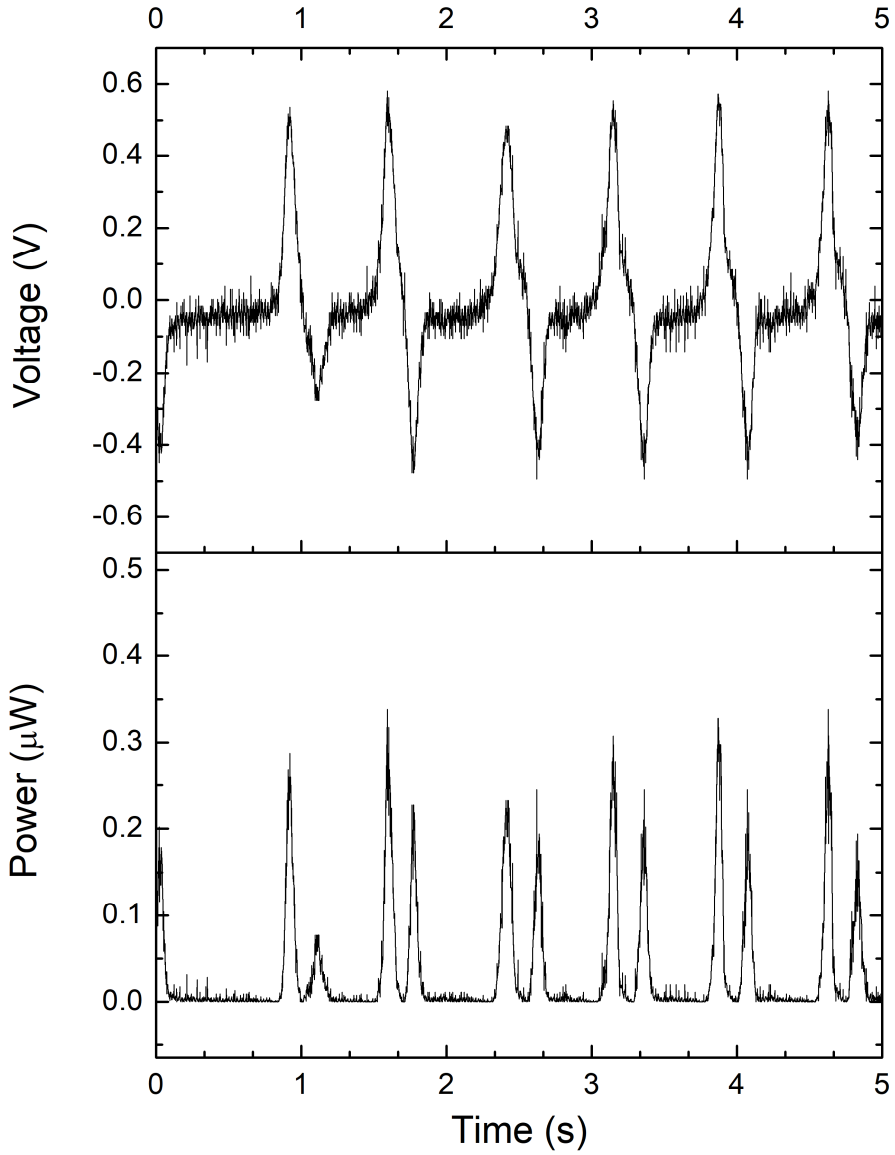

Fig. 4.43 *Voltage (up) and Power (bottom) graphs as function of time for foot-excited PT-bridge/TPU-CCTO 40 vol.%. E=1MV/m, γ=12%*

ground) occurred, thus interrupting the circuit (Fig. 4.42a - inset). This was due to the friction to which the film was subjected during cycles. In fact, the pressure of the foot on the PT-bridge squeezed it against the ground, thus consuming the gold electrodes by friction. To solve this problem, we simply added a second PT-bridge to the lower part, thus constituting a symmetrical device (Fig. 4.42b). In this way, friction between gold electrodes and the ground is avoided, permitting long-range use of the device, limited only by the performances of the materials involved in the energy generation process. The results obtained by (double) PT-bridge device were also compared with that obtained from measuring instrument, in order to highlight any differences deriving from the excitation type. What comes from this comparison is reported in Fig. 4.44a. As it can be noted, the intensities of voltage signals produced between PT-bridge and testing instrument are comparable. The main difference between them is the width of the signal produced. This can be

ascribed to different velocity of the displacement (application of strain to the film) between measuring instrument and PT-bridge, where this last resulted slower to perform stress/relax cycles. Fig. 4.44b shows the energy generation values of the PT-bridge device as function of the applied electric field with a film strip of TPU-CCTO 50 vol.%. Clearly, the quadratic trend is preserved, indicating that the PT-bridge device works well, performing perfectly repeatable harvesting cycles (no hysteresis or loss of elasticity was observed) and is completely comparable with the jaw couple system.

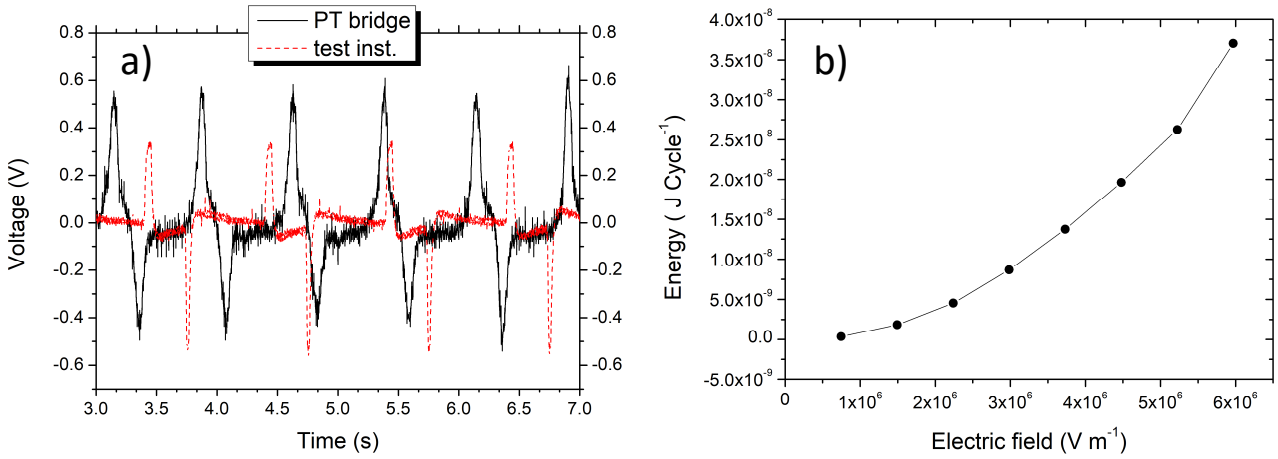

Fig. 4.44 *a) Voltage vs time scans of TPU-CCTO 40 vol.% obtained from activation by PT-bridge or measuring instrument (E=1MV/m; γ=12%; b) generated energy as function of the applied electric field for a TPU-CCTO 50 vol.% activated by double PT-bridge (f=1Hz, γ=4%)*

5. Conclusions

The target that I set at the beginning of this research project was to *study and develop an energy harvesting device, able to convert the mechanical energy of human gait into electrical energy.* The interest about energy harvesting devices comes from the fact that electrical energy is becoming one of the most (in if not THE most) form of energy consumed by people all over the world. In particular, they could find application in portable electronics. In this frame, human motion energy harvesting devices can give a substantial help.

In order to achieve such a complex goal, I proceeded through: (i.) critical study of the literature on this field, in order to identify the best physico-chemical processes to be employed; (ii.) laboratory experimentation of new efficient materials and processes basing on that individuated in (i.); (iii.) design and development of a prototype of energy harvesting device. Before to proceed with the study of the literature about human motion energy harvesting, an evaluation about the energy produced by humans during motion, was mandatory. A previous analysis on human gait returned the result that large amounts of energy are developed during motion in the form of pressure, in the heel region up to 1MPa, and tension, at the metatarsal region. These were considered as amounts able to feed small electronics devices.

For what concerns the panorama of suitable physico-chemical processes, five of them were individuated as possible candidates, belonging to three different classes: 1. Electromagnetic, 2. Piezoelectric, 3. Electrostatic. Among these, two were selected, both belonging to the electrostatic class: 1. Reverse electrowetting on dielectric (REWOD) and 2. Electrostriction by means of polymer composites (EPCs). The first comprises the changing of the active area of a variable capacitor by cyclical squeezing of a liquid conductive plate, while the second provides the change in capacitance by stretching of a polymer-based variable capacitor.

REWOD phenomenon was recently proposed (2011) by T. Krupenkin and J. A. Taylor in U.S., just for energy harvesting applications. It is the inverse of the more known electrowetting on dielectric. In REWOD, the liquid drop contact angle is changed by a mechanical stimulus that causes an alternative motion of charges stored in the capacitor, thus generating AC current. The system was composed by a quartz substrate coated with metallic Ta, as the electrode, that is further partially anodized to Ta_2O_5 and then spin-coated with a fluopolymeric layer (Cytop^{TM}). With this arrangement, they obtained energy densities up to about 400 nJ/mm^2 (oscillating plates at 70V bias voltage) and power densities up to 125 µW/mm^2, that reached up to 10 mW/mm^2 in the high

frequency "bubbler" device[31]. In this frame, during our research project I have investigated the use of ZrO_2 as high-k dielectric oxide layer, instead of Ta_2O_5, and polytetrafluoroethylene (PTFE) as the fluoropolymeric coating. Moreover, since REWOD device fabrication involved different steps, I also investigated the possibility to obtain a REWOD system composed of ZrO_2/PTFE bilayer by *one-pot* fabrication by sputtering deposition on p-doped Si(100) substrates. I obtained reproducible PTFE-coated ZrO_2 thin films layers fabricated only by sputtering deposition in a sequential deposition of the two materials. I found that the presence of PTFE sputtered layer considerably increased the energy generation of the REWOD device, passing from 0.2 to 1.3 μJ $cycle^{-1}$ (450% increase) but did not affect significantly the leakage current density, that was similar to that of ZrO_2 itself. Based on this REWOD energy values, I obtained energy density values up to 7.5 nJ $cycle^{-1}$ mm^{-2} at 30V of bias voltage. The comparison with Krupenkin's results evidenced that our energy density values were much lower than theirs, at the same bias voltage (110 nJ mm^{-2})[30]. This discrepancy could be ascribed to the interpretation of the measurement: in fact, the Hg drop when squeezed could not effectively cover all the area of the capacitor, giving an underestimated value. Further investigations about liquid drop behavior are needed to confirm this hypothesis. On the other hand, our energy density values are comparable to that obtained by Krupenkin *et al.* with the 22 Hg drops in a channel fashion[30], indicating that our systems, even still optimizable, can be a good alternative choice to that considered in the literature, with the advantage of a one-step fabrication process that could facilitate the industrial scale of this energy harvesting device.

The other process investigated to perform energy harvesting from human gait was that exploiting electrostrictive polymer composites (EPCs). Electrostriction is commonly defined as the quadratic coupling between the strain, which the material undergoes, and the applied electric field across it. EPCs were commonly studied as actuators, but recently P.-J. Cottinet *et al*. investigated their ability to perform mechanical-to-electrical energy harvesting in a pseudo-piezoelectric fashion that involve the cyclical stress/relax of the EPC film when subjected to a constant electric field[39]. They found that, beside experimental conditions like frequency, electric field intensity and amplitude of strain, also electric parameters like resistivity and dielectric constant (ε_r) affect the energy generation of these devices. In particular, ε_r seems to be one of the most important factors to be considered to obtain high energy harvesting values. During the research on EPCs, I investigated the energy harvesting properties of polyurethane (TPU) films filled with nanometric calcium copper titanate ($CaCu_3Ti_4O_{12}$, hereafter CCTO). CCTO is an inorganic compound that crystallizes in the body-centered cubic lattice (s.g.: Im3, No. 204) and is characterized by giant permittivity values (up to

10^5). It was prepared by sol-gel method in from of nanoparticles (CCTO NPs), that were then incorporated (at various vol.%) in the TPU matrix. The films obtained were cut into 2x5 cm rectangular strips, provided with gold electrode on both faces (A=6 cm^2) and tested under different experimental conditions. I observed that the inclusion of CCTO NPs into the TPU matrix increased quadratically the energy generation, passing from 9 to 40 nJ $cycle^{-1}$ at 4 MV m^{-1}, for the pure TPU and 50 vol.% loaded EPC, respectively, corresponding to more than 400% increase. The values obtained for 50 vol.% loaded samples, gave energy densities up to 42 nJ $cycle^{-1}$ cm^{-2} and power densities of almost 1.5 μW $cycle^{-1}$ cm^{-2}, at 8 MV m^{-1} of bias electric field.

I also studied the possibility to connect in parallel different EP strips and to subject this *multistrip* to stress/relax cycles. To do this, I used from 3 to 11 pure TPU strips connected in parallel. I found that parallel connection of strips permits to increase considerably the energy generation, but also increases losses by leakage current, due to parallel connection of resistances related to each strip; thus a trade-off had to be individuated in order to maximize energy generation with low values of leakage current. In this case, it corresponds to nine strips in parallel, that produced up to 11 nJ $cycle^{-1}$ cm^{-2} and 1 μW $cycle^{-1}$ cm^{-2} at 8 MV m^{-1}, wasting only 28 nW cm^{-2} due to leakage current. Even if by comparison with 50 vol.% CCTO loaded strips, the multistrip device seems to be less performing, it should be taken into account that experimental conditions were different for the two devices. In fact, multistrip device testing was carried out at γ=4% and using pure TPU strips, that were found to be less performing than the loaded ones. However, with this arrangement the harvested energy reached 477 nJ $cycle^{-1}$, with power 54 μW $cycle^{-1}$ (γ=4%, E=8 MV m^{-1}), against 257 nJ $cycle^{-1}$ and 9 μW $cycle^{-1}$ of the 50 vol% CCTO-loaded sample (γ=12%, E=8 MV m^{-1}). This means that also if the multistrip system is less “efficient” than the single strip, it is more powerful and could permit to power small electronics nodes.

A last consideration regards the comparison between different approaches used to perform human gait energy harvesting. Table 5.1 listed power, energy and density values for the different systems investigated. As it can be noted, the ZrO_2/PTFE REWOD device is much more efficient than EPCs-based one. However, it should reminded that the energy generated by the two different harvesters is function of the applied electric field. Thus, scaling EPC energy generation to *E* working values typical of REWOD devices will give, theoretically, energy densities of about 100 nJ mm^{-2}, that are comparable with those obtained by Krupenkin *et al.* in their pioneering work on reverse electrowetting on Ta_2O_5/Cytop™ bilayers[30].

In conclusion, during this doctoral research project I have successfully designed, fabricated and tested energy harvesting devices based on innovative reverse electrowetting on dielectric (REWOD) and electrostrictive polymer composites materials, respectively based on ZrO_2/PTFE bilayers and TPU-$CaCu_3Ti_4O_{12}$ composites. I also found that REWOD devices works better with respect to EPCs for energy harvesting purposes, reaching values of 0.4 mW cm^{-2} and 0.7 μJ cm^{-2}. Further optimization of ZrO_2/PTFE bilayers could lead to higher energy and power generations, while the reduction of thickness of EPC-based energy harvesting devices could provide such high applied electric fields to reach harvesting performances comparable to that of REWOD devices.

Table 5.1 *Power, energy and density values obtained for REWOD and EPCs-based energy harvesting devices developed in this research project*

	ZrO_2/PTFE	**TPU-CCTO 50 vol.%**	**mx9 (Pure TPU)**
Power peak [μW]	197	9	54
Power density [μW cm^{-2}]	444	1.5	1
Energy [μJ]	1.2	0.26	0.47
Energy density [nJ cm^{-2}]	735	43	11
Electric field [V m^{-1}]	$1.2 \cdot 10^8$	$8 \cdot 10^6$	

6. Bibliography

[1] S. Chu and A. Majumdar, *Nature*, 2012, **488**, 7411

[2] S. P. Beeby, M. J. Tudor and N. M. White, *Meas. Sci. Technol*., 2006, **17**, R175

[3] P. D. Mitcheson, E. M. Yeatman, G. K. Rao, A. S. Holmes and T. C. Green, *Proc. IEEE,* 2008, **96**, 1457

[4] J. M. Donelan, Q. Li, V. Naing, J. A. Hoffer, D. J. Weber and A. D. Kuo, *Science*, 2008, **319**, 5864

[5] Z. L. Wang, *Adv. Mater*., 2012, **24**, 1759

[6] S. Bauer, S. Bauer-Gogonea, I. Graz, M. Kaltenbrunner, C. Keplinger and R. Schwodiauer, *Adv. Mater.*, 2014, **26**, 149

[7] T. Starner, *IBM Syst. J*., 1996, **35**, 618

[8] P. Niu, P. Chapman, R. Reimer and X. Zhang, *Power Electronics Specialists Conference*, 2004, **3**, 2100

[9] M. Gorlatova, J. Sarik, G. Grebla, M. Cong, I. Kymissis and G. Zussman, *IEEE Journal on Selected Areas in Communications*, 2015, **33**, 1624

[10] E.M. Hennig and T.L. Milani, 1995, Journal of Applied Biomechanics 11: 303

[11] C. R. Bowen, H. A. Kim, P. M. Weaver and S. Dunn, *Energ. Environ. Sci.*, 2014, **7**, 25

[12] R. Hinchet, W. Seung and S.-W. Kim, *ChemSusChem*, 2015, **8**, 2327

[13] S. Chikazumi and S. H. Charap, *Physics of Magnetism*, Krieger, 1978

[14] R. E. Newnham, *Properties of Materials, Oxford University Press*, 2005

[15] E. W. Becker, W. Ehrfeld, P. Hagmann, A. Maner and D. Munchmeyer, *Microelectron. Eng*., 1986, **4**, 35.

[16] K. Kratt, M. Seidel, M. Emmenegger, U. Wallrabe and J. G. Korvink*, Proc. IEEE Micr. Elect.*, 2008, 996

[17] C. B. Williams, C. Shearwood, M. A. Harradine, P. H. Mellor, T. S. Birch and R. B. Yates, *IEE Proc.-Circuits Devices Syst.*, 2001, **148**, 337

[18] S. P. Beeby, R. N. Torah, M. J. Tudor, P. Glynne-Jones, T. O'Donnell, C. R. Saha and S. Roy*, J. Micromech. Microeng.*, 2007, **17**, 1257

[19] S. O. Kasap, *Principles of Electronic Materials and Devices*, 2006, McGraw-Hill

[20] A. Khaligh, P. Zeng and C. Zheng, *IEEE Trans. Ind. Electron*., 2010, **57**, 850

[21] S. Priya and D. J. Inman, *Energy Harvesting Technologies*, Springer, 2009

[22] J. Kymissis, C. Kendall, J. Paradiso and N. Gershenfeld, *Proc. 2nd IEEE Int. Conf. Wearable Computers*, 1998, **132**

[23] Zhao and Z. You, *Sensors*, 2014, **14**, 12497–12510

[24] K. Ishida, T.-C. Huang, K. Honda, Y. Shinozuka, H. Fuketa, T. Yokota, U. Zschieschang, H. Klauk, G. Tortissier, T. Sekitani, H. Toshiyoshi, M. Takamiya, T. Someya, T. Sakurai, (2013) *IEEE Journal of Solid-State Circuits*, 2013, **48**, 255

[25] A. F. Diaz and R. M. Felix-Navarro, *J. Electrostat.*, 2004, **62**, 277

[26] F.-R. Fan, Z.-Q. Tian and Z. L. Wang, *Nano Energy*, 2012, **1**, 328

[27] Z. L. Wang, J. Chen and L. Lin, *Energy Environ. Sci*., 2015, **8**, 2250

[27a] L. Beccai *et al.*, *Adv. Energy Mater.*, 2014, **4**, 12, 1400024

[28] J. Wang, S. Li, F. Yi, Y. Zi, J. Lin, X. Wang, Y. Xu and Z. L. Wang, Nat. Commun., 2016, **7**, 12744

[29] W.-S. Jung, M.-G. Kang, H. G. Moon, S.-H. Baek, S.-J. Yoon, Z. L. Wang, S.-W. Kim and C.-Y. Kang, *Sic. Rep. - UK,* 2015, **5**, 9309

[30] T. Krupenkin and J. A. Taylor, *Nat. Commun*., 2011, **2**, 448

[31] T.-H. Hsu *et al.*, *Sci. Rep.,* **5**, 16537

[32] F.M. Guillot, E. Balizer, *Journal of Applied Polymer Science*, 2003, **89**, 399

[33] J. Su, Q. M. Zhang, R. Y. Ting, *Appl. Phys. Lett*., 1997, **71**, 386

[34] R. Pelrine, R.D. Kornbluh, J. Eckerle, P. Jeuck, S. Oh, Q. Pei and S. Stanford, *Proc. SPIE, Int. Soc. Opt. Eng.*, 2001, **4329**

[35] Q.M. Zhang, H. Li, M. Poh, F. Xia, Z.-Y. Cheng, H. Xu, C. Huang, *Nature*, 2002 **419**, 284

[36] D. Guyomar, L. Lebrun, C. Putson, P.-J. Cottinet, B. Guiffard and S. Muensit, *Journal of applied physics,* 2009, **106**, 014910

[37] Y. Bar-Cohen, *J. Adv. Mater.*, 2006, **38**, 4

[38] Y. Liu, K. L. Ren, H. F. Hofmann and Q. Zhang, *IEEE transactions on ultrasonics, ferroelectrics, and frequency control*, 2005, **52**, 12

[39] P.-J. Cottinet, D. Guyomar, B. Guiffard, C. Putson and L. Lebrun, *IEEE Transactions on Ultrasonics, ferroelectrics and frequency control*, 2010, **57**, 4

[40] P.-J. Cottinet *et al., IEEE T. Ultrason. Ferr.,* 2010, **57**, 4, 774

[41] J. Liu, R. W. Smith and W.-N. Mei, *Chem. Mater.*, 2007, **19**, 6020–6024

[42] Y. Liu, K. Ren, H. F. Hofmann and Q. M. Zhang, *Proc. SPIE, Int. Soc. Opt. Eng.*, 2004, **5385**, 1, 17

[43] J. Robertson, *Eur. Phys. J. Appl. Phys*.,2004, **28**, 265

[44] Y. Zhang, G. H. Yang, E. T. Kang, K. G. Neoh, W. Huang, A. C. H. Huan, S. Y. Wu, *Langmuir*, 2002, **18**, 6373

[45] M. Drabik, O. Polonskyi, O. Kylian, J. Cechvala, A. Artemenko, I. Gordeev, A. Choukourov, D. Slavınska, I. Matolinova, H. Biederman, *Plasma Process. Polym.*, 2010, **7**, 544

[46] D.S. Bodas et al., *Appl. Surf. Sci.*, 2005, **245**, 202

[47] S. Roberts, J. Ryan, L. Nesbit, *J. Electrochem. Soc.,* 1986, **133**, 7

[48] Y. N. Wu *et al.*, *Phys. Rev.*, 2011, **B 83**, 144105

[49] H. Yang *et al.*, *Nano Energy*, 2017, **31**, 450

[50] M. Ahmadipour, M.F. Ain, Z.A. Ahmad, *Nano-Micro Letters* **2016**, *8*, 291

[51] M. Arbatti, X. Shan, Z. Cheng, *Adv. Mater.*, 2007, **19**, 1369

[52] V. Di Noto, G. A. Giffin, K. Vezzù, M. Piga, S. Lavina, *Solid State Proton Conductors: Properties and Applications in Fuel Cells*, P. Knauth, M. L. Di Vona, Eds., *John Wiley & Sons* (**2012**), Weinheim, Germany, pp. 107-180

[53] V. Di Noto, M. Vittadello, K. Yoshida, S. Lavina, E. Negro, T. Furukawa, *Electrochim. Acta*, 2011, **57**, 192

[54] F. Bertasi, E. Negro, K. Vezzù, G. Nawn, G. Pagot, V. Di Noto, *Electrochim. Acta*, 2015, **175**, 113

[55] N.H. Bingham, B. Dunham, *Annals of the Institute of Statistical Mathematics,* 1997, **49**, 667

[56] X. Yin, M. Lallart, P.-J. Cottinet, D. Guyomar, J.-F. Capsal, *Appl. Phys. Lett.*, 2016, **108**

[57] X. Lalande, B. Vie, J. P. Weber, Y. Jammes, *J. Am. Podiat. Med. Assn.,* 2016, 106, **4**, 265

7. Acknowledgments

At first, I want to thank my **family** and my **parents** for the support they give me during all these three years, without which would have been impossible to reach this goal.

Many thanks to Professor **Piercarlo Mustarelli**, that wisely driven me across these years of research listening, discussing and advising me for all of my doubt, scientific and not. Thank you *Lalo*.

I want to thank also **ATOM S.p.A.** for financing of this project that I had the pleasure to work for (in the memory of the co-founder Luciano Deambrosis), and in particular I want to thank Ing. *Sergio Dulio* that always supported us during all the scientific research, with useful suggestions and consulting on fabrication and future trends in the shoe industry.

I want to thank all the collaborators that actively worked with me on different aspects of my research project: **Pietro Zandalazini**, for the HUGE support on design and fabrication of the measuring instrument; *Giorgio Bacchio* and *Riccardo Castelli*, for fundamental support on the practical assembly and manufacturing of measuring instrument parts; *Corina Savazzi*, for useful advises on electrical measurements and electronic components. I want to thank also *Alessandro Invernizzi*, *Chiara Ferrara*, *Valentina Dall'Asta*, *Irene Quinzeni*, *Leonardo Lanfredi* and *Sara Bonomi*.